



저작자표시-비영리-변경금지 2.0 대한민국

이용자는 아래의 조건을 따르는 경우에 한하여 자유롭게

- 이 저작물을 복제, 배포, 전송, 전시, 공연 및 방송할 수 있습니다.

다음과 같은 조건을 따라야 합니다:



저작자표시. 귀하는 원저작자를 표시하여야 합니다.



비영리. 귀하는 이 저작물을 영리 목적으로 이용할 수 없습니다.



변경금지. 귀하는 이 저작물을 개작, 변형 또는 가공할 수 없습니다.

- 귀하는, 이 저작물의 재이용이나 배포의 경우, 이 저작물에 적용된 이용허락조건을 명확하게 나타내어야 합니다.
- 저작권자로부터 별도의 허가를 받으면 이러한 조건들은 적용되지 않습니다.

저작권법에 따른 이용자의 권리는 위의 내용에 의하여 영향을 받지 않습니다.

이것은 [이용허락규약\(Legal Code\)](#)을 이해하기 쉽게 요약한 것입니다.

[Disclaimer](#)

공학박사 학위논문

**Development of Twin Roll Cast
Magnesium Alloys with High
Formability and High Strength**

고성형성 고강도 TRC 마그네슘합금 개발

2016년 08월

서울대학교 대학원

재료공학부

박 상 준

Development of Twin Roll Cast Magnesium Alloys with High Formability and High Strength

지도교수 신 광 선

이 논문을 공학박사 학위논문으로 제출함

2016년 07월

서울대학교 대학원

재료공학부

박 상 준

박상준의 박사 학위논문을 인준함

2016년 07월

위 원 장 한 홍 남 (인)

부위원장 신 광 선 (인)

위 원 김 낙 준 (인)

위 원 김 도 향 (인)

위 원 이 경 훈 (인)

Abstract

Development of Twin Roll Cast Magnesium Alloys with High Formability and High Strength

Sang Jun Park

School of Materials Science and Engineering

The Graduate School

Seoul National University

World demand for magnesium alloys has rapidly grown due to interests in vehicle weight reduction and fuel efficiency. Magnesium alloy components have been mainly manufactured by the high-pressure die casting (HPDC) process because of high efficiency and low production cost. However, magnesium components manufactured by the HPDC process suffer from porosity and have the limitations in mechanical properties such as tensile strength and elongation. The demand for magnesium components with high plasticity wrought magnesium alloys has dramatically increased during the past decade in the automobile industry. Wrought magnesium components are mainly produced by the extrusion or rolling process which are more expensive than casting processes in production cost. Therefore, new process for wrought magnesium components should be necessary to produce Mg alloy sheets with low production cost and high production speed. Recently, twin roll casting (TRC) process which is a combination of rolling and casting

process has been paid attention to produce low cost TRC Mg-Al-Zn alloy sheets. However, those alloys are not suitable for TRC process due to the appearance of centerline segregation and cracks, which could significantly alter their mechanical properties. It is mandatory to consider the mechanical properties and controlled segregation of Mg alloys developed by TRC process, because it mainly affects the surface quality and mechanical properties of the products.

The first objective of this study is to understand the solidification and deformation behavior in TRC Mg-6Al-X alloys to develop the new TRC Mg alloys. Simulations of TRC process were carried out in order to develop suitable TRC Mg alloy by considering both thermal and thermodynamic properties. The TRC simulation results showed that AX60 alloy had the lower segregation tendency, while AZ60 had the highest segregation tendency because of its different solidification behavior and thermal properties. Compared to the as-cast microstructure, segregation area in as-cast was well matched with the melt to roll nip distance predicted in simulation. Annealed Mg alloys with addition of Ca or Sr elements showed weaker texture when compared to A6 alloy rolled at 350°C. In addition, there was a significant change in (0002) pole figures from strong basal textures to random texture when rolling temperature increased from 350°C to 450°C. It may be attributed to the activity of non-basal slip system at high rolling temperature. Results of visco-plastic self-consistent (VPSC) simulation revealed that critical resolved shear stress (CRSS) of tension twin increased with increasing rolling temperature resulting in suppression of the activity of tension twin in compression, which was associated with enhancing the yield isotropy and formability of Mg-6Al-X alloys.

Furthermore, the relative activities of basal $\langle a \rangle$ slip in AX60 alloy were higher than the other Mg alloys resulting from weaker basal textures, which were responsible for enhancing the formability and yield isotropy of Mg alloys.

The second objective of this study is to understand the effects of alloying elements such as Al, Mn, Ca, Sn, Sr, and Zn on yield isotropy and deformation behavior of Mg- x Al and Mg-6Al-X alloys. Furthermore, mechanical properties, microstructure and texture evolutions of Mg- x Al and Mg-6Al-X alloys have also been investigated. All alloys showed the improved yield isotropy with increasing alloying elements. Especially, addition of Ca element played a role in significant increase of yield isotropy compared to other elements, and Mg-6Al-1Ca alloy exhibited the enhanced yield isotropy with over the 0.80. From the VPSC results, Mg alloys with weaker basal textures had more relative activity of basal $\langle a \rangle$ slip at both tension and compression deformation, and that was considered to be responsible for CRSS value. In addition, it showed that there is a close relationship between yield isotropy and the relative activity of tension twin in compression deformation. Higher value of yield isotropy could be obtained by restricting the initiation of tension deformation.

The third objective of this study is to develop high strength and high formability TRC Mg alloys with low pre-heating temperature. Formability and VPSC simulations of Mg-4Zn-X-Ca alloys have been carried out to understand the relationship between deformation behaviors and room temperature formability. Microstructure, texture and mechanical properties of Mg-4Zn-X-Ca alloys have also been investigated. All the alloys showed sound TRC microstructure without occurrence of the inverse segregation. Annealed Z4 and ZSX400 alloys exhibited strong basal textures, however, the rest of Mg alloys showed weaker basal textures with a splitting to

transverse direction resulting from their different types of static recrystallization. The formability and yield strength of ZX40 alloys significantly increased by Ca addition compared to Z4 alloy. Especially, Erichsen value of ZX40 alloy was 7.2mm, however, that of Z4 alloy was 3.8mm due to low yield isotropy (compressive yield strength/tensile yield strength) in Z4 alloy. Among the Mg-4Zn-X-Ca alloys, ZAX400 alloy exhibited high yield strength of 189.3MPa and excellent formability of 7.5mm which was comparable with those of Al alloys. Higher values of formability for Mg-4Zn-X-Ca alloys were closely related to modified deformation behaviors resulting from texture evolutions. Higher formable Mg alloys, ZX40, ZAX400, ZCX400, and ZWX400 alloys, had the higher relative activity of basal $\langle a \rangle$ slip at compression deformation resulting in improved yield isotropy. However, normal formable Mg alloys, Z4 and ZSX400 alloys, had the relatively lower activity of basal $\langle a \rangle$ slip at compression modes caused by their different CRSS ratio (tension twin/basal $\langle a \rangle$).

Keywords: Mg Alloys, Twin Roll Casting, Segregation, Mechanical Properties, Formability, Texture, VPSC

Student Number: 2010-30176

Contents

Chapter 1 Introduction.....	1
1.1 Motivation	1
1.2 Twin roll casting process	7
1.3 High formable wrought Mg alloys	12
1.4 Plastic deformation in Mg alloys.....	14
1.4.1 Slip deformation.....	14
1.4.2 Twinning system	20
Bibliography	25
 Chapter 2 Analysis of the solidification and deformation behavior of TRC Mg-6Al-X alloys.....	 28
2.1 Introduction	28
2.2 Experimental procedures	31
2.3 Results and discussions	34
2.3.1 TRC simulation and thermodynamic calculations	34
2.3.2 Microstructural evolution.....	38
2.3.3 Texture evolution	43
2.3.4 Mechanical properties and formability	46
2.3.5 VPSC simulations	51
2.3.6 Finite element simulation during Erichsen test.....	59
2.4 Conclusions	64
Bibliography	65

Chapter 3	Effects of alloying elements on deformation behaviors of Mg alloys.....	69
3.1	Introduction	69
3.2	Experimental procedures.....	72
3.3	Results and discussions	74
3.3.1	Effects of Al	74
3.3.2	Effects of Mn	80
3.3.3	Effects of Ca	86
3.3.4	Effects of Sn.....	92
3.3.5	Effects of Sr	99
3.3.6	Effects of Zn	105
3.3.7	Effects of alloying elements on grain size, texture and yield isotropy	111
3.4	Conclusions	115
	Bibliography	116
Chapter 4	Characterization of TRC Mg-Zn-X-Ca alloys for enhanced room temperature formability	121
4.1	Introduction	121
4.2	Experimental procedures.....	124
4.3	Results and discussions	127
4.3.1	Microstructure of Mg-4Zn-X-Ca alloys	127
4.3.2	Texture of Mg-4Zn-X-Ca alloys	132
4.3.3	Mechanical properties and formability of Mg-4Zn-X-Ca	

alloys	136
4.3.4 VPSC simulations of Mg-4Zn-X-Ca alloys	142
4.3.5 Relationship between formability vs. yield isotropy vs. deformation behavior	147
4.3.6 Finite element simulation during Erichsen test	151
4.4 Conclusions	154
Bibliography	156

List of Tables

Table 1.1	Physical properties of magnesium and other metals.	4
Table 1.2	Mechanical properties of commercial wrought magnesium alloys.....	6
Table 1.3	Research and development activities of TRC Mg. .	11
Table 1.4	Vector energies for the possible dislocation types in Mg metals.....	17
Table 1.5	Twin type and corresponding misorientation angle in Mg crystal.	24
Table 2.1	Chemical composition of TRC Mg-6Al-X alloys...	33
Table 2.2	Mechanical properties and formability of annealed Mg-6Al-X alloys.	49
Table 3.1	Mechanical properties and formability of Mg-xAl alloys.	79
Table 3.2	Mechanical properties and formability of Mg-6Al-xMn alloys.	85
Table 3.3	Mechanical properties and formability of Mg-6Al-xCa alloys	91
Table 3.4	Mechanical properties and formability of Mg-6Al-xSn alloys	98
Table 3.5	Mechanical properties and formability of Mg-6Al-	

	<i>x</i> Sr alloys.....	104
Table 3.6	Mechanical properties and formability of Mg-6Al- <i>x</i> Zn alloys.....	110
Table 4.1	Chemical compositions of the investigated alloys.	126
Table 4.2	Mechanical properties and formability of Mg-4Zn- X-Ca alloys.	139

List of Figures

Figure 1.1	World magnesium consumption.....	5
Figure 1.2	Conventional process vs. twin roll casting process in POSCO.....	9
Figure 1.3	Schematic diagrams of Bessamer's twin roll caster	10
Figure 1.4	Burgers vector in the hexagonal close-packed lattice	18
Figure 1.5	Theoretically possible slip modes in magnesium, colored surfaces represent each slip planes, arrows represent slip direction Burgers vectors. (a) $\langle a \rangle$ type slip systems, (b) $\langle c+a \rangle$ type slip systems.....	19
Figure 1.6	Variation of twinning shear with the axial ratio for the hexagonal metals. A filled symbol indicates that the twin mode is an active mode.....	22
Figure 1.7	Relationship between planes K_1 , K_2 , and directions η_1 , η_2	23
Figure 2.1	Distribution of liquid fraction on Mg-6Al-X alloys; (a) A6, (b) AX60, (c) AJ60 and (d) AZ60.....	37
Figure 2.2	Solidification behavior of Mg-6Al-X alloys; (a) A6, (b) AX60, (c) AJ60 and (d) AZ60.	37
Figure 2.3	Microstructures of as-cast Mg-6Al-X alloys; (a) A6,	

	(b) AX60, (c) AJ60 and (d) AZ60	40
Figure 2.4	Relationship between centerline segregation area and melt to roll nip distance of Mg-6Al-X alloys...	41
Figure 2.5	Microstructures of annealed Mg-6Al-X alloys rolled at 350°C; (a) A6, (b) AX60, (c) AJ60 and (d) AZ60	42
Figure 2.6	Microstructures of annealed Mg-6Al-X alloys rolled at 450°C; (a) A6, (b) AX60, (c) AJ60 and (d) AZ60.	42
Figure 2.7	(0002) pole figures of annealed Mg-6Al-X alloys rolled at 350°C; (a) A6, (b) AX60, (c) AJ60 and (d) AZ60	45
Figure 2.8	(0002) pole figures of annealed Mg-6Al-X alloys rolled at 450°C; (a) A6, (b) AX60, (c) AJ60 and (d) AZ60	45
Figure 2.9	Nominal strain-stress curves of annealed Mg-6Al-X alloys rolled at 350°C	48
Figure 2.10	Nominal strain-stress curves of annealed Mg-6Al-X alloys rolled at 450°C	50
Figure 2.11	VPSC simulation results of annealed Mg-6Al-X alloys rolled at 350°C; (a) experimental and simulated stress-strain curves, (b) hardening curves	

	of deformation modes, (c) relative activities during tensile deformation and (d) relative activities during compressive deformation.....	54
Figure 2.12	VPSC simulation results of annealed Mg-6Al-X alloys rolled at 450°C; (a) experimental and simulated stress-strain curves, (b) hardening curves of deformation modes, (c) relative activities during tensile deformation and (d) relative activities during compressive deformation.....	55
Figure 2.13	Inverse pole figure (IPF) map of AX60 alloy with deformed to $\epsilon = 2\%$ and 10% (Tensile loading is along RD).....	56
Figure 2.14	Microstructure and image quality map of AX60 alloy compressively deformed to $\epsilon = 2\%$ (a) microstructure of AX60 rolled at 350°C (a) microstructure of AX60 rolled at 450°C (c) image quality map of AX60 rolled at 350°C and (d) image quality map of AX60 rolled at 450°C.	57
Figure 2.15	Relationship between yield isotropy and CRSS ratio (tension twin/basal $\langle a \rangle$ slip) at initial deformation.	58
Figure 2.16	Relationship between Erichsen values and CRSS	

	ratio (tension twin/basal $\langle a \rangle$ slip) at initial deformation.....	58
Figure 2.17	The strain distribution along the RD according to Erichsen test of AX60 alloy rolled at 350°C and 450°C.....	61
Figure 2.18	Contribution of the deformation modes during Erichsen test of AX60 alloy rolled at 350°C and 450°C.....	61
Figure 2.19	Inverse pole figure (IPF) map of AX60 alloy after Erichsen test of 3.4mm..	62
Figure 2.20	Relationship between Erichsen values and CRSS ratio (tension twin/basal $\langle a \rangle$ slip) at 15% corresponding to 3.5mm of Erichsen value at center position.....	63
Figure 3.1	Microstructure of annealed Mg- x Al alloys; (a) A1, (b) A3, (c) A6 and (d) A9 alloy..	78
Figure 3.2	(0002) pole figures of annealed Mg- x Al alloys; (a) A1, (b) A3, (c) A6 and (d) A9 alloy...	78
Figure 3.3	VPSC simulation results of annealed Mg- x Al alloys; (a) experimental and simulated stress-strain curves, (b) hardening curves of deformation modes, (c) relative activities during tensile deformation	

	and (d) relative activities during compressive deformation.	79
Figure 3.4	Microstructure of annealed Mg-6Al- <i>x</i> Mn alloys; (a) AM603, (b) AM605, (c) AM607 and (d) AM61 alloy.	84
Figure 3.5	(0002) pole figures of annealed Mg-6Al- <i>x</i> Mn alloys; (a) AM603, (b) AM605, (c) AM607 and (d) AM61 alloy.	84
Figure 3.6	VPSC simulation results of annealed Mg-6Al- <i>x</i> Mn alloys; (a) experimental and simulated stress-strain curves, (b) hardening curves of deformation modes, (c) relative activities during tensile deformation and (d) relative activities during compressive deformation.	85
Figure 3.7	Microstructure of annealed Mg-6Al- <i>x</i> Ca alloys; (a) AX603, (b) AX605, (c) AX607 and (d) AX61 alloy.	90
Figure 3.8	(0002) pole figures of annealed Mg-6Al- <i>x</i> Ca alloys; (a) AX603, (b) AX605, (c) AX607 and (d) AX61 alloy.	90
Figure 3.9	VPSC simulation results of annealed Mg-6Al- <i>x</i> Ca alloys; (a) experimental and simulated stress-strain curves, (b) hardening curves of deformation modes,	

	(c) relative activities during tensile deformation and (d) relative activities during compressive deformation.	91
Figure 3.10	Microstructure of annealed Mg-6Al-xSn alloys; (a) AT61, (b) AT63, (c) AT65 and (d) AT67 alloy.	97
Figure 3.11	(0002) pole figures of annealed Mg-6Al-xSn alloys; (a) AT61, (b) AT63, (c) AT65 and (d) AT67 alloy. ..	97
Figure 3.12	VPSC simulation results of annealed Mg-6Al-xSn alloys; (a) experimental and simulated stress-strain curves, (b) hardening curves of deformation modes, (c) relative activities during tensile deformation and (d) relative activities during compressive deformation.	98
Figure 3.13	Microstructure of annealed Mg-6Al-xSr alloys; (a) AJ603, (b) AJ605, (c) AJ607 and (d) AJ61 alloy. .	103
Figure 3.14	(0002) pole figures of annealed Mg-6Al-xSr alloys; (a) AJ603, (b) AJ605, (c) AJ607 and (d) AJ61 alloy.	103
Figure 3.15	VPSC simulation results of annealed Mg-6Al-xSr alloys; (a) experimental and simulated stress-strain curves, (b) hardening curves of deformation modes, (c) relative activities during tensile deformation and (d) relative activities during compressive	

deformation	104
Figure 3.16 Microstructure of annealed Mg-6Al- <i>x</i> Zn alloys; (a) AZ603, (b) AZ61, (c) AZ62 and (d) AZ64 alloy. .	109
Figure 3.17 (0002) pole figures of annealed Mg-6Al- <i>x</i> Zn alloys; (a) AZ603, (b) AZ61, (c) AZ62 and (d) AZ64 alloy.	109
Figure 3.18 VPSC simulation results of annealed Mg-6Al- <i>x</i> Zn alloys; (a) experimental and simulated stress-strain curves, (b) hardening curves of deformation modes, (c) relative activities during tensile deformation and (d) relative activities during compressive deformation.	110
Figure 3.19 Average grain size of Mg-6Al- <i>X</i> alloys and the contents of alloying elements.....	113
Figure 3.20 Max. intensity of (0002) pole figure of Mg-6Al- <i>X</i> alloys and the contents of alloying elements.	113
Figure 3.21 Yield isotropy of Mg-6Al- <i>X</i> alloys and the contents of alloying elements.....	114
Figure 3.22 Yield isotropy of Mg-6Al- <i>X</i> alloys and the relative activity of tension twin in compression deformation at initial stage.	114
Figure 4.1 Microstructures of as-cast Mg-4Zn- <i>X</i> -Ca alloys; (a) Z4, (b) ZX40, (c) ZAX400, (d) ZWX400, (e)	

	ZCX400 and (f) ZSX400.	129
Figure 4.2	Microstructures of as-rolled Mg-4Zn-X-Ca alloys; (a) Z4, (b) ZX40, (c) ZAX400, (d) ZWX400, (e) ZCX400 and (f) ZSX400.	130
Figure 4.3	Microstructures of as-annealed Mg-4Zn-X-Ca alloys; (a) Z4, (b) ZX40, (c) ZAX400, (d) ZWX400, (e) ZCX400 and (f) ZSX400.....	131
Figure 4.4	(0002) pole figures of as-rolled Mg-4Zn-X-Ca alloys; (a) Z4, (b) ZX40, (c) ZAX400, (d) ZWX400, (e) ZCX400 and (f) ZSX400.....	134
Figure 4.5	(0002) pole figures of as-annealed Mg-4Zn-X-Ca alloys; (a) Z4, (b) ZX40, (c) ZAX400, (d) ZWX400, (e) ZCX400 and (f) ZSX400.....	135
Figure 4.6	Nominal strain-stress curves of Mg-4Zn-X-Ca alloys.	138
Figure 4.7	Circular blanks after Erichsen tests for Mg-4Zn-X- Ca alloys; (a) Z4, (b) ZX40, (c) ZAX400, (d) ZWX400, (e) ZCX400 and (f) ZSX400.....	140
Figure 4.8	Relationship between Erichsen values and yield strength of Mg alloy and New Mg-4Zn-X-Ca alloys (investigated alloys in present study).....	141
Figure 4.9	VPSC simulation results of annealed Mg-4Zn-X-	

Ca alloys rolled at 350°C; (a) experimental and simulated stress-strain curves, (b) hardening curves of deformation modes, (c) relative activities during tensile deformation and (d) relative activities during compressive deformation.....	145
Figure 4.10 Inverse pole figure (IPF) map of Z4 and ZX40 alloy with deformed to $\varepsilon = 2\%$ and 10% (Tensile loading is along RD)..	146
Figure 4.11 Relationship between activity of basal slip in compression at initial stage and (0002) max. intensity of basal texture.	149
Figure 4.12 Activity of basal slip in compression at initial stage and CRSS ratio (tension twin/basal $\langle a \rangle$ slip).....	149
Figure 4.13 Variation of yield isotropy and CRSS ratio (tension twin/basal $\langle a \rangle$ slip).....	150
Figure 4.14 Relationship between Erichsen values and yield isotropy.....	150
Figure 4.15 The strain distribution along the RD according to the Erichsen test of Z4 and ZX40 alloys.....	152
Figure 4.16 Contribution of the deformation modes during Erichsen test of Z4 and ZX40 alloys.....	152
Figure 4.17 Relationship between Erichsen values and CRSS	

ratio (tension twin/basal $\langle a \rangle$ slip) at 15%
corresponding to 3.5mm of Erichsen value at center
position.....153

Chapter 1. Introduction

1.1 Motivation

Magnesium is the lightest structural metal and has a density (1.74g/cm^3) of about 2/3 of that of aluminium and 1/4 of that of iron as shown in Table 1.1. Due to their superior physical and mechanical properties such as high specific strength, high damping capacity, excellent castability and workability, magnesium alloys become attractive in the transportation and electronic industries requiring lightweight materials. World demand for magnesium alloys has rapidly grown as shown in Figure 1.1. The use of lightweight magnesium components rapidly increased in the automotive industry due to growing interests in vehicle weight reduction and fuel efficiency. Most of the Mg and Mg alloys are mainly fabricated by casting process, especially die-casting because of lower production cost compared to that of wrought process such as extrusion, forging and rolling, etc. However, wrought Mg alloys have shown the high strength and high ductility through the rolling and extrusion process. Recently, it has been demonstrated that twin roll casting process could economically fabricate Mg alloy sheets with low cost and high production rate. TRC process is a combination of casting and rolling with one step processing which the molten metal can directly become thin Mg strip less than 10mm in thickness. TRC also provides fast solidification rate ($\sim 1.7 \times 10^3 \text{K/s}$) resulting in homogeneous distributed microstructure, grain refinement and extension of solid solubilities of alloying elements compared with conventional casting.

However, TRC Mg alloys normally require following multipass rolling for reducing the thickness of Mg sheets, resulting in formation of

strong basal texture during rolling. It is well known that such a strong basal texture could deteriorate formability of Mg alloy sheets at room temperature [1, 2]. In order to improve the formability, texture control from strong basal texture to non-basal texture should be required by development of new fabrication process or wrought Mg alloys. There have been a lot of studies carried out on severe deformation (SDF) such as equal channel angular extrusion (ECAE), differential speed rolling (DSR) and cross rolling to randomize the texture of Mg alloy sheets [1, 3-4]. Furthermore, there have been also lots of attempts to modify strong basal texture by addition by alloying elements which are related to modifying activity of deformation modes. P. Jason *et al.* [5] have studied the effect of Y content on Mg-Y alloys that Y alloying element could suppress the basal $\langle a \rangle$ slip with solute strengthening, and increase the activity of prismatic $\langle a \rangle$ cross slip with solute softening which are responsible for formation of weaker textures. H. Y. Wang *et al.* [6] has investigated that activation of basal $\langle a \rangle$ slip, pyramidal $\langle a \rangle$ and $\langle c+a \rangle$ slip could be improved by addition of Al and Sn via first-principles method. Y. Chino *et al.* [7] have shown that both the prismatic $\langle a \rangle$ and $\langle c \rangle$ slip are more active in Mg-Zn alloy by addition of Ca during rolling via TEM image analysis.

Recently, there have been extensive research efforts worldwide on the development of high plasticity wrought magnesium alloys to improve mechanical properties. Tensile properties of various commercial wrought magnesium alloys including WE43, AZ80 and ZK61 are summarized in Table 1.2. The majority of commercial wrought magnesium alloys do not have a good balance of strength and ductility, even though they contain expensive alloying elements such as rare-earth, silver, etc. Therefore, it is difficult to apply these alloys for commercial production of automobile

components. It is, therefore, essential to develop new high plasticity magnesium alloys with improved strength and ductility, compared to conventional alloys for wide-spread applications.

In order to develop new TRC Mg alloys with high formability and high strength, it is necessary to control microstructure and texture of the alloys with the addition of appropriate alloying elements. In order to improve the room temperature formability, it is important to understand relationship between formability and deformation behavior. In this research, VPSC simulations are carried out to predict deformation behavior of tensile and compressive deformation at various composition and processing conditions for developing new formable Mg alloys.

Table 1.1 Physical properties of magnesium and other metals

Elements	Mg	Fe	Al	Cu	Zn	Ti
Density [gr/cc]	1.74	7.87	2.71	8.94	7.13	4.51
Modulus [GPa]	45	211	70	130	108	120
Specific Modulus [nd]	26	27	26	14	15	26
Electrical Resistance at 20°C [$\mu\text{ohm/cm}$]	4.5	9.7	2.7	1.7	5.9	42.0
Thermal Conductivity 20-100°C [$\text{Wm}^{-1}\text{K}^{-1}$]	156	78	238	397	120	26
Thermal Expansion Coefficient 0-100°C [10^{-6}K^{-1}]	26.0	12.1	23.5	17.0	30.2	8.9
Melting Temp. [°C]	650	1538	660	1085	420	1668
Crystal Structure	hcp	bcc/fcc	fcc	fcc	hcp	hcp/bcc

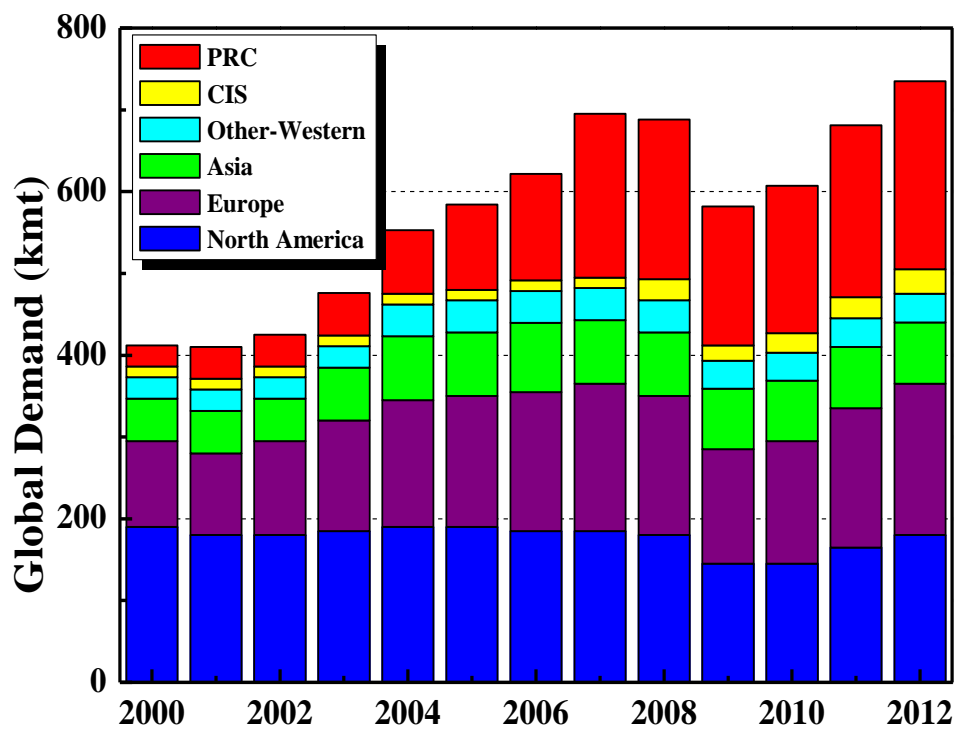


Figure 1.1 World magnesium consumption.

Table 1.2 Mechanical properties of commercial wrought magnesium alloys

Alloys	Type	Tensile Properties		
		Y.S. (MPa)	U.T.S. (MPa)	El. (%)
AZ31	Extrusion	200(F)	255(F)	12(F)
WE54	Extrusion	190 (T6)	275 (T6)	10 (T6)
WE43	Extrusion	160 (T6)	260 (T6)	15 (T6)
ZM21	Extrusion	160	245	10
AZ80	Forging	200 (T5)	290 (T5)	6 (T5)
ZK31	Extrusion	225	305	8
ZK61	Extrusion	210	285	6
HK31	Sheet	170 (H24)	230 (H24)	4 (H24)
HM21	Forging	175 (T5)	225 (T5)	3 (T5)
HZ11	Extrusion	120	215	7
LA141	Sheet	95 (T7)	115 (T7)	10 (T7)

1.2 Twin roll casting process

Twin roll casting is one of the continuous casting processes to fabricate strip plates from directly the melts, and a combination of casting and rolling process. Compared to direct chill casting process, it has lots of advantages to produce the near-net shape plates (Figure 1.2). It provides high cooling rate of 100 ~ 1,000K/s, which affects the microstructure such as expanding solid solubilities, grain refinements and controlling segregation. It could also decrease production costs by reducing the hot-rolling steps [8].

The TRC process was designed by Sir Henry Bessemer in 1846 and based concept of TRC process was patented in 1865, which combined the rolling and vertical casting process to fabricate steel plates. However, sound plates through the TRC process had been successfully fabricated by limitation of processing technologies such as development of refractory materials and controlling the level of melt (Figure 1.3).

Since then, a number of processing such as leveling, sensing and dynamic casting techniques had been significantly improved, and successfully fabricated the aluminum sheet for commercial products in 1950s. Technique of TRC Al was developed by Hunter Co., which adopted horizontal twin roll casting process, instead of vertical type process originally designed by Bessemer.

Fabrication of Mg alloy sheets at first time was carried out by Dow Chemical Co. with a proprietary molten Mg handling system in the 1980s. 200kg of magnesium plates and a thickness of 6 ~ 7mm was produced. However, the amounts of Mg alloy sheets were limited and the markets for magnesium sheets were not enough to be commercialization until 2000.

There have been many researches on TRC Mg alloy sheets carried out at Korea, Japan, China, Australia, Germany, Norway, Turkey and Canada for

commercialization of Mg alloy sheets with lab scale or pilot plant scale in the mid-2000s. Among the research groups, only POSCO and RIST at Korea has commercially produces Mg alloy sheets via TRC process and could produce a 16 ton of Mg sheets with a width of 2,000mm (Table 1.3) [8].

At present, many research groups and companies have studied on development of the TRC Mg alloys for commercialization in the world. Table 1.3 shows the list of research group and company which produce the Mg alloy sheets by TRC process.

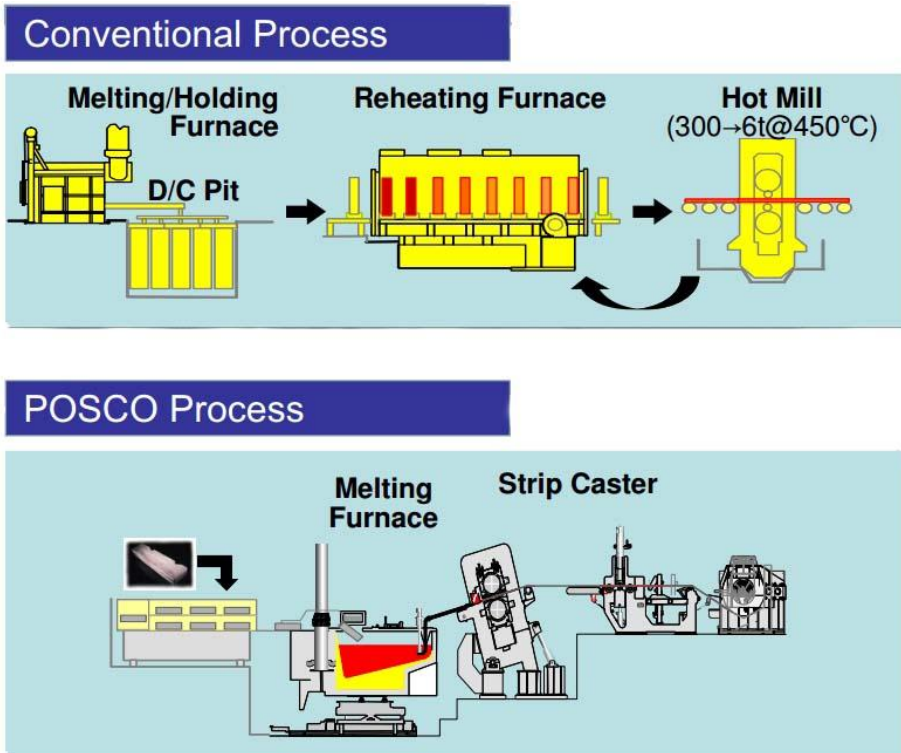


Figure 1.2 Conventional process vs. twin roll casting process in POSCO.

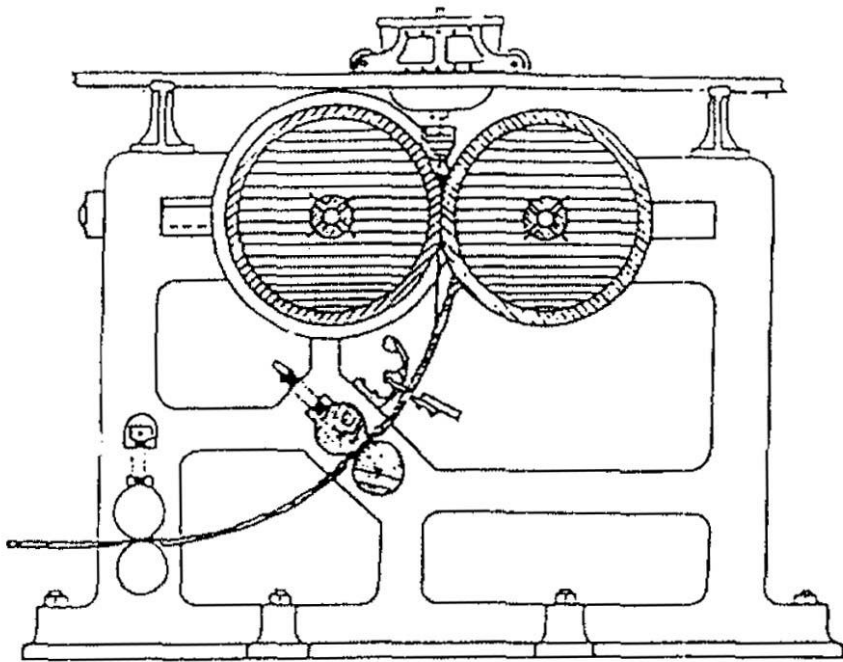


Figure 1.3 Schematic diagrams of Bessamer's twin roll caster [9].

Table 1.3 Research and development activities of TRC Mg [8]

Country	Company/Institute	Cast Strip Dimensions Width X Thickness (mm)
Korea	POSCO (RIST)	600 X 4~6
		2,000 X 4~8
Japan	Mitsubishi Aluminium	250 X 5
	Gonda Metal	400 X 2~6
China	Luoyang Copper	600 X 7
	Yinguang Magnesium	600 X 2~8
Australia	CSIRO	600 X 3~5
Germany	MgF	700 X 4~7
	HZG	600 X 4~7
Norway	Hydro Aluminium	700 X 4.5
Turkey	TUBITAK	1,500 X 4.5~6.5
Canada	CANMET	250 X 4~6

1.3 High formable wrought Mg alloys

Compared with cast Mg alloys, wrought Mg alloys show excellent ductility with grain refinement through the plastic deformation processes such as extrusion, rolling and press forging, and their mechanical properties expand the application of wrought Mg alloys in automobile and electronic industries which require the high strength properties for weight reduction. However, general wrought Mg alloys show poor formability at room temperature because of formation of the strong basal textures resulting from plastic deformation. In order to expand wide applications of wrought Mg alloys, development of high formable Mg alloys is needed. One of the ways to improve the formability is the addition of alloying elements such as RE, Li and Ca which plays a role in reduction of basal texture intensity. The high formability Mg alloys can be divided into various types such as Mg-RE alloys, Mg-Li alloys and Mg-Ca alloys.

○ Mg-RE Alloys

It is well known that addition of RE alloying elements such as Ce and Gd on Mg alloys could effectively reduce an intensity of (0002) pole figures and modify the basal texture of wrought magnesium alloys resulting in enhancement of formability at room temperature. For example, Mg-0.2Ce alloy shows the random texture and splitting of basal plane. Erichsen value of Mg-0.2Ce alloy is 4.0mm, which is more formable compared to Pure Mg with 3.1mm of Erichsen value. It is due to activation of prismatic $\langle a \rangle$ slip by Ce addition [10]. It has also been reported that formabilities of GZ21 and GZ31 alloys are 6.8 and 7.9mm, respectively, compared to AZ31 alloy which has 2.6mm of Erichsen value at room temperature. Improvement of formability in Mg-Gd-Zn alloys is related to excellent strain hardening capability with high

n value due to addition of Gd alloying elements [11].

○ Mg-Li Alloys

Addition of Li alloying element plays a vital role in weakening the basal texture and splitting the (0002) pole figures toward transverse direction. It has been reported that addition of Li below 5.5 wt.% could lower the c/a axial ratio resulting in more activation of non-basal slip system such as pyramidal $\langle c+a \rangle$ slip and prismatic $\langle a \rangle$ slip system. And addition of Li can reduce the energy of the stacking fault for stability of glissile dislocation configuration and affect the texture change by modification of deformation mechanisms [8] related to improving formability of Mg alloys. For example, formability of LAZ531 alloy is 5.1mm and that of AZ31 alloy is 3.2mm with Erichsen value [12]. The increase in formability of LAZ531 alloy can mainly be attributed to low c/a ratio and random texture with large n value.

○ Mg-Ca Alloys

It has recently been reported that the addition of Ca on Mg alloys can significantly reduce the intensity of basal texture with splitting (0002) pole figure to transverse direction. For example, basal textures of Mg-0.05Ca, Mg-0.1Ca and Mg-0.5Ca alloys show more random texture than that of Mg-3Zn alloy. The basal texture intensity of Mg-0.5Ca alloy is only 5.1. Compared to Mg-3Zn alloy which has the intensity of 26.1, Mg-xCa alloys exhibit the non-basal textures resulting in enhanced formability at room temperature [13]. It also shows that Erichsen values of Mg-0.05Ca, Mg-0.1Ca and Mg-0.5Ca alloys are 6.5, 9.1 and 7.1mm, respectively, which are quite formable in Mg wrought alloys.

1.4 Plastic deformation in Magnesium alloys

Plastic deformation of magnesium and magnesium alloys is quite complicated compared to FCC and BCC structure materials such as aluminium, copper and iron. Few studies of plastic deformation in Mg alloys are available. Due to hexagonal closed packed crystallographic structure, the number of active slip system is limited. Generally, magnesium and magnesium alloys accommodate the plastic deformation by mainly slip deformation and twin deformation. Slip deformation occurs when dislocation moves along the slip planes. Twin deformation occurs when atoms move distances proportional to their distance from the twin plane. In order to accommodate the plastic deformation, five independent slip systems are necessary, and twin deformation can play a vital role in increase the number of slip system by changing the texture. In case of room temperature deformation, basal slip system largely activates resulting in difficulty of c-axis strain. Therefore, slip deformation and twin deformation are competed and interacted on each other.

1.4.1 Slip deformation

As mentioned before, from the von Mises criterion, five independent slips are needed for accommodation of arbitrary plastic deformation in a polycrystalline material. In Mg and Mg alloys, basal slip that has only two independent slip systems is largely activated at room temperature due to its low critical resolved shear stress (CRSS) compared to that of non-basal slips. Otherwise, activation of pyramidal $\langle c+a \rangle$ slip system rarely occurs due to relatively high CRSS. Thus, it is necessary to activate four independent slip

modes by basal $\langle a \rangle$ and pyramidal $\langle c+a \rangle$ slips for arbitrary deformation in pure Mg and Mg alloys at room temperature.

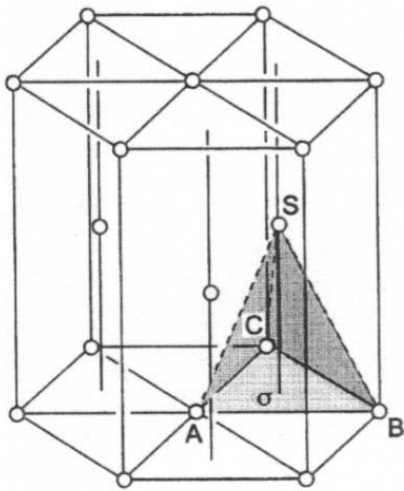
Table 1.4 shows the miller Bravais index and scale of burger vector b in Mg metal. In case of pure Mg single crystal, its burgers vector can be represented in Fig.1.4. From the Fig 1.5, dislocation with this burger vector can be glided on (0001), (1 $\bar{1}$ 00), (1 $\bar{1}$ 01) and (1 $\bar{1}$ 02) plane. It is also possible for non-basal slip system to glide the pyramidal planes. Slip occurs when applied stresses are higher than critical resolved shear stress (CRSS). The CRSS is affected by temperature, impurity and strain rate, etc. For plastic deformation at room temperature, the CRSS of basal slip is relatively lower than other slip system and twin modes. Therefore, basal slip is largely activated at room temperature. Basal slip can be generally observed at all the planes, however, prismatic slip is observed at high stress level.

Recently, there are lots of work done to activate the non-basal slip without the activation of basal $\langle a \rangle$ slip at tensile tests of Mg single crystal which is parallel to the basal slip plane to tensile loading direction. In this condition, it can be confirmed that prismatic $\langle a \rangle$ slip activated as a deformation mode. In addition, pyramidal $\langle a \rangle$ slip could contribute the plastic deformation at high temperature due to lowering its CRSS value. It have been reported by Reed-Hill and Robertson that activation of prismatic and pyramidal $\langle a \rangle$ slip observed at Mg single crystal that has the basal plane parallel to tensile loading direction of $\langle 10\bar{1}0 \rangle$ at tensile test with various temperature. T. Obara investigated that pyramidal $\langle c+a \rangle$ slip is activated at low temperature through the tensile and compressive tests. Koike *et al.* [14] showed that grain refinement is effective for activation of prismatic slip at grain boundary, because grain refinement promotes stress concentration at grain boundary, resulting in activation of prismatic slip. Detailed analysis in

his study shows that dislocation cross-slip to non-basal planes occurred at a yield isotropy value of only 1.1 instead of an expected value of 100. And also it reported that twin formation was observed in a 16% elongated sample and the activity of non-basal dislocation slip systems and the dynamic recovery were considered to be responsible for the large tensile ductility in the ECAE-processed AZ31 magnesium alloys. Therefore, it is necessary to understand the slip deformation of magnesium alloys in plastic deformation such as tensile and compressive deformation.

Table 1.4 Vector energies for the possible dislocation types in Mg metals.

Type of Dislocation	Number of Systems	Burgers Vector	Magnitude of Burgers Vector	Slip System	
a(AB)	3(2)	$\frac{1}{3}\langle 11\bar{2}0 \rangle$	$ a =3.209$	Basal	$\{0001\}\langle 11\bar{2}0 \rangle$
	3(2)			Prism-I	$\{10\bar{1}0\}\langle 11\bar{2}0 \rangle$
	6(4)			Pyramidal-I Pyramidal-II	$\{10\bar{1}1\}\langle 11\bar{2}0 \rangle$
c(ST)	3(2)	$\langle 0001 \rangle$	$ c =5.211$	Prism-I	$\{10\bar{1}0\}\langle 0001 \rangle$
	3(2)			Prism-II	$\{11\bar{2}0\}\langle 0001 \rangle$
c+a (ST + AB)	6(5)	$\frac{1}{3}\langle 11\bar{2}3 \rangle$	$\{ a ^2 + c ^2\}^{1/2} = 6.120$	Pyramidal-II	$\{11\bar{2}2\}\langle 11\bar{2}3 \rangle$



AB = perfect (unit) dislocation
 $A\sigma$ = Shockley partial type

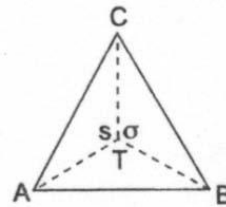
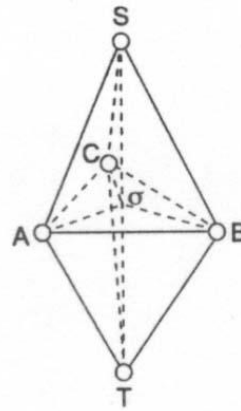


Figure 1.4 Burgers vector in the hexagonal close-packed lattice.

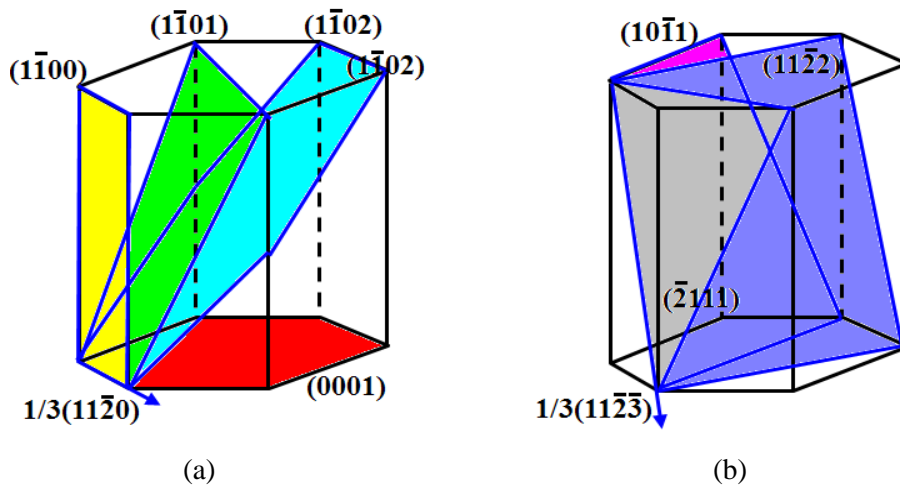


Figure 1.5 Theoretically possible slip modes in magnesium, colored surfaces represent each slip planes, arrows represent slip direction Burgers vectors. (a) $\langle a \rangle$ type slip systems, (b) $\langle c+a \rangle$ type slip systems.

1.4.2 Twinning system

Twin deformations in magnesium play a critical role in accommodating the deformations. For example, formation of twin at room temperature is only a way to accommodate the deformation along the c-axis at Mg alloys with coarse microstructure. Fig. 1.6 shows the relationship between twinning shear and axial ratio in HCP metals. In case of magnesium, tension twin is mainly generated and compression twin is secondarily occurred in compression deformation. It is also indicated that the slope of linear line determine the twin deformations. If some metal have the negative slope, tension twin is generated when c-axis is in tension, and compression twin occurs when load is applied to compress the c-axis.

Generally, the invariant plane of this shear is called K_1 and the shear direction η_1 ; the second undistorted plane is K_2 , the plane containing η_1 and the normal to K_1 and K_2 is the plane of shear. The crystallographic elements, K_1 , K_2 , η_1 and η_2 , the four compound twin systems are well known. Figure 1.7 shows the relationship between K_1 , K_2 , η_1 and η_2 .

Several types of twin modes were reported in Mg single crystals including the $\{10\bar{1}1\}$, $\{10\bar{1}2\}$, $\{10\bar{1}3\}$, $\{10\bar{1}5\}$, $\{30\bar{3}2\}$, and $\{30\bar{3}4\}$ type [15-16]. Double twinning of the $\{10\bar{1}1\}$ - $\{10\bar{1}2\}$, $\{10\bar{1}2\}$ - $\{10\bar{1}2\}$ and $\{10\bar{1}3\}$ - $\{10\bar{1}2\}$ types were found to be a particular feature of twins with $\{10\bar{1}2\}$ re-twinning in the primary twin interior and the preferential alignment of primary twins [17-18]. Table 1.5 lists the detailed information about misorientation between the matrix and the corresponding twin types. Among them, the $\{10\bar{1}2\}$ twin and $\{10\bar{1}1\}$ twin have been far the most observed twinning mode in Mg metals. It was reported that the $\{10\bar{1}2\}$ tensile twinning requires only 2 to 3MPa, while the $\{10\bar{1}1\}$ compressive twin requires 70 to

140MPa [19]. Reed–Hill and Robertson reported the onset of twinning at a tensile stress of 4MPa, which corresponds to the resolved shear stress of 2 MPa, i.e. reversal of the η_1 direction will not produce a twin [20]. This means that for a single crystal of given orientation with respect to a uni-axially applied stress, some variants of particular twin mode should operate only in tension, whereas others should operate only in compression.

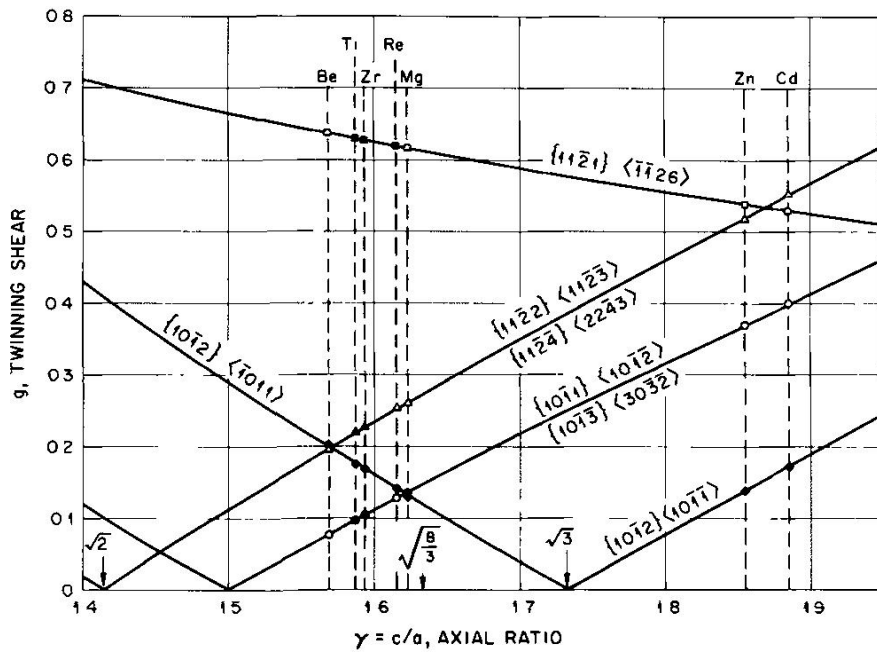


Figure 1.6 Variation of twinning shear with the axial ratio for the hexagonal metals. A filled symbol indicates that the twin mode is an active mode [21].

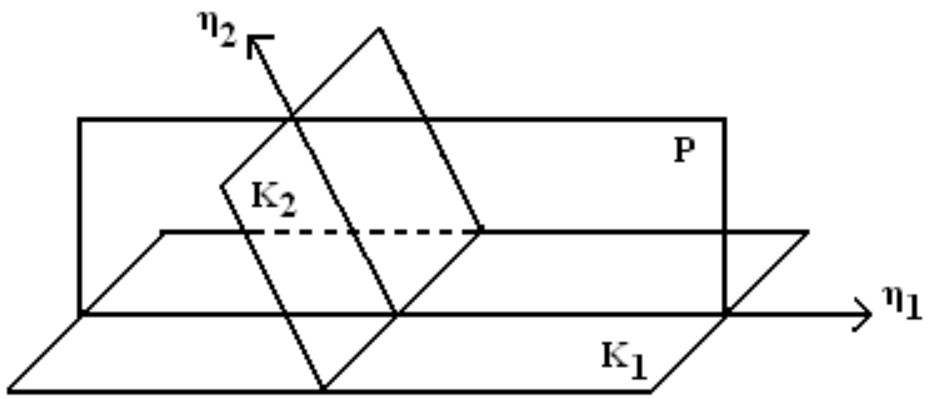


Figure 1.7 Relationship between planes K_1 , K_2 , and directions η_1 , η_2 .

Table 1.5 Twin type and corresponding misorientation angle in Magnesium crystal [22].

Type of Twin	Misorientation Angles/Axis
$\{10\bar{1}1\}$	$56.2^\circ \langle 1\bar{2}10 \rangle$
$\{10\bar{1}2\}$	$86.3^\circ \langle 1\bar{2}10 \rangle$
$\{10\bar{1}3\}$	$64^\circ \langle 1\bar{2}10 \rangle$
$\{10\bar{1}5\}$	$41^\circ \langle 1\bar{2}10 \rangle$
$\{30\bar{3}2\}$	$39.2^\circ \langle 1\bar{2}10 \rangle$
$\{30\bar{3}4\}$	$70.8^\circ \langle 1\bar{2}10 \rangle$
$\{10\bar{1}1\}-\{10\bar{1}2\}$	$37.5^\circ \langle 1\bar{2}10 \rangle$
$\{10\bar{1}1\}-\{10\bar{1}2\}$	$30.1^\circ \langle 1\bar{2}10 \rangle$
$\{10\bar{1}1\}-\{10\bar{1}2\}$	$66.5^\circ \langle 5\bar{9}43 \rangle$
$\{10\bar{1}1\}-\{10\bar{1}2\}$	$69.9^\circ \langle 2\bar{4}21 \rangle$
$\{10\bar{1}2\}-\{10\bar{1}2\}$	$7.4^\circ \langle 1\bar{2}10 \rangle$
$\{10\bar{1}2\}-\{10\bar{1}2\}$	$60^\circ \langle 10\bar{1}0 \rangle^a$
$\{10\bar{1}2\}-\{10\bar{1}2\}$	$60.4^\circ \langle \bar{8}170 \rangle^b$
$\{10\bar{1}3\}-\{10\bar{1}2\}$	$22.2^\circ \langle 1\bar{2}10 \rangle$

Bibliography

1. X. Huang, K. Suzuki, A. Watazu, I. Shigematsu, N. Saito, "Improvement of formability of Mg-Al-Zn alloy sheet at low temperatures using differential speed rolling", *J. Alloys Compd*, 470 (2009) pp. 263-268.
2. D. Wu, R. S. Chen, E. H. Han, "Excellent room-temperature ductility and formability of rolled Mg-Gd-Zn alloy sheets", *J. Alloys Comp.* 509 (2011) pp. 2856-2863.
3. T. Mukai, M. Yamanoi, H. Watanabe, K. Higashi, "Ductility enhancement in AZ31 magnesium alloy by controlling its grain structure", *Scripta Mater.* 45 (2001) pp. 89-94.
4. Y. Chino, J. S. Lee, K. Sassa, A. Kamiya, M. Mabuchi, "Press formability of a rolled AZ31 Mg alloy sheet with controlled texture", *Mater. Letters* 60 (2006) pp. 173-176.
5. J. P. Hadorn, K Hantzsche, S. Yi, J. Bohlen, D. Letzig, "Role of solute in the texture modification during hot deformation of Mg-RE alloys", *J. A. Wollmershauser, S. R. Agnew, Metall. Mater. Trans. A* 43 (2012) pp. 1347-1362.
6. H. Y. Wang, N. Zhang, C. Wang, Q. Jiang, "First-principles study of the generalized stacking fault energy in Mg-3Al-3Sn alloy", *Scripta Mater.* 65 (2011) pp. 723-726.
7. Y. Chino, T. Ueda, Y. Otomatsu, K. Sassa, X. Huang, K. Suzuki, M. Mabuchi, "Effects of Ca on tensile properties and stretch formability at room temperature in Mg-Zn and Mg-Al alloys", *Mater. Trans.* 52 (2011) pp. 1477-1482.
8. C. Bettles, M. Barnett, "Advances in wrought magnesium alloys", Woodhead Publishing, (2012).

9. Y. S. Han, H. I. Lee, "Strip casting technology", *J. Korean Foundrymen's Soc.* 9 (1989), pp. 20-28.
10. Y. Chino, M. Kado, M. Mabuchi, "Enhancement of tensile ductility and stretch formability of magnesium by addition of 0.2wt% Ce", *MSE A* 494 (2008) pp. 343-349.
11. D. Wu, R. S. Chen, E. H. Han, "Excellent room-temperature ductility and formability of rolled Mg-Gd-Zn alloy sheets", *J. Alloys Comp.* 509 (2011) pp. 2856-2863.
12. Q. Yang, B. Jiang, J. Li, H. dong, W. Liu, S. Luo, F. Pan, "Modified texture and room temperature formability of magnesium alloy sheet by Li addition", *Int. J. Mater. Form.* (2015).
13. J. Y. Lee, Y. S. Yun, W. T. Kim, D. H. Kim, "Twinning and texture evolution in binary Mg-Ca and Mg-Zn alloys", *Met, Mater, Int.*, 20 (2014) pp. 885-891.
14. J. Koike, T. Kobayashi, T. Mukai, H. Watanabe, M. Suzuki, K. Maruyama, K. Higashi, "The activity of non-basal slip systems and dynamic recovery at room temperature in fine-grained AZ31B magnesium alloys", *Acta Mater.* 51 (2003), pp. 2055-2065.
15. H. Yoshinaga and R. Horiuchi, "Deformation Mechanisms in Magnesium Single Crystals Compressed in the Direction Parallel to Hexagonal Axis", *Trans. JIM.*, 4 (1963), pp. 1-8.
16. L Jiang, J.J. Jonas, A.A. Luo, A.K. Sachdev and S. Godet, "Twinning-induced Softening in Polycrystalline AM30 Mg Alloy at Moderate Temperatures", *Scripta Mater.*, 54 (2006), pp. 771-775.
17. M R. Barnett, Z. Keshavarz, A.G. Beer and X. Ma, "Non-Schmid Behaviour during Secondary Twinning in a Polycrystalline Magnesium Alloy", *Acta Mater.*, 56 (2008), pp. 5-15.

18. L Jiang, J.J. Jonas, A.A. Luo, A.K. Sachdev and S. Godet, "Influence of $\{10\bar{1}2\}$ Extension Twinning on the Flow Behavior of AZ31 Mg Alloy", *Mater. Sci. Eng. A*, 445-446 (2007), pp. 302-309.
19. J Koike, "Enhanced Deformation Mechanisms by Anisotropic Plasticity in Polycrystalline Mg Alloys at Room Temperature", *Metall. Mater. Trans. A*, 36 (2005), pp. 1689-1696.
20. R E. Reed-Hill and W.D. Robertson, "Additional Modes of Deformation Twinning in Magnesium", *Acta Metal.*, 5 (1957), pp. 717-727.
21. M. H. Yoo, "Slip, Twinning, and Fracture in Hexagonal Close-Packed Metals", *Meter. Trans. A*, 12 (1981), pp.409-418.
22. M. Z. Bian, "Plastic Deformation Behavior of Magnesium Single Crystals", Ph. D. Thesis, (2013)

Chapter 2. Analysis of the solidification and deformation behavior of TRC Mg-6Al-X alloys

2.1 Introduction

Mg alloys are known for being light structure materials that can be used in the automobile industry to reduce CO₂ emission and improve fuel efficiency due to its high specific strength and high specific stiffness, among others [1-2]. However, of the formability of Mg alloys at room temperature is very low compared to that of Al alloys due to limitations in deformation modes from its crystal structure, which is a hexagonal close-packed (HCP) crystal [3]. In order to expand the application of Mg alloys, high formability Mg alloys should be developed with a high production rate and low production cost. Recently, the TRC process has fabricated near-net shape sheets with high productivity and some of the Mg alloy sheets have been successfully produced commercially through the TRC process, which is the combination of casting and hot-rolling [4]. However, TRC Mg alloys - mostly Mg-Al-Zn based alloys - have poor surface quality in TRC sheets caused by segregation and show limited formability at room temperature due to strong basal texture by plastic deformation [5-6]. Therefore, new TRC Mg alloys should consider less volume segregation during casting and enhanced formability by modifying the basal texture.

The centerline or inverse segregation formation in TRC samples may be closely related to solidification behaviors affected by processing parameters such as roll speed, separating force, melt temperature, and setback distance [5]. To ensure a good quality surface with less segregation, lots of TRC simulation should be conducted to predict the solidification behavior and

optimize the processing parameters before casting. Bae *et al.* [7] have examined the roll speed and nozzle depth effect on temperature distribution by a finite difference method (2D). Zeng *et al.* [8] have studied casting speed and processing gap during the horizontal twin roll casting by a computational fluid dynamics model. Park [9] has investigated the nozzle thickness effect on solidification behavior by finite element method (FEM) code. Most of the TRC simulation studies have focused mainly on the effects of processing parameters on the solidification in Mg alloys. However, it is important to elucidate the effect of alloying elements on the solidification behavior of Mg alloys to develop suitable TRC Mg alloys, which show less tendency to segregate.

It is well known that such strong basal textures could deteriorate the formability of Mg alloy sheets at room temperature, which results from restrictions in slip systems to accommodate the thickness strain during sheet forming [10]. Additionally, (0002) intensity of pole figure in Mg alloy increases during plastic deformation [11]. For TRC Mg alloy sheets, a multi-pass rolling process could be required to obtain the desired thickness and strong basal texture during rolling. Therefore, the development of a new fabrication process or alloying element addition is necessary to control the strong basal texture to random texture, resulting in modifying the deformation mode activity. Suzuki *et al.* [12] have shown that high temperature rolling could modify strong basal textures to random textures in Mg alloys. In addition, there are many attempts to modify the strong basal texture by adding alloying elements like rare earth (RE), Ca, or Sr [13-15]. Nakano *et al.* [3] have shown that adding Zn and Ca enhanced the mobility of prismatic dislocation compared to that of basal $\langle a \rangle$ slip. However, the effects of rolling temperature and alloying elements on deformation

behaviors of the TRC Mg alloys have not yet been investigated by viscoplastic self-consistent (VPSC) simulation.

In the present study, TRC simulations of Mg-6Al-X alloys are performed to understand the segregation tendency by utilizing the DEFORM software. TRC Mg-6Al-X alloys are produced with different compositions. The microstructure and mechanical properties were examined by optical microscopy and tensile tests. Textural evolution of TRC Mg-6Al-X alloys was examined by analyzing X-ray diffraction. In order to predict deformation behavior, VPSC simulations were carried out in tension and compression deformations based on these experimental results.

2.2 Experimental Procedures

TRC simulations of Mg-6Al-X alloys were carried out by a commercial FEM code DEFORM software in order to predict the liquid fraction distribution during casting. For TRC simulation, specific heat, thermal conductivity, latent heat, and solid fraction were inputted and calculated by JMatPro software. Alloys with nominal compositions (in wt.%) of Mg-6Al-0.3Mn (A6), Mg-6Al-0.3Ca-0.3Mn (AX60), Mg-6Al-0.3Sr-0.3Mn (AJ60), and Mg-6Al-0.3Zn-0.3Mn (AZ60) were subjected to the TRC process at laboratory scale. The alloys were melted at 700~710°C using a steel crucible under CO₂ and SF₆ gas mixture and transferred to the preheated nozzle held at 650°C. This was followed by twin roll casting at 3m/min where the roll gap was set at 2.0mm and TRC sheet thickness was around 3.0 ~ 3.3mm. TRC sheets were subsequently homogenized at 400°C for 12hr and then followed by water quenching. The analyzed chemical composition of the homogenized sheets was given in Table 2.1. The homogenized sheets were hot rolled at 350°C and 450°C for 4pass with a total rolling reduction of 65%. Before hot rolling, the sheets were preheated at 350°C and 450°C for 30min. The rolled sheets were subsequently annealed at 350°C for 1hr before water quenching. The tensile tests and compression tests were performed at a strain rate of 2×10^{-4} /sec according to the ASTM standard B557M using the Instron 5582 machine. The loading axis was parallel to the rolling direction. The stretch formability of the sheets was evaluated by the Erichsen cupping test using graphite type lubricant. The punch diameter and speed were 20mm and 5mm/min (55mm square type specimen), respectively. Pole figures of annealed sheets were measured from four different planes: $\{10\bar{1}0\}$, $\{0002\}$, $\{10\bar{1}1\}$, and $\{11\bar{1}0\}$ using the Schulz

reflection method by a PANalytical X'Pert PRO X-ray diffractometer with Cu K α source. The macro-texture was analyzed on the mid-thickness planes perpendicular to the normal direction. Complete pole figures were acquired from the orientation distribution function (ODF) calculated using the arbitrarily defined cells (ADC) method in the LaboTex 3.0 software. The texture of deformed samples was characterized using EBSD using FE-SEM (SU70, HITACHI) fitted with a TSL EBSD camera operating at 20kV, 70° tilting angle. VPSC simulations were conducted for both tension and compression deformation in order to predict the contribution of various deformation modes. Voce-type hardening rule and Predominant Twin Reorientation Scheme (PTR) model were used for the hardening and twinning model, respectively.

Table 2.1. Chemical composition of TRC Mg-6Al-X alloys.

Alloys	Compositions (wt.%)							
	Al	Mn	Ca	Sr	Zn	Ni	Fe	Mg
A6	6.0920	0.1422	-	-	-	0.031	0.0071	Bal.
AX60	5.9900	0.1978	0.3019	-	-	0.0031	0.0103	Bal.
AJ60	5.9060	0.1324	-	0.2680	-	0.0036	0.0083	Bal.
AZ60	5.6440	0.2534	-	-	0.3286	0.0045	0.0110	Bal.

2.3 Results and discussions

2.3.1 TRC simulation and thermodynamic calculations

Prior to twin roll casting, the TRC simulations of Mg-6Al-X alloys are carried out to predict the solidification behavior. The casting speed, roll diameter, initial roll temperature, melt temperature, and heat-transfer coefficient are set at 140mm, 3m/min, 20°C, 670°C, and 16kW/m²C, respectively, for simulations. Fig. 2.1 presents the liquid fraction distribution of Mg-6Al-X alloys during casting. The distance between the melt and roll nip point is 64.6mm, 48.9mm, 58.2mm, and 34.6mm for A6, AX60, AJ60, and AZ60 alloys, respectively. These are closely related to segregation tendency. The A6 alloy has the longest distance compared to other alloys, resulting in less segregation tendency due to its highest thermal conductivity. The AJ60 alloy also has the longer distance resulting from fast heat transfer between liquid and roll surface. It is due to high thermal conductivity of AJ60 alloy. The thermal conductivity of A6 alloy is 58.93W/mK and that of AJ60 alloy is the same. However, that of the AX60 and AZ60 alloy is less than 58.93W/mK. It makes different solidification behavior during TRC. The AZ60 alloy has the shortest distance and expected to form more segregation areas in TRC alloys due to thermodynamic properties, especially in the solidification range [5]. In fact, the AZ60 alloy has the longest solidification range (liquidus ~ solidus temperature) of 223.8°C among the alloys, which may affect the mushy zone size related to macro-segregation like centerline segregation and/or inverse segregation, which are harmful to surface quality and mechanical properties of TRC Mg alloys. Therefore, the AZ60 alloy has the tendency to segregate, and the other alloys have less tendency to segregate, which is suitable for the TRC process. Fig. 2.2 shows

the results of Mg-6Al-X alloy thermodynamic calculation used PanDat7.0 software to predict the solidification sequence and second phase types. During the TRC process, molten metal rapidly solidified through the copper chilled rolls. Thus, the diffusion in solids is significantly limited. The Scheil model for solidification calculations is utilized in the present study. From the calculations, the Al_8Mn_5 phase is precipitated before forming the α -Mg matrix in all alloys. The $\text{Mg}_{17}\text{Al}_{12}$ phase is formed at the last stage. Al_8Mn_5 and $\text{Al}_{11}\text{Mn}_4$ phases are present in thermodynamic calculations and can affect the microstructure of TRC Mg-6Al-X alloys due to their high thermal stability. For A6 alloy, the second phases consist of $\text{Mg}_{17}\text{Al}_{12}$, Al_8Mn_5 , and $\text{Al}_{11}\text{Mn}_4$ phases. However, the mole fraction of second phases is nearly occupied by $\text{Mg}_{17}\text{Al}_{12}$, suggesting that centerline segregation of the A6 alloy may consist mainly of the α -Mg matrix and $\text{Mg}_{17}\text{Al}_{12}$ phase. For the AX60 alloy, the $(\text{Mg}, \text{Al})_2\text{Ca}$ phase is newly formed at $464.1 \sim 437.7^\circ\text{C}$ from adding Ca due to low solubility in Mg-6Al-X alloys, as shown in Fig. 2.2 (b). In addition, the AX60 alloy has a higher mole fraction in the $\text{Mg}_{17}\text{Al}_{12}$ phase compared to the A6 alloy. The AX60 alloy segregation largely consists of the α -Mg matrix, $\text{Mg}_{17}\text{Al}_{12}$, and $(\text{Mg}, \text{Al})_2\text{Ca}$ phases, resulting in more segregation compared to the A6 alloy. For the AJ60 alloy, Al_4Sr and $\text{Al}_{38}\text{Mg}_{58}\text{Sr}_4$ phases are newly precipitated compared to the A6 alloy, as shown in Fig. 2.2 (c). The mole fraction of these second phases is not considerable, but such precipitates could change the strong basal texture due to particle stimulated nucleation [16]. For the AZ60 alloy, there are no new second phases compared to the A6 alloy due to the high Zn solubility in the Mg-6Al alloy. The liquid solubility of Zn in Mg-6Al alloy is 4.9 wt.%, and that of Ca and Sr is only 0.005 and 0.014wt.%, respectively. This indicates that Zn content could be soluble in a α -Mg matrix. However, adding Zn to

the Mg-6Al alloy increases the solidification range from 182.9°C to 223.8°C, resulting in more centerline segregations during the TRC process [5].

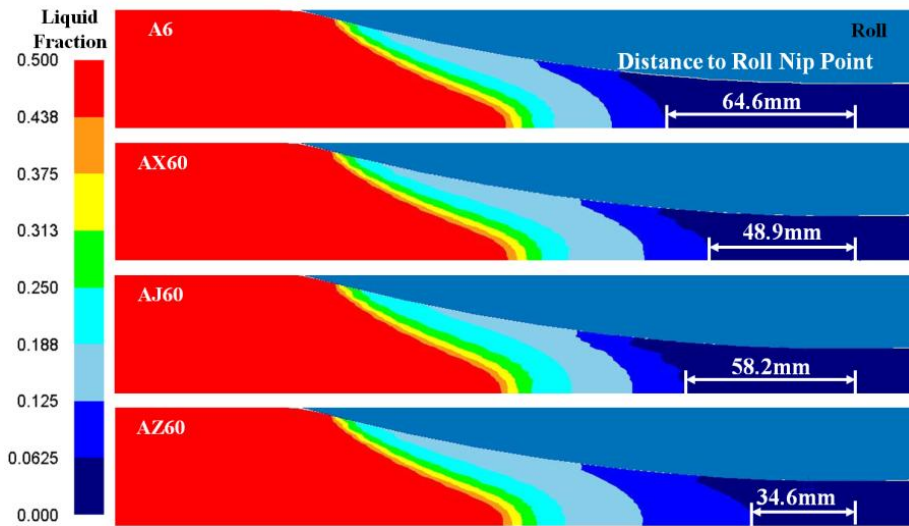


Figure 2.1 Distribution of liquid fraction on Mg-6Al-X alloys; (a) A6, (b) AX60, (c) AJ60 and (d) AZ60.

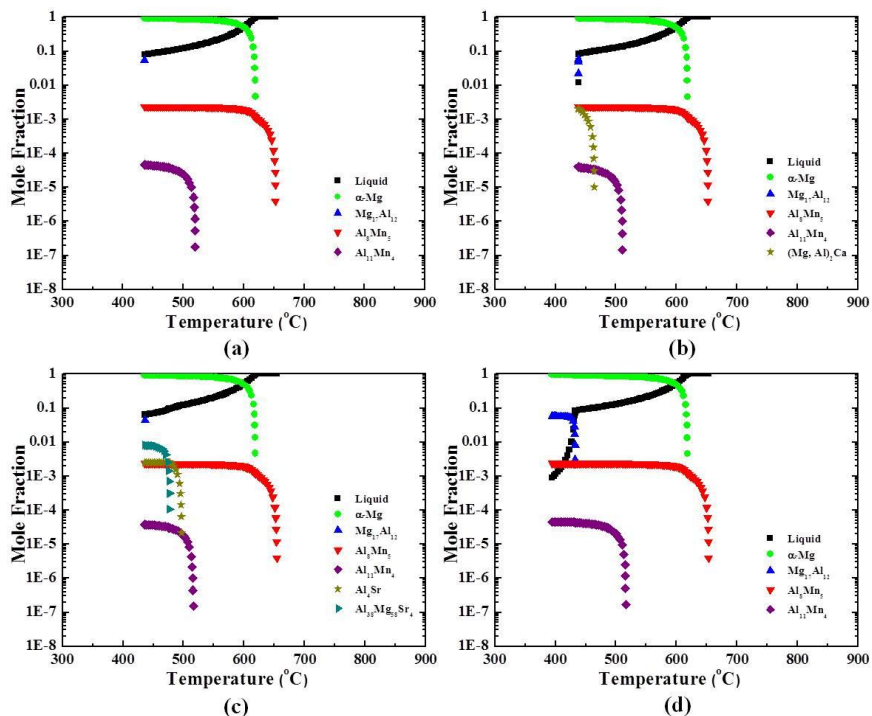


Figure 2.2 Solidification behavior of Mg-6Al-X alloys; (a) A6, (b) AX60, (c) AJ60 and (d) AZ60.

2.3.2 Microstructural evolution

Fig. 2.3 shows the cross-sectional micrographs of TRC Mg-6Al-X alloys in as-cast condition. All the alloys show the centerline segregation formation along the casting direction. However, A6, AX60, and AJ60 alloys exhibit deformation segregates types while the AZ60 alloy shows channel segregation due to different solidification behaviors [17]. Furthermore, the centerline segregation area (%) of TRC Mg alloys are measured by an image analyzer software where the segregation area is 1.9%, 2.1%, 2.2%, and 3.4% for A6, AX60, AJ60, and AZ60 alloys, respectively. These results confirm that the segregation area measured in the real microstructure matches the distance between the melt and roll nip point calculated from TRC simulation in Fig. 2.4. In general, centerline segregation is mainly affected by thermal and thermodynamic properties [18]. A6 and AJ60 alloys have higher thermal conductivity and shorter solidification ranges that lead to faster cooling rates during casting. However, the AZ60 alloy has the longest solidification range and the lowest α -Mg mole fraction, which could be attributed to easy segregation formation. Fig. 2.5 presents the optical micrographs of annealed Mg-6Al-X alloys rolled at 350°C. All the Mg alloys exhibit a fully annealed and uniform equiaxed grain structure. Annealed A6 alloy appears to have a coarse grain with 14.8 μ m. Yet, AX60 and AJ60 alloys exhibit fined microstructures with 9.9 and 8.7 μ m, respectively, suggesting that the Ca and Sr addition is effective for grain refinement on the Mg-6Al alloy. Fig. 2.6 shows the optical micrographs of annealed Mg-6Al-X alloys rolled at 450°C. Compared to previous microstructures, the grain growth of Mg-6Al-X alloys occurs after the annealing process. When the rolling temperature increases from 350°C to 450°C, the average grain size increases from 14.8 to 19.0, 9.9

to 14.0, 8.7 to 10.9 and 10.8 to 15.6 μm for A6, AX60, AJ60, and AZ60 alloys, respectively. The coarse microstructure formation may be attributed to the rolling temperature caused by second phase dissolution to a matrix at higher rolling temperatures [19]. AX60 and AJ60 alloys show smaller grain sizes at both rolling temperatures of 350°C and 450°C in comparison to other alloys. The formation of thermally stable second phases such as $(\text{Mg}, \text{Al})_2\text{Ca}$ and Al_4Sr may play a role in impeding movements in the grain boundary during hot rolling.

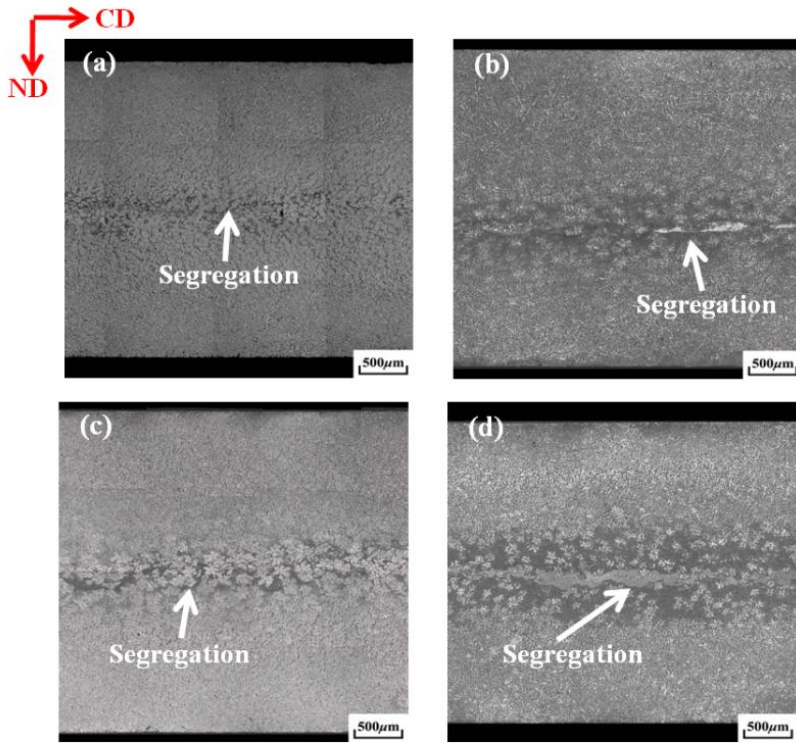


Figure 2.3 Microstructures of as-cast Mg-6Al-X alloys; (a) A6, (b) AX60, (c) AJ60 and (d) AZ60.

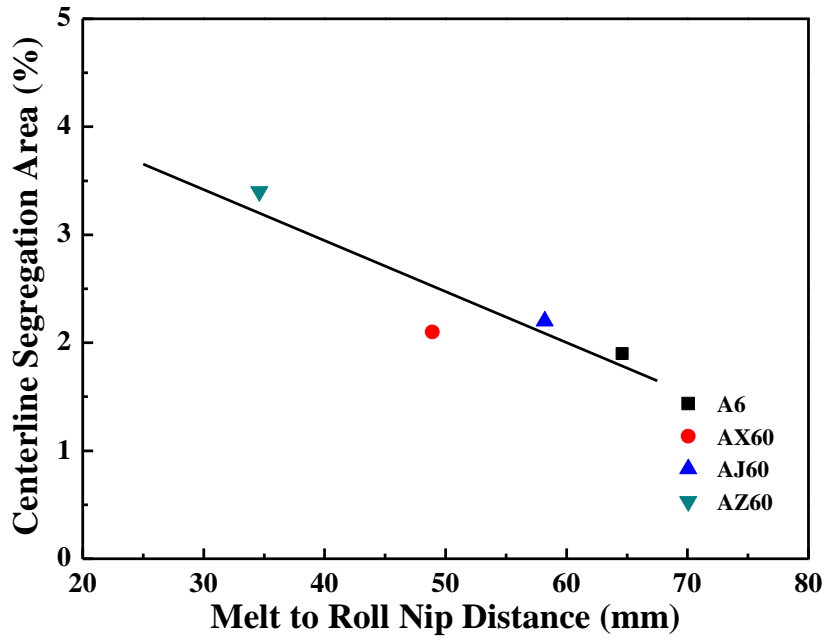


Figure 2.4 Relationship between centerline segregation area and melt to roll nip distance of Mg-6Al-X alloys.

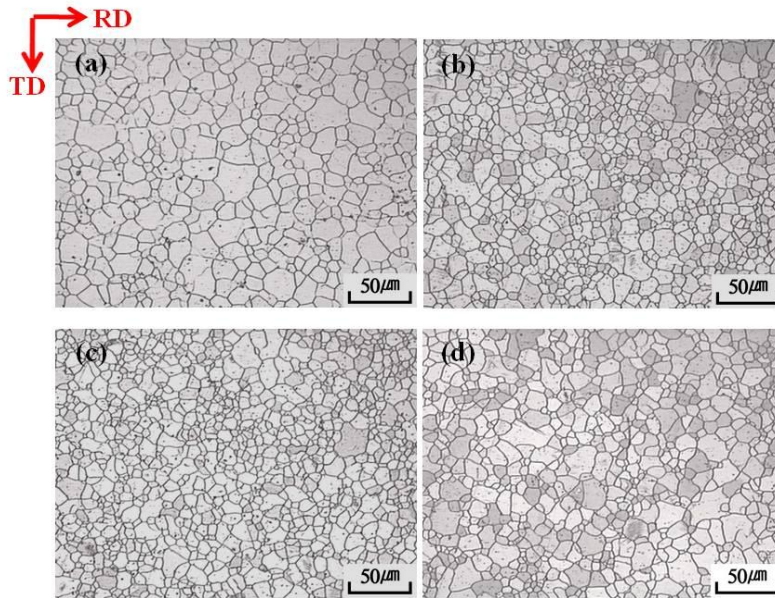


Figure 2.5 Microstructures of annealed Mg-6Al-X alloys rolled at 350°C; (a) A6, (b) AX60, (c) AJ60 and (d) AZ60.

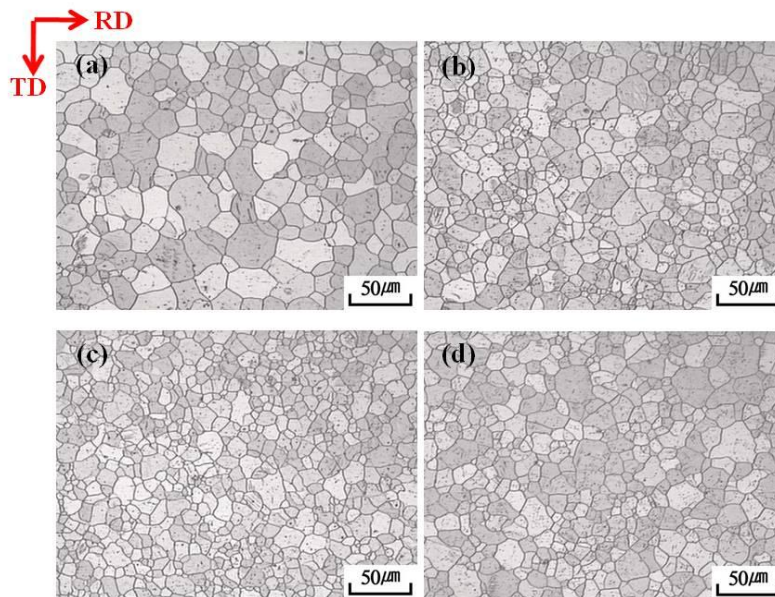


Figure 2.6 Microstructures of annealed Mg-6Al-X alloys rolled at 450°C; (a) A6, (b) AX60, (c) AJ60 and (d) AZ60.

2.3.3 Texture evolution

Fig. 2.7 shows (0002) pole figures of annealed Mg-6Al-X alloys rolled at 350°C. Most basal poles are parallel to the normal direction with slightly tilting basal poles from the normal direction (ND) to transverse direction (TD), which shows the typical annealed Mg alloy texture. The (0002) pole figure intensities of A6, AX60, AJ60, and AZ60 alloys are 9.223, 8.345, 8.104, and 9.203, respectively. It is interesting to note that AX60 and AJ60 alloys exhibit weaker textures while A6 and AZ60 alloys show strong basal textures. The weaker texture formation with AX60 and AJ60 may be related to size misfit in Mg and reducing stacking fault energy by adding Ca or Sr elements, which result in non-basal slip system activation [15]. In addition, the atomic size ratio is +0.20% and +0.33% for Ca/Mg and Sr/Mg, respectively, resulting in a strong solute drag effect to accelerate the dynamic recrystallization by PSN or interactions between lattice defects like dislocations and twins [20-21]. Therefore, adding such elements could lead to weaker basal Mg alloy textures. Fig. 2.8 exhibits (0002) pole figures of annealed Mg-6Al-X alloys rolled at 450°C. There are significant changes in texture intensities compared to previous textures. The intensities of (0002) pole figures are largely reduced 2~3 times. In particular, the AJ60 alloy is reduced from 8.104 to 2.787 and all basal textures show a broad angular distribution of basal planes from the ND towards the TD, which could be formable at room temperature and influence the deformation mode activation. It has been reported that increasing the rolling temperature decreases the (0002) pole figure intensity of Mg alloys due to non-basal slip system activation caused by lower CRSS values at higher temperatures [12].

Therefore, Ca and Sr element addition and high temperature rolling play vital roles in weakening the strong basal Mg alloy textures.

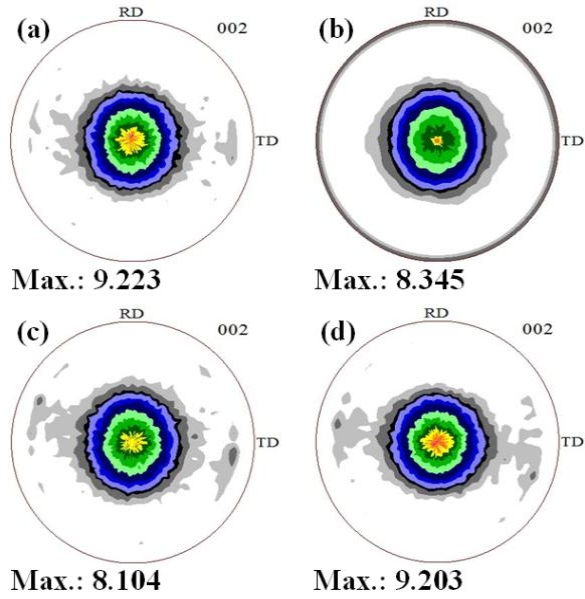


Figure 2.7 (0002) pole figures of annealed Mg-6Al-X alloys rolled at 350°C;
 (a) A6, (b) AX60, (c) AJ60 and (d) AZ60.

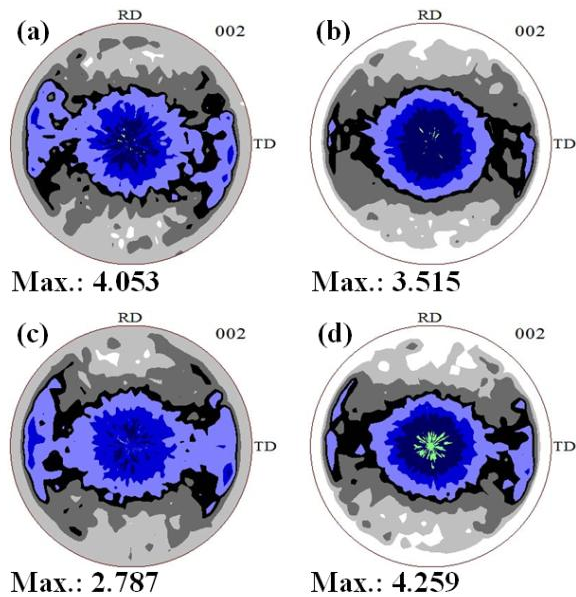


Figure 2.8 (0002) pole figures of annealed Mg-6Al-X alloys rolled at 450°C;
 (a) A6, (b) AX60, (c) AJ60 and (d) AZ60.

2.3.4 Mechanical properties and formability

Fig. 2.9 exhibits the tensile and compressive properties of annealed Mg-6Al-X alloys rolled at 350°C. The solid lines and dashed lines indicate tensile and compressive stress-strain curves, respectively. The AX60 alloy shows the highest yield strength of 199.8MPa and ultimate strength of 308.7MPa with elongation of 16.4% due to the fine microstructure compared to other alloys shown in Fig. 2.4. Furthermore, all the alloys show strong yield asymmetry of 0.58 ~ 0.62 (CYS/TYS) caused by tension twin activation with low strain hardening rates at compressive deformations [22]. In general, the tension twin occurs in compression, parallel to the basal planes, or in tension, parallel to the c-axis. Therefore, a strong basal texture could easily induce tension twin formation in compression deformation, resulting in strong yield isotropy. All the mechanical properties and formability of the Mg-6Al-X alloys are summarized in Table 2.2. The formabilities of Mg-6Al-X alloys are approximately 3.3 ~ 3.4mm, which are the typical Erichsen values of Mg alloys. The AX60 alloy is expected to stretch more at room temperature compared to other alloys, because of the random texture, as shown in Fig. 2.7. However, the AX60 alloy formability is only 3.4mm, which may be related to higher yield strength and lower strain hardening compared to other alloys. Fig. 2.10 shows the tensile and compressive properties of annealed Mg-6Al-X alloys rolled at 450°C. As the tensile stress-strain curves, yield strength (YS), and ultimate tensile strength (UTS) of Mg-6Al-X alloys steadily decrease while the elongation and strain hardening exponent significantly increase with increasing rolling temperature, Mg alloys with higher n values exhibit enhanced formability due to large uniform elongation [23]. It is interesting to note that when the rolling temperature increases from 350 to 450°C, the

compressive yield strength slightly increases, resulting in enhanced yield isotropy with coarse grain sizes compared to previous rolling conditions. It has been reported that when the grain size decreases, the compressive yield strength gradually increases, resulting in enhanced yield isotropy with low fraction of the twin area [24]. However, CYS of Mg-6Al-X alloys increases when the grain size of annealed alloys increases. This may be related to changes from strong basal texture to random texture, which could affect deformation mode activation. More random textures are not favorable for stress states with tension twin initiation in compression deformation. Therefore, Mg alloys that depict random textures could enhance the yield isotropy by modifying deformation modes with coarse grain sizes. In addition, assessing the formability of annealed alloys rolled at 450°C is carried out by Erichsen tests, which reveals that formability of alloys increases approximately 1.5~1.7 times compared to previous rolling conditions. When compared to commercial AZ31 alloy, alloys containing Sr or Ca elements show higher formability with Erichsen values of 5.6mm and 5.3mm for AJ60 and AX60 alloys, respectively.

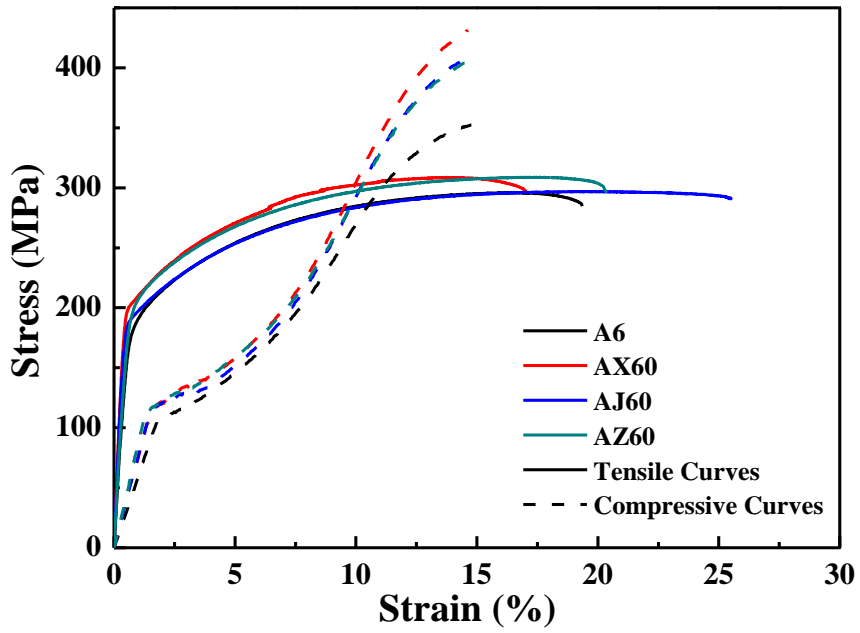


Figure 2.9 Nominal strain-stress curves of annealed Mg-6Al-X alloys rolled at 350°C.

Table 2.2 Mechanical properties and formability of annealed Mg-6Al-X

alloys

Rolling Temperature	Alloys	Tensile Properties				Compressive Properties		Yield Isotropy	Formability
		Y. S. (MPa)	U. T. S. (MPa)	Elongation (%)	n	Y. S. (MPa)	Max. S. (MPa)	C.Y.S./T.Y.S.	Erichsen Value (mm)
350°C	A6	175.8	295.9	18.5	0.223	102.8	352.9	0.58	3.3
	AX60	199.8	308.7	16.4	0.209	112.1	432.1	0.56	3.4
	AJ60	186.9	296.8	24.3	0.212	116.5	412.1	0.62	3.4
	AZ60	191.3	308.7	19.3	0.208	118.1	408.6	0.62	3.4
450°C	A6	140.4	286.6	20.3	0.309	110.2	306.6	0.78	4.8
	AX60	151.7	295.7	19.7	0.267	124.3	339.9	0.82	5.3
	AJ60	146.3	278.3	23.4	0.283	117.3	330.1	0.80	5.7
	AZ60	149.8	285.2	21.1	0.283	122.1	346.3	0.82	5.2

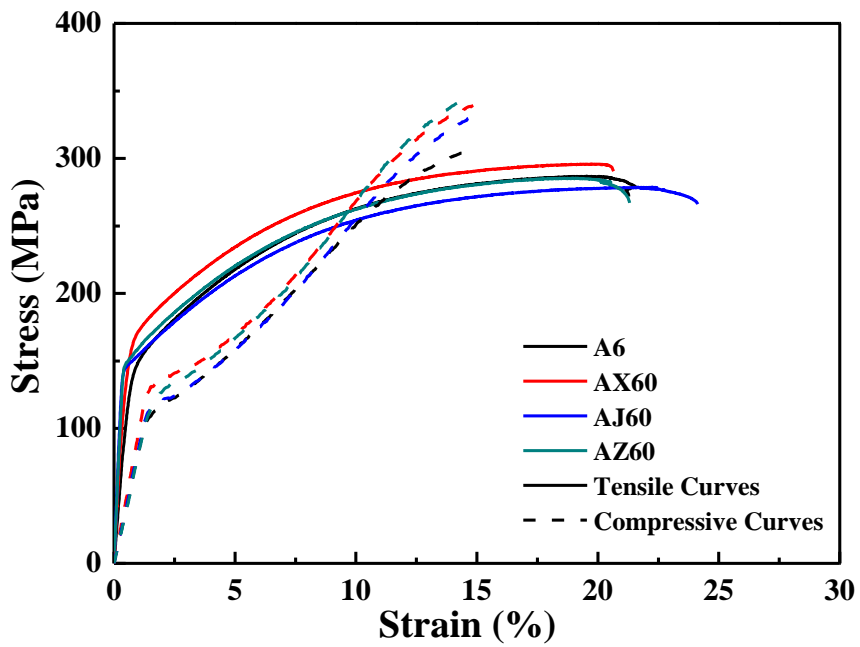


Figure 2.10 Nominal strain-stress curves of annealed Mg-6Al-X alloys rolled at 450°C.

2.3.5 VPSC simulations

As mentioned previously, there is a close relationship between the Ericksen value and intensity of (0002) pole with the yield isotropy of Mg-6Al-X alloys. When yield isotropy increases or the intensity of basal texture decreases, the formability of Mg alloys at room temperature steadily increases. This may be associated to the contribution of activated deformation modes during deformation. In order to analyze the relative activity of deformation modes, VPSC simulations of annealed Mg-6Al-X alloys are carried out on tensile and compressive deformation with 1,000 orientations. Fig. 2.11 (a) illustrates both simulated and experimental tensile and compressive strain stress-curves of annealed alloys rolled at 350°C, which are well matched. Fig. 2.11 (b) shows the hardening curves of various deformation modes with accumulated shear strains. All the alloys show that the basal $\langle a \rangle$ slip has the smallest CRSS value while the compressive twin has the highest CRSS value, which are observed in Mg single crystals [26]. Among the four different alloys, the AX60 alloy has the highest initial CRSS of basal $\langle a \rangle$ slip while the A6 alloy exhibits the lowest initial CRSS of basal $\langle a \rangle$ slip caused by grain refinement, resulting in higher tensile and compressive yield strength with Ca alloying element addition. Fig. 2.11 (c) and (d) present the relative activities of various deformation modes on tensile and compressive deformation, respectively. In terms of tensile deformation, all the alloys show that basal $\langle a \rangle$ slip and prismatic $\langle a \rangle$ slip largely accommodate the deformation. The relative activity of pyramidal $\langle c+a \rangle$ slip significantly increases at the last deformation stage due to its low hardening rate [27]. In addition, basal $\langle a \rangle$ slip and tension twin are the main deformation modes at entire strains during compressive deformation and pyramidal $\langle c+a \rangle$ slip are largely activated over

the 10% strain. The AX60 and AJ60 alloys, which have more random texture, have more active basal $\langle a \rangle$ slip and pyramidal $\langle c+a \rangle$ slip. Fig. 2.12 (a) shows both simulated and experimental tensile and compressive strain stress-curves of annealed alloys rolled at 450°C. The simulation results agree with the experimental flow curves at both tensile and compressive deformation. Fig. 2.12 (b) shows the threshold stress of Mg-6Al-X alloys with accumulated shear strain. The initial CRSS of basal $\langle a \rangle$ slip are similar to that of Mg-6Al-X alloys rolled at 350°C while CRSS of tension twin slightly increases by approximately 10MPa due to tension twinning suppression during compression deformation. For tensile deformation, basal $\langle a \rangle$ slip and prismatic $\langle a \rangle$ slip are dominant deformation modes while the pyramidal $\langle c+a \rangle$ slip is important in accommodating the strain as tensile deformation proceeds, as shown in Fig. 2.12 (c). Compared to the alloys rolled at 350°C, there are significant increases in the relative activity of basal $\langle a \rangle$ slip. In addition, AX60 and AJ60 alloys show more relative activity of basal $\langle a \rangle$ slip among the four alloys caused by more random textures, which indicates that thickness strain could be accommodated by the basal $\langle a \rangle$ slip activation during deformation. It is also found that basal $\langle a \rangle$ slip and tension twin mainly accommodated plastic deformation during compressive deformation, as shown in Fig.2.12 (d). With increasing rolling temperature, the initial relative activity of basal $\langle a \rangle$ slip increases from 0.534 to 0.711, from 0.516 to 0.718, from 0.553 to 0.678 and from 0.503 to 0.636 for A6, AX60, AJ60, and AZ60 alloys, respectively. However, the relative activity of tension twin in compression mode significantly decreases compared to that of the 350°C results. Fig. 2.13 shows the formation of deformation twins with increasing the amount of tensile strain from 2% to 10%. AX60 rolled at 350°C has the area fraction of tension twins increases from 0.51% at 2% strain to 0.67% at

10% strain. AX60 rolled at 450°C with more random texture has the area fraction of tension twins increases from 0.29% at 2% strain to 1.06% at 10% strain. Generally, it is not easy to form the tension twin during tensile test because of unfavorable orientation between matrix and tensile loading direction. It is suggested that the formation of tension twin during tensile test along the RD is caused by operation of compressive stress along the TD [25]. It also can be seen that tension twins are active at tension mode and important deformation mode at initial stage resulting to texture evolution in VPSC simulation. Mg alloys with smaller grain sizes have higher compressive strengths due to grain boundary strengthening [24]. However, Mg-6Al-X alloys rolled at 450°C show the increased compressive yield strength caused by initial CRSS increase of tension twin compared to that of Mg alloys rolled at 350°C due to suppression of tension twin during the compression deformation as shown in Fig. 2.14 (a)-(d). This is attributed to improved yield isotropy of Mg alloys, as shown in Fig 2.10. Fig. 2.15 shows the relationship between yield isotropy and initial CRSS ratio (tension twin/basal $\langle a \rangle$). Furthermore, it shows that yield isotropy is a linear relationship with CRSS ratio, indicating that a large CRSS ratio is needed to achieve enhanced yield isotropy. Fig. 2.16 shows the relationship between Erichsen values and CRSS ratio (tension twin/basal $\langle a \rangle$ slip) in initial deformation. The formability of Mg alloys increases at room temperature as the CRSS ratio of (tension twin/basal $\langle a \rangle$ slip) increases, which is associated with modifying deformation modes.

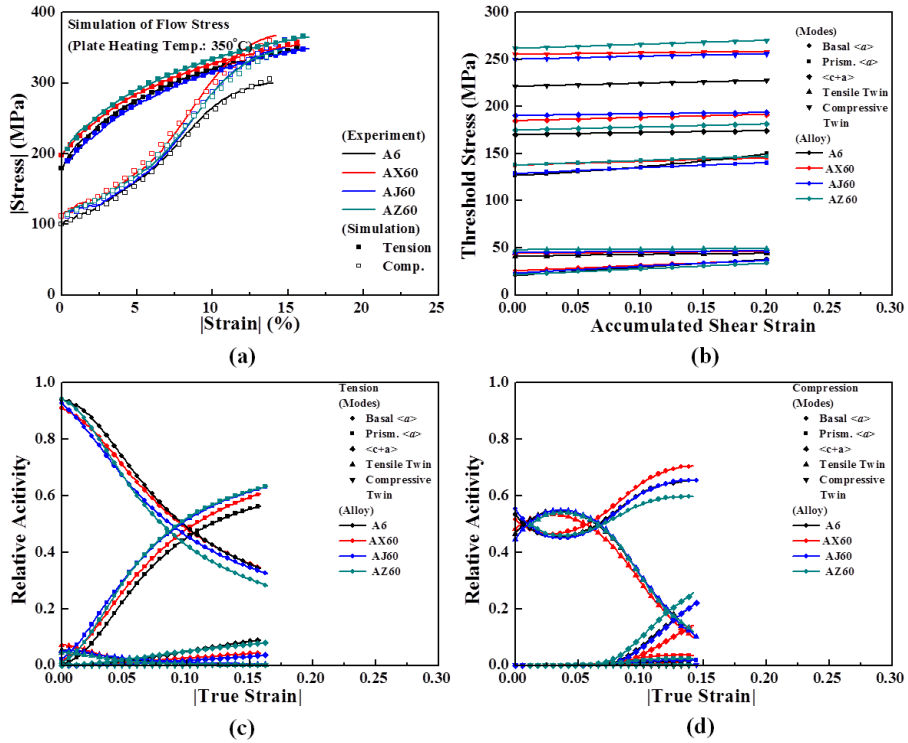


Figure 2.11 VPSC simulation results of annealed Mg-6Al-X alloys rolled at 350°C; (a) experimental and simulated stress-strain curves, (b) hardening curves of deformation modes, (c) relative activities during tensile deformation and (d) relative activities during compressive deformation.

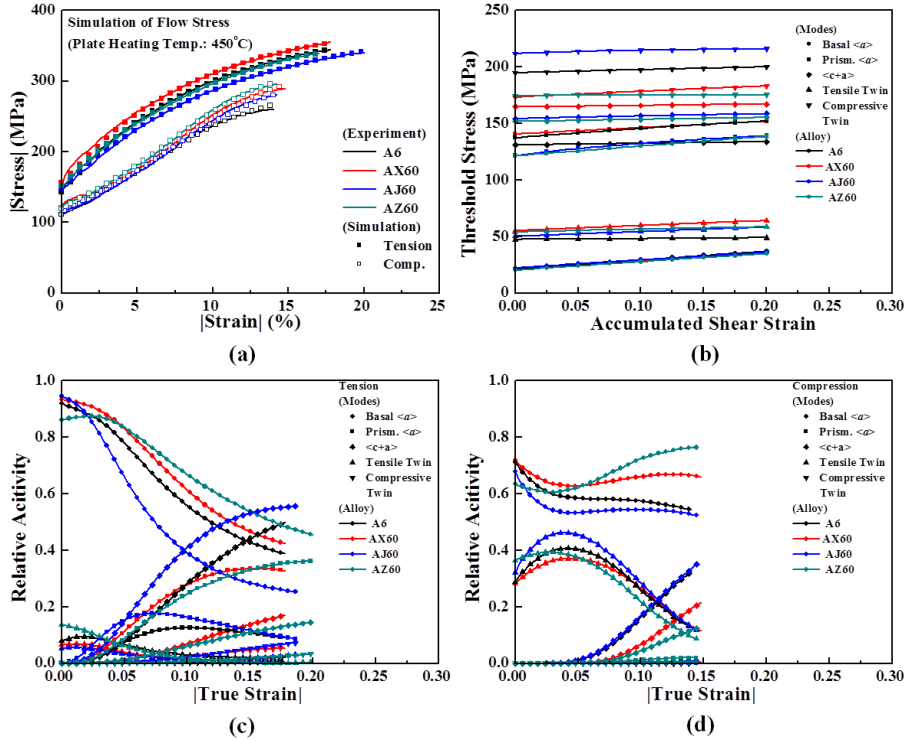


Figure 2.12 VPSC simulation results of annealed Mg-6Al-X alloys rolled at 450°C; (a) experimental and simulated stress-strain curves, (b) hardening curves of deformation modes, (c) relative activities during tensile deformation and (d) relative activities during compressive deformation.

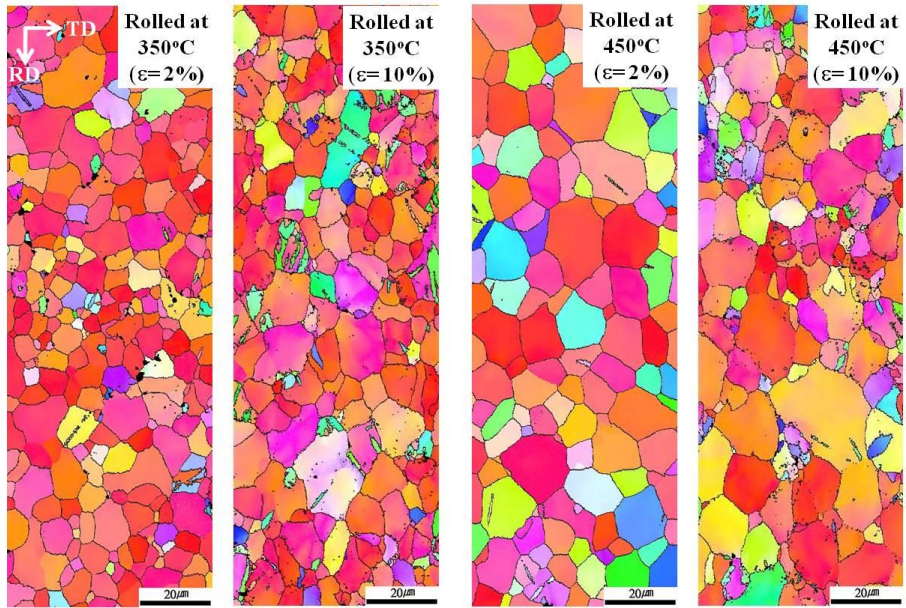


Figure 2.13 Inverse pole figure (IPF) map of AX60 alloy with deformed to $\epsilon = 2\%$ and 10% (Tensile loading is along RD).

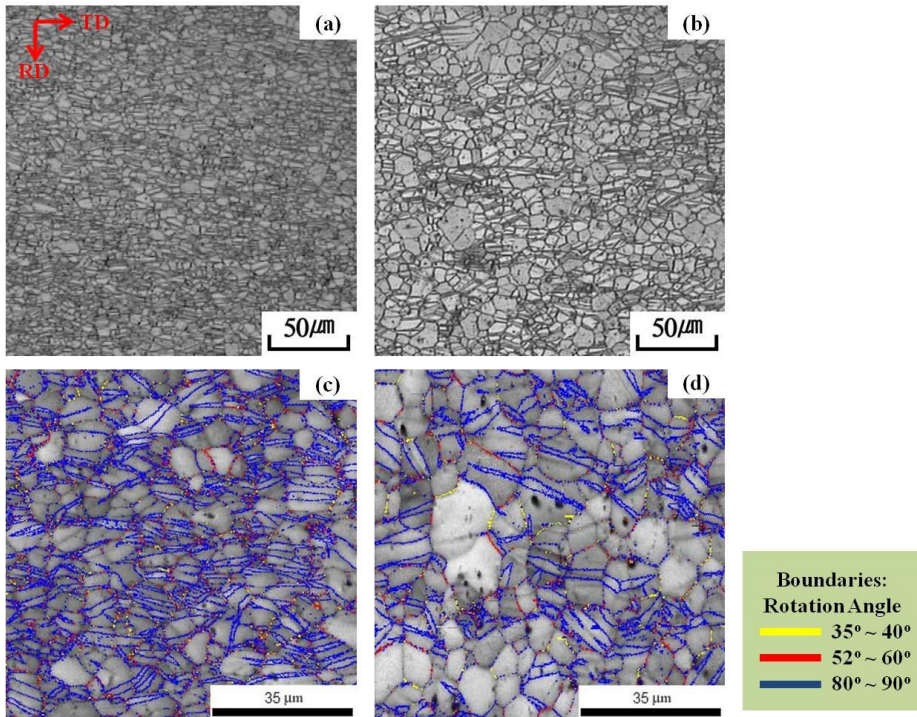


Figure 2.14 Microstructure and image quality map of AX60 alloy compressively deformed to $\epsilon = 2\%$ (a) microstructure of AX60 rolled at 350°C (b) microstructure of AX60 rolled at 450°C (c) image quality map of AX60 rolled at 350°C and (d) image quality map of AX60 rolled at 450°C.

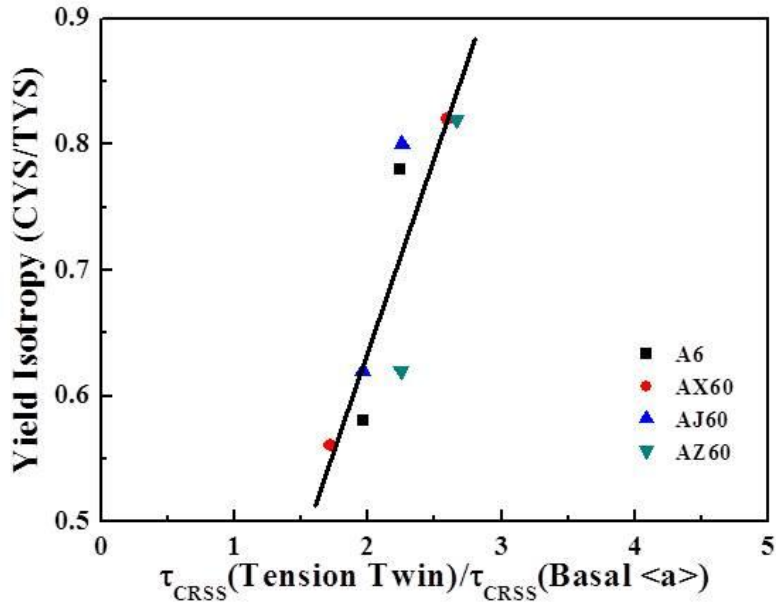


Figure 2.15 Relationship between yield isotropy and CRSS ratio (tension twin/basal $\langle a \rangle$ slip) at initial deformation.

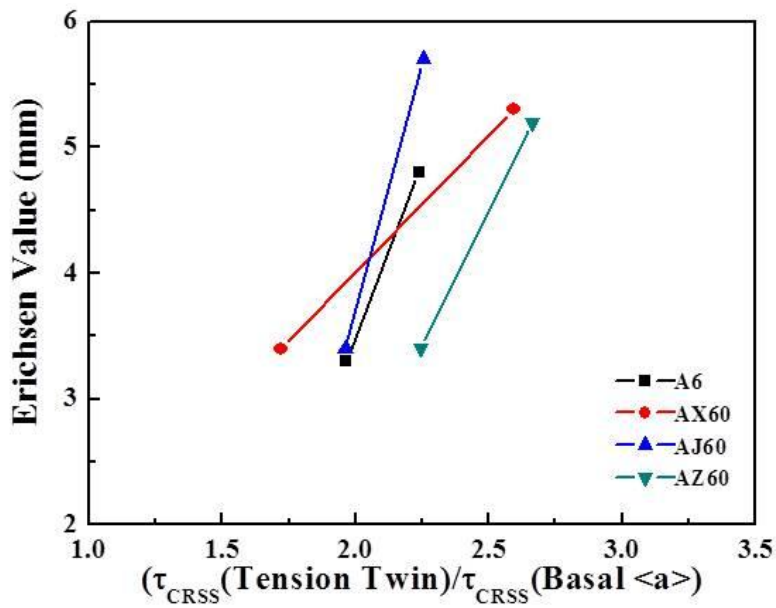


Figure 2.16 Relationship between Erichsen values and CRSS ratio (tension twin/basal $\langle a \rangle$ slip) at initial deformation.

2.3.5 Finite element simulation during Erichsen test

To understand the deformation behavior during Erichsen test, finite element method with VPSC polycrystal model has been conducted. In order to carry out the Erichsen simulation, 1,000 grains, 1,199 meshes in sheet and 0.12 shear friction coefficient between sheet and punch are used. Fig. 2.17 shows the strain distribution of annealed AX60 alloy rolled at 350°C and 450°C. It indicates that maximum effective strain of AX60 rolled at 350°C steadily increases from 0.21 to 0.48mm/mm with increasing Erichsen value from 2mm to 8mm. In addition, max. effective strain of AX60 rolled at 450°C is 0.18 and 0.43mm/mm which are more formable compared to AX60 rolled at 350°C. Fig. 2.18 shows the relative activity of AX60 alloy during Erichsen test. Main deformation modes are basal $\langle a \rangle$ slip, $\langle c+a \rangle$ slip and tension twin. However, most strains are accommodated to basal $\langle a \rangle$ slip. In case of “A” position, more relative activity of basal $\langle a \rangle$ slip occurs at AX60 alloy rolled at 450°C due to random texture which are favorable orientation to activate the basal $\langle a \rangle$ slip. With the increase of strain, the relative activity of basal $\langle a \rangle$ slip decreases, and that of $\langle c+a \rangle$ slip gradually increases. Similar result is observed at “B” position. At initial stage, basal $\langle a \rangle$ slip is quite important to accommodate the strain. As the process goes on, the relative activity of basal $\langle a \rangle$ slip decreases, however, that of $\langle c+a \rangle$ slip increases. Fig. 2.19 shows the inverse pole figure map of Z4 and ZX40 alloy after Erichsen test of 3.4mm. It shows that AX60 alloys rolled at 450°C has more volume fraction of tension twin compared to AX60 alloy rolled at 350°C. It also can be seen that more relative activity of tension twin during Erichsen simulation is observed at AX60 alloy rolled at 450°C. It is due to favorable orientation to activate the tension twin under the biaxial tension stress under Erichsen test. Fig. 2.20

shows the relationship between Erichsen values and CRSS ratio (tension twin/basal $\langle a \rangle$ slip) in 15% which are corresponded to 3.5mm of Erichsen value at center of AX60 alloy. The formability of Mg alloys increases at room temperature as the CRSS ratio of tension twin to basal $\langle a \rangle$ slip increases, which is associated with modifying deformation modes. Consequently, highly formable Mg alloys can be achieved by modifying deformation behaviors, which are significantly affected by alloying elements and processing parameters.

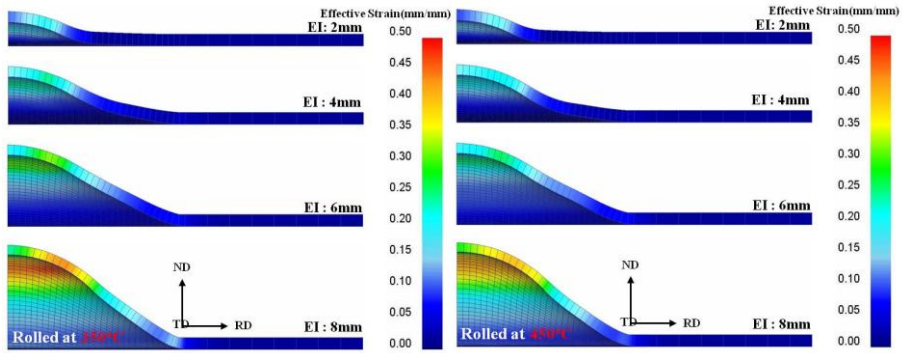


Figure 2.17 The strain distribution along the RD according to Erichsen test of AX60 alloy rolled at 350°C and 450°C.

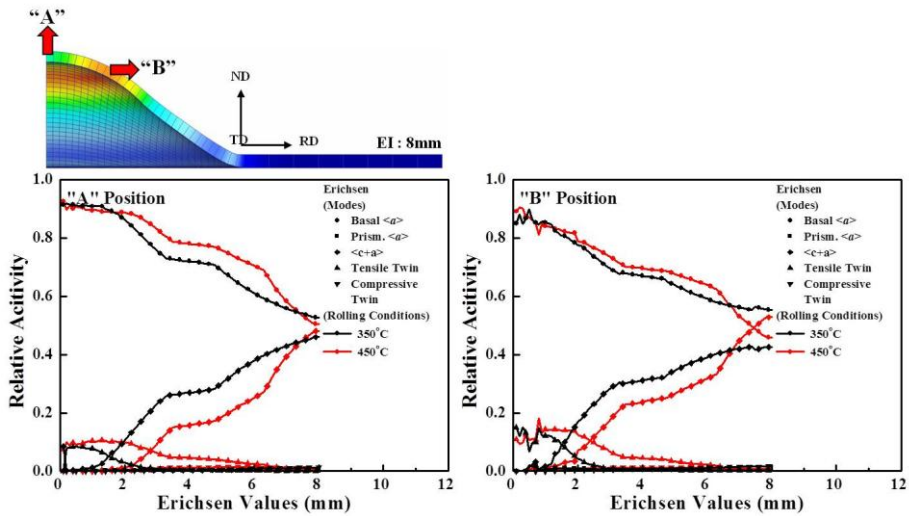


Figure 2.18 Contribution of the deformation modes during Erichsen test of AX60 alloy rolled at 350°C and 450°C.

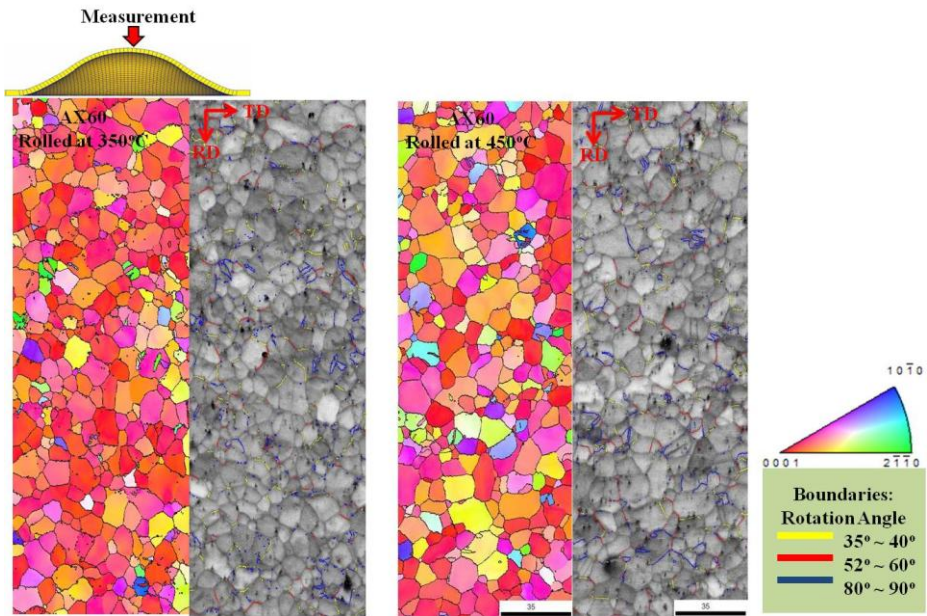


Figure 2.19 Inverse pole figure (IPF) map of AX60 alloy after Erichsen test of 3.4mm.

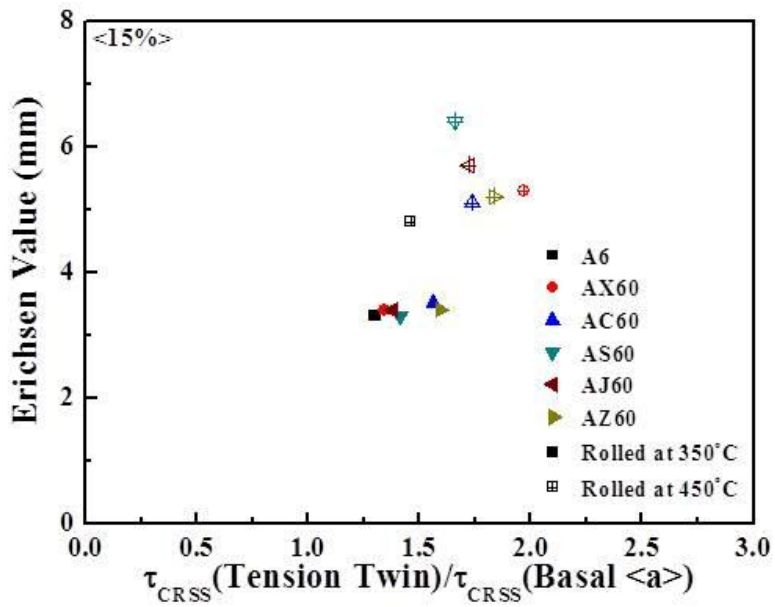


Figure 2.20 Relationship between Erichsen values and CRSS ratio (tension twin/basal $\langle a \rangle$ slip) at 15% corresponding to 3.4mm of Erichsen value at center position.

2.4 Conclusions

By using the TRC process, the effects of alloying elements on solidification and deformation behaviors of Mg-6Al-X alloys were investigated in this study. The main conclusions can be drawn as follows:

(1). According to TRC simulations, the AZ60 alloy showed a higher tendency to segregate while the AX60 and AJ60 alloys exhibited lower tendency due to the thermal and thermodynamic properties. This matched the centerline segregation observed in real microstructures.

(2). The formability of Mg-6Al-X alloys significantly increased with increasing rolling temperature, which may be related to modifying the deformation behaviors caused by texture evolution. Furthermore, the AX60 alloy exhibited a good combination of mechanical properties and formability, resulting from grain refinement and weaker basal texture.

(3). Among the different Mg-6Al-X alloys, the AX60 and AJ60 alloys had the lowest intensities of (0002) poles at both rolling conditions due to Ca and Sr alloying element addition, which had large atomic size mismatch to Mg.

(4). Contributions of basal $\langle a \rangle$ slip to accommodate the strain significantly increased the tensile and compression deformation as the rolling temperature increased from 350°C to 450°C. This results in improved yield isotropy and formability of Mg-6Al-X alloys.

(5). There was a close correlation between formability of Mg-6Al-X alloys and deformation mode activity in addition to correlation between yield isotropy and CRSS ratio (tension twin/basal $\langle a \rangle$ slip). Highly formable Mg alloys could be achieved by modifying deformation behaviors that result in yield isotropy enhancement.

Bibliography

1. K. S. Song, H. C. Jung, K. S. Shin, "Fatigue crack propagation behavior of AZ31 Mg alloy in ultra-high vacuum", *Met. Mater. Int.* 17 (2011) pp. 397-402.
2. C. D. Yim, Y. M. Moon, B. S. You, Y. S. Na, J. S. Bae, "Microstructural change in gravity cast Mg-Ni alloys with Ni contents", *Met. Mater. Int.* 10 (2004) pp. 605-608
3. M. Yuasa, M. Hayashi, M. Mabuchi, Y. Chino, "Improved plastic anisotropy of Mg-Zn-Ca alloys exhibiting high-stretch formability: A first-principles study", *Acta Mater.* 65 (2014) pp. 207-214.
4. D. Liang, C. B. Cowley, "The twin-roll strip casting of magnesium", *JOM*, 56, (2004) pp. 26-28.
5. J. H. Bae, M. S. Shim, B. C. Suh, D. W. Kim, S. H. Park, N. J. Kim, "Segregation in twin-roll cast Mg alloy and its suppression through alloy design", *Mater. Letters*, 13 (2014) 361-364.
6. M. Masoumi, F. Zarandi, M. Pekguleryuz, "Microstructure and texture studies on twin-roll cast AZ31 alloy and the effect of thermomechanical processing", *Mater. Sci. Eng. A* 528 (2011) pp. 1268-1279.
7. J. W. Bae, C. G. Kang, S. B. Kang, "Mathematical model for the twin roll type strip continuous casting of magnesium alloy considering thermal flow phenomena", *J. Mater. Process. Technol.* 191 (2007) pp. 251-255.
8. J. Zeng, R. Koitzsch, H. Pfeifer, B. Friedrich, "Numerical simulation of the twin-roll casting process of magnesium alloy strip", *J. Mater. Process. Technol.* 209 (2009) pp. 2321-2328.

9. J. J. Park, "Finite-element analysis of a vertical twin-roll casting", *Met, Mater, Int.*, 20 (2014) pp. 317-322.
10. S. Yi, J. Bohlen, F. Heinemann, D. Letzig, "Mechanical anisotropy and deep drawing behaviour of AZ31 and ZE10 magnesium alloy sheets", *Acta Mater.* 58 (2010) pp. 592-605.
11. X. Huang, K. Suzuki, N. Saito, "Textures and stretch formability of Mg-6Al-1Zn magnesium alloy sheets rolled at high temperatures up to 793K", *Scripta Mater.* 60 (2009) pp. 651-654.
12. K. Suzuki, Y. Chino, X. Huang, M. Yuasa, M. Mabuchi, "Enhancement of room temperature stretch formability of Mg-1.5mass%Mn alloy by texture control", *Mater. Trans.* 54 (2013) pp. 392-398.
13. N. Stanford, D. Atwell, A. Beer, C. Davies, M. R. Barnett, "The origin of rare earth texture development in extruded Mg-based alloys and its effect on tensile ductility", *Scripta Mater.* 59 (2008) pp. 772-775.
14. G. T. Bae, J. H. Bae, D. H. Kang, H. Lee, N. J. Kim, "Effect of Ca addition on microstructure of twin-roll cast AZ31 Mg alloy", *Met, Mater, Int.*, 15 (2009) pp. 1-5.
15. M. Yuasa, N. Miyazawa, M. Hayashi, M. Mabuchi, Y. Chino, "Effects of group II elements on the cold stretch formability of Mg-Zn alloys", *Acta Mater.* 83 (2015) pp. 294-303.
16. A. Sadeghi, M. Hoseini, M. Pekguleryuz, "Effect of Sr addition on texture evolution of Mg-3Al-1Zn alloy during extrusion", *MSE A* 528 (2011) pp. 3096-3104.
17. S. A. Lockyer, M. Yun, J. D. Hunt, D. V. Edmonds, "Micro- and macrodefects in thin sheet twin-roll cast aluminum alloys", *Mater. Characterization* 37 (1996) pp. 301-310.

18. M. Ferry, *Direct Strip Casting of Metals and Alloys*, Woodhead Publishing, Cambridge England, 2006.
19. X. Huang, Y. Chino, M. Mabuchi, M. Matsuda, "Influences of grain size on mechanical properties and cold formability of Mg-3Al-1Zn alloy sheets with similar weak initial textures", *MSE A* 61 (2014) pp. 152-161.
20. H. Borkar, M. Pekguleryuz, "Effect of extrusion parameters on texture and microstructure evolution of extruded Mg-1pct Mn and Mg-1pct Mn-Sr Alloys", *Metall. Mater. Trans. A* 46A (2015) pp. 488-495.
21. Z. R. Zeng, M. Z. Bian, S. W. Xu, C. H. J. Davies, N. Birbillis, J. F. Nie, "Texture evolution during cold rolling of dilute Mg alloys", *Scripta Mater.* 108 (2015) pp. 6-10.
22. L. Jiang, J. J. Jonas, A. A. Luo, A. K. Sachdev, S. Godet, "Influence of {10-12} extension twinning on the flow behavior of AZ31 Mg alloy", *MSE A* 445-446 (2007) pp. 302-309.
23. D. H. Kang, D. W. Kim, S. Kim, G. T. Bae, K. H. Kim, N. J. Kim, "Relationship between stretch formability and work-hardening capacity of twin-roll cast Mg alloys at room temperature", *Scripta Mater.* 61 (2009) pp. 768-771.
24. M. R. Barnett, Z. Keshavarz, A. G. Beer, D. Atwell, "Influence of grain size on the compressive deformation of wrought Mg-3Al-1Zn", *Acta Mater.* 52 (2004) pp. 5093-5103.
25. B. C. Suh, M. S. Shim, D. W. Kim, N. J. Kim, "Twinning behavior of Mg-4Zn-1Gd alloy sheet during longitudinal tensile deformation", *Scripta Mater.* 69 (2013) pp.465-468.

26. A. Chapuis, J. H. Driver, "Temperature dependency of slip and twinning in plane strain compressed magnesium single crystals", *Acta Mater.* 59 (2011) pp. 1986-1994.
27. S. B. Yi, C. H. J. Davies, H. G. Brokmeier, R. E. Bolmaro, K. U. Kainer, J. Homeyer, "Deformation and texture evolution in AZ31 magnesium alloy during uniaxial loading", *Acta Mater.* 59 (2006) pp. 549-562.

Chapter 3. Effects of alloying elements on deformation behaviors of Mg alloys

3.1 Introduction

Magnesium alloys have been paid attentions to apply automotive components due to its high specific strength and stiffness for weight reduction in automotive vehicles [1-2]. Most of Mg components in automobile industry have been fabricated by casting process such as high pressure die-casting and permanent mold casting, etc [3]. However, cast Mg alloys that generally show their low mechanical properties due to grain size and casting defects limit the Mg applications which require high mechanical properties and ductility. There have been lots of researches on Mg wrought alloys with high performance by wrought process such as rolling, extrusion, forging, etc [4-5]. However, application of these processes to Mg alloys could increase the production cost compared to casting processes and production rate is not enough to meet the demands of automobile industry. Recently, it has been reported that twin roll casting (TRC) process could fabricate Mg alloy sheets with low cost and high production rate [6-7]. Several TRC Mg alloy sheets have been successfully fabricated due to high mechanical properties. For example, TRC AZ31 and AZ41 alloys exhibit the high yield strength of 190 ~ 220MPa with elongation of 11.0 ~ 20.8% [8-9]. However, those TRC Mg alloys have the strong basal texture resulting in worse yield isotropy (compressive yield strength/tensile yield strength) and that is related to poor ductility and formability. Therefore, development of new TRC Mg alloys with random texture and enhanced yield isotropy should be necessary to extend the applications of wrought Mg alloys. Addition of

alloying elements on Mg alloys is one of the effective methods to weaken the strong basal texture. Especially, RE elements such as Ce, Y, Nd are well known to randomize the basal texture by particle-stimulated nucleation of recrystallization and significantly improve the yield isotropy [10-12]. Yield isotropy of Mg-Mn-RE alloys with weaker basal texture shows over the 0.8 compared to that of Mg-Mn alloy that has the yield isotropy of 0.3 and extruded Mg-Zn-Y alloys has exhibited excellent yield isotropy of over the 0.9 [12, 13]. Unfortunately, these kinds of Mg alloys containing RE alloying have difficulty to become commercial due to addition of expensive alloying elements. To expand application of wrought Mg alloys, new RE free Mg alloys or low contents RE Mg alloys with improved yield isotropy and more random texture are more potential. Among the various alloying elements, Al addition on Mg alloys has lots of advantages; 1) low cost 2) improvement of castability 3) increase of strength, etc [14-15]. It has been also reported that Al addition on Mg alloys could weak the strong basal texture and improve the yield isotropy [16-17]. For examples, Mg- x Al-1Mn alloys show improved yield isotropy of over 0.8 [17]. Similar values of yield isotropy have been reported for Mg-Al-Zn [18] and Mg-Al-Ca-Mn alloy [19]. However, there are few studies available for effects of alloying elements on yield isotropy of Mg-Al alloys. Furthermore, effects of alloying elements such as Mn, Ca, Si, Sr and Zn on correlation between yield isotropy and deformation behavior of Mg-6Al alloy have not yet been carried out.

In the present study, the influence of effects of alloying elements on yield isotropy and deformation behavior of Mg-Al alloys to develop new TRC Mg alloys was investigated. TRC Mg- x Al and Mg-6Al-X alloys were produced with different compositions. The mechanical properties of the alloys were examined tensile and compressive tests for evaluation of yield

isotropy. Microstructure and texture evolutions of TRC Mg- x Al and Mg-6Al- X alloys were examined by optical microscopy and analysis of X-ray diffraction, respectively. In order to analyze the correlation between yield isotropy and deformation behavior, VPSC simulations were carried out to calculate contribution of deformation modes to tension and compression deformation based on these experimental results.

3.2 Experimental Procedures

Twin roll cast Mg alloys with nominal compositions (in wt.%) Mg-6Al- x Mn ($x= 0.5, 0.7$ and 1.0), Mg-6Al- x Ca-0.3Mn ($x= 0.3, 0.5, 0.7$ and 1.0), Mg-6Al- x Sn-0.3Mn ($x= 1, 3, 5$ and 7), Mg-6Al- x Sr-0.3Mn ($x= 0.3, 0.5, 0.7$ and 1.0) and Mg-6Al- x Zn-0.3Mn ($x= 0.3, 1.0, 2.0$ and 4.0) were cast by TRC process. The TRC Mg alloys were melted at $700\sim 710^{\circ}\text{C}$ under the protection gas and flowed to the nozzle held at 650°C followed by twin roll casting to fabricate TRC Mg alloys. The roll gap was set to 2.0mm and roll speed was 3m/min . Sound TRC Mg alloys sheets were fabricated with plate thickness of around 3.3mm . For the hot rolling, TRC Mg sheets were homogenized at 400°C for 12hr , followed by water quenching. The homogenized Mg alloys were hot rolled at 350°C for 4pass with total rolling reduction of 65% . Before hot rolling, the sheets were preheated 350°C for 30min with follow by subsequent annealing process at 300°C for 1hr . In order to evaluate the mechanical properties, the tensile tests and compression tests were performed with a strain rate of $2 \times 10^{-4}/\text{sec}$ according the ASTM standard B557M with Instron 5582. The loading axis was parallel to the rolling direction. In order to evaluate the strength formability for Mg alloys, Erichsen cupping tests were carried out using graphite type lubricant. During the tests, punch diameter and speed were 20mm and 5mm/min . respectively. Pole figures of annealed M alloy sheets were measured at the mid-thickness planes perpendicular to the normal direction from four different planes, $\{10-10\}$, $\{0002\}$, $\{10-11\}$ and $\{11-10\}$ using Schulz reflection method by X-ray diffractometer with Cu K source. Using these experimental results, VPSC simulations were conducted for both tensile and compressive deformation in order to predict the contribution of various deformation modes such as basal

$\langle a \rangle$ slip, prismatic $\langle a \rangle$ slip, pyramidal $\langle c+a \rangle$ slip, tension twin and compression twin by using Voce-type hardening rule and Predominant Twin Reorientation Scheme (PTR) model for hardening and twinning model respectively.

3.3 Results and discussions

3.3.1 Effects of Al

Fig.3.1 shows the optical micrographs of the A1, A3, A6 and A9 alloys annealed at 350°C for 1hr. All the alloys show the fully recrystallized microstructure with no twin observation caused by static recrystallization. Among the four different alloys, A1 alloy shows the coarse microstructure with average grain size of 18.9 μm , while A9 alloy shows uniform microstructure with grain size of 10.7 μm . The grain size of Mg- x Al alloys steadily decreases from to by addition of Al content from 1wt.% to 9wt.%. Grain refinement could be attributed to second phases which can impede the grain boundary movement and help resist grain growth during annealing process. It is also observed that volume fraction of second phases significantly increases over the 6wt.% Al content and second phases of Mg- x Al alloys may consist of $\text{Mg}_{17}\text{Al}_{12}$, Al_8Mn_5 and $\text{Al}_{11}\text{Mn}_4$ predicted by PanDat7.0 software. It has been reported that Al_8Mn_5 phase generally appears in AM series alloys and $\text{Mg}_{17}\text{Al}_{12}$ phase forms in Mg-Al-Zn alloy during solidification [16, 20].

Fig. 3.2 indicates (0002) pole figures of annealed A1, A3, A6 and A9 alloys. All the alloys have the strong basal texture which is parallel to normal direction. This kind of texture can easily be observed in typical Mg alloys. It is interesting to note that (0002) pole figures of A6 and A9 alloys are tilted to transverse direction compared to A1 and A3 alloys, which are favorable with room temperature formability. Intensity of Basal texture is 12.075, 8.496, 7.796 and 8.728 for A1, A3, A6 and A9 alloys, respectively. When Al contents increase in Mg- x Al alloys, intensity of basal texture steadily decreases. A6 alloy shows the lower intensity of basal texture

compared to A9 alloy, however, entire basal texture of A9 alloy have weaker basal texture. Formation of weaker basal texture with high Al contents could be caused by decrease in solidus line by Al addition, which can relatively increase the rolling temperature compared to Mg alloys containing lower Al contents. Solidus temperature is 632.9 and 492.1°C for A1 and A9 alloys, respectively, and difference between A1 and A9 alloys is 140.8°C. Therefore, A9 alloy is rolled at relatively higher temperature compared to other alloys, which could affect the contribution of activity of deformation modes resulting in the different texture evolution during rolling process.

Table 3.1 shows a summary of tensile and compressive properties and Erichsen values of annealed Mg-xAl alloys. For tensile properties, yield strength of Mg-xAl alloys is 177.7, 169.8, 193.9 and 216.1MPa for A1, A3, A6 and A9 alloy, respectively. Ultimate strength of Mg- xAl alloys steadily increases from 232.3 to 342.7MPa, however, elongation decreases from 20.8 to 10.7% by addition of Al contents from 1wt.% to 9wt.%. Increase in YS and UTS could be associated with solid solution strengthening and grain refinement effects by Al addition with different contents as shown in Fig. 3.1. It can be also seen that compressive yield strength significantly increases by 72.4MPa by addition Al contents. It is mainly due to the grain refinement and texture evolution affecting the increase of compressive yield strength. Generally, tension twin is a main deformation mode under the compressive deformation, and it is largely affected by grain size and basal texture. Mg alloys with coarse microstructure and strong basal texture are easily deformed by tension twin under compressive deformation caused by favorable orientation for initiation of twin deformation [21]. Therefore, A1 alloy shows the lowest compressive yield strength with coarse grain size, while A9 alloy shows the highest compressive yield strength with weaker

basal texture, which is affecting the yield isotropy of Mg-xAl alloys. The yield isotropy (CYS/TYS) is steadily improved by increasing Al contents due to significant increase in compressive yield strength. Improvement of yield isotropy is favorable for sheet forming which is generally under the biaxial tension and uniaxial compression state. It shows that Erichsen values of Mg-xAl alloys are 2.0, 2.4, 2.8 and 2.6mm for A1, A3, A6 and A9 alloys, respectively. Formability at room temperature steadily increases by addition of Al contents and A6 alloy has the largest Erichsen values of 2.8mm. Formability and mechanical properties of Mg alloys can be improved by Al addition due to texture evolution and better yield isotropy affecting the contribution of activity of slip system and deformation twins during the deformation.

In order to predict the contribution of deformation modes by Al addition, VPSC simulations of Mg-xAl alloys are carried out at both tensile and compressive deformation. Fig. 3.3 (a) shows both simulated and experimental tensile and compressive strain stress curves in good agreement with each other. Fig. 3.3 (b) shows the hardening curves of various deformation modes with accumulated shear strains. Initial CRSS of basal $\langle a \rangle$ slip has the smallest value among deformation modes, which are easily observed at Mg single crystal [22]. It can be also seen that initial CRSS of basal $\langle a \rangle$ slip, prismatic $\langle a \rangle$ slip, pyramidal $\langle c+a \rangle$ slip, tension twin and compression twin increases with increasing Al contents. It has been reported that initial CRSS of prismatic $\langle a \rangle$ slip decreases by Al addition on Mg single crystal and Mg-1wt%Mn alloys that show a decrease in yield strength by Al addition. However, in the present study, we could not observe the decrease in yield strength at both tensile and compressive deformation by addition of Al contents. Significant increase in yield strength is observed by

solution hardening and grain refinement strengthening by increasing Al contents, which are associated with strengthening the initial CRSS of various deformation modes. Fig. 3.3 (c-d) indicates the relative activity of deformation modes for tensile and compressive deformation, respectively. In case of tensile deformation, basal $\langle a \rangle$ slip and prismatic $\langle a \rangle$ slip are the main deformation modes, and relative activity of basal $\langle a \rangle$ slip gradually increases with increasing Al contents. In terms of compressive deformation, tension twin and basal $\langle a \rangle$ slip are the dominant deformation modes, however, the relative activity of tension twin significantly decreases by Al addition. It is caused by increase in initial CRSS of tension twin with increasing Al contents and texture evolution which are not favorable for initiation of tension twin.

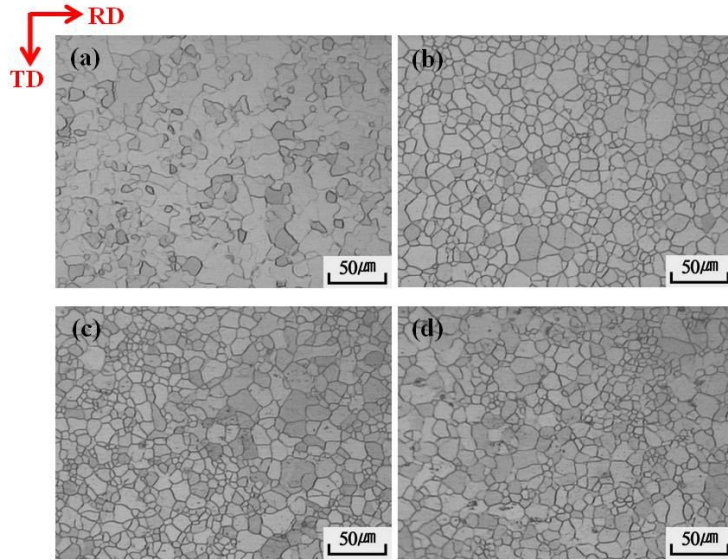


Figure 3.1 Microstructure of annealed Mg- x Al alloys; (a) A1, (b) A3, (c) A6 and (d) A9 alloy.

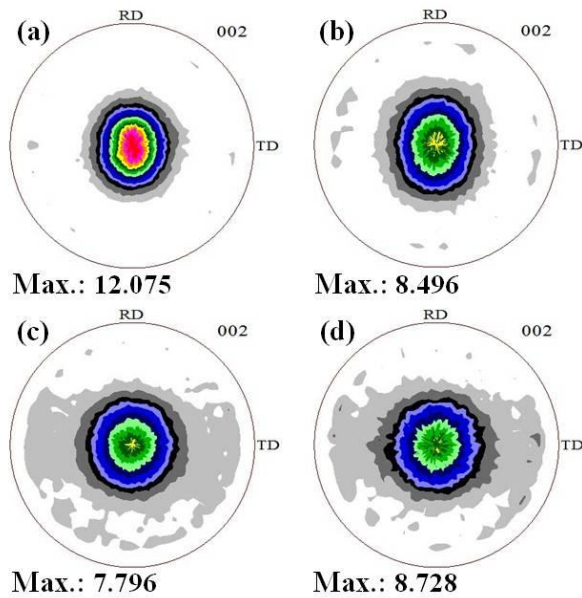


Figure 3.2 (0002) pole figures of annealed Mg- x Al alloys; (a) A1, (b) A3, (c) A6 and (d) A9 alloy.

Table 3.1 Mechanical properties and formability of Mg-xAl alloys.

Tensile Tests					Compression Tests				Erichsen Tests
Alloys	Y.S. (MPa)	U.T.S. (MPa)	Elong. (%)	n	Y.S. (MPa)	Max. Stress (MPa)	Elong. (%)	Y.S. _C / Y.S. _T	Formability (mm)
A1	177.7	232.3	20.8	0.140	88.0	382.5	10.3	0.50	2.0
A3	169.8	258.0	20.8	0.199	94.3	388.8	8.6	0.56	2.4
A6	193.9	302.0	17.3	0.207	123.3	415.9	12.0	0.64	2.8
A9	216.1	342.7	10.7	0.202	160.4	486.5	9.1	0.74	2.6

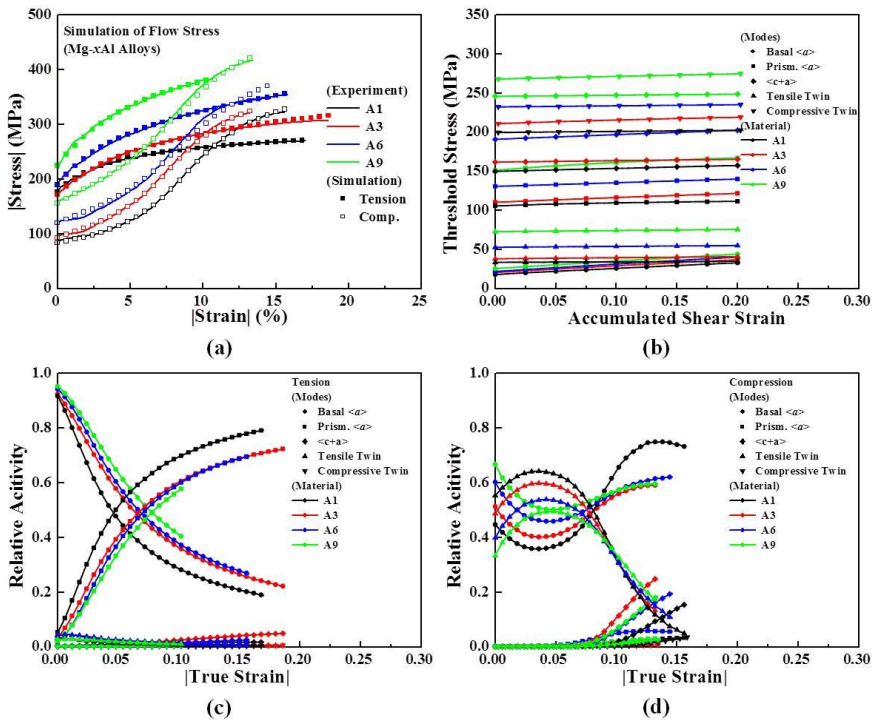


Figure 3.3 VPSC simulation results of annealed Mg-xAl alloys; (a) experimental and simulated stress-strain curves, (b) hardening curves of deformation modes, (c) relative activities during tensile deformation and (d) relative activities during compressive deformation.

3.3.2 Effects of Mn

Fig. 3.4 shows the optical microstructure of annealed Mg-6Al-xMn alloys rolled at 350°C. All the alloys exhibit equiaxed grains and fully recrystallized microstructures with no evidence of deformation twins caused by static recrystallization. It is also observed that the average grain size steadily reduces with increasing Mn contents. The grain size is 12.4, 9.1, 6.9 and 6.8 μm for AM603, AM605, AM607 and AM61 alloys, respectively, suggesting that the addition of Mn effectively plays a role in grain refiner. Khan S. A. *et. al* have been reported that The grain size of extruded Mg alloys decreases with increasing Mn contents due to intermetallic particles precipitated [23]. Similarly, fined microstructures have been also obtained by the addition of Mn to extruded ZX51 alloy due to second particles related to Mn [24]. Mg-6Al-xMn alloys could contain lots of second phases precipitated during the TRC casting. The volume fraction of α -Mg is 94.35 and 94.14% for AM603 and AM61 alloys, respectively, and volume fraction of second phase particles which are related to Al-Mn intermetallic compounds significantly increases with varying Mn contents. Therefore, the thermodynamic calculations could suggest that the Al_8Mn_5 phase which initially precipitates before α -Mg matrix provide the nucleation sites and hinder the grain growth during deformation or heat-treatment.

Fig. 3.5 shows the (0002) pole figures of annealed Mg-6Al-xMn alloys rolled at 350°C. Mg-6Al-xMn alloys exhibit strong basal texture which is parallel to normal direction with single peak. In addition, intensities of basal poles are 7.796, 7.772, 8.017 and 7.036 for AM603, AM605, AM607 and AM61 alloys, respectively, indicating that AM61 alloy has the largest intensity of 7.036 in (0002) pole figures. However, the addition of

Mn on Mg-6Al alloy has minor effect on texture evolution compared to other alloying elements such as Ca, RE, Sr etc. which are well known as effective elements to randomize the basal texture. Huang X. *et al.* have reported that addition of Mn on AZ31 slightly increases the basal pole intensity up to 0.4wt.% Mn and decreases the intensity over the 0.4wt.% Mn in rolled and annealed conditions due to increase in *c/a* ratio by Mn addition [25]. Similar result has been reported that ZX510 alloy has stronger basal texture than that of ZX51 alloy caused by PSN effects leading to decrease in volume fraction of unDRXed grains [24]. Mn addition slightly strengthen the intensity of (0002) poles figures, but effects of Mn addition on texture evolution of Mg-6Al alloys are limited in the present study.

Table 3.2 exhibits a summary of mechanical properties and formability of Mg-6Al-*x*Mn alloys. For tensile properties, yield strength of annealed Mg-6Al-*x*Mn alloys gradually increases with increasing Mn contents. The YS of AM603 alloy is 193.9MPa and YS of AM61 alloy is 204.1MPa increase by around 10MPa compared to AM603 alloy caused by grain refinement by addition of Mn alloying element as shown in Fig 3.4. Generally, Ultimate strength steadily increases with varying Mn contents except for AM61 alloy which have the same value of UTS to AM603 alloy. In addition, all the alloys have the elongation of around 18% with slight decrease in AM61 alloy. For compression properties, compressive yield strength is improved from 123.3 to 141.9MPa by the addition of 1.0wt.% of Mn to Mg-6Al alloy affecting the yield isotropy. Yield isotropy is 0.64, 0.66, 0.68 and 0.70 for AM603, AM605, AM607 and AM61 alloys, respectively. It is obvious that the addition of Mn improves the yield isotropy, which is good for room temperature formability. Erichsen values of Mg-6Al-*x*Mn alloys are 2.8, 2.9, 2.8 and 2.7mm for AM603, AM605, AM607 and AM61 alloys,

respectively. Even though Mg-6Al- x Mn alloys have moderate formability, Mg alloys containing higher strength with normal formability can be obtained by addition of Mn alloying element which are associated with active deformation modes during deformation.

It can be seen in this study that the addition of Mn on Mg-6Al alloy show no texture evolution compared to other alloying elements such as Ca, Sr, Zn etc., however, enhanced yield isotropy with moderate formability could be obtained by Mn addition. In order to analyze the relationship between yield isotropy and formability, VPSC simulations are carried out at tensile and compressive deformations. Fig. 3.6 (a) indicates that simulated tensile and compressive strain stress curves are well matched with experimental strain stress curves. Fig. 3.6 (b) shows the predicted threshold stress of various deformation modes with accumulated shear strains. The initial CRSS for various deformation such as basal $\langle a \rangle$ slip, prismatic $\langle a \rangle$ slip, pyramidal $\langle c+a \rangle$ slip, tension twin and compression steadily increases by increasing Mn contents, which leads to enhance the tensile and compressive yield strength. The initial CRSS for basal $\langle a \rangle$ slip and tension twin have the relative smaller values compared to other deformation modes resulting in higher activity during deformation. Fig. 3.6 (c-d) indicates the relative activity of deformation modes for tensile and compressive deformation, respectively. In tensile deformation, all the alloys show that the relative activity of basal $\langle a \rangle$ slip gradually decreases and that of prismatic $\langle a \rangle$ slip steadily increases due to work hardening with strain. In addition, the relative activity of basal $\langle a \rangle$ slip slightly increases with increasing Mn contents but it is not clear to show the effects of Mn contents on contribution of deformation modes during tensile tests. It was expected that AM603 alloy shows more active basal $\langle a \rangle$ slip due to weaker basal texture, however,

AM603 alloy has the lowest activity for basal $\langle a \rangle$ slip in simulation results among different Mg-6Al-xMn alloys. It is mainly caused by minor effects on texture evolution and strengthening by addition of Mn contents. As mentioned above, there is no significant change in texture evolution and dramatic improvement in yield strengths, which result in change the main deformation modes caused by CRSS ratio between deformation modes. However, CRSS ratio between basal $\langle a \rangle$ slip to prismatic $\langle a \rangle$ slip in Mg-6Al-xMn alloys has similar values resulting in almost same deformation behavior during tension deformation. In compressive deformation, all the alloys show that basal $\langle a \rangle$ slip and tension twin are the predominant deformation modes. In addition, the relative activity of tension twin gradually decreases with increasing Mn contents, however, that of basal $\langle a \rangle$ steadily increases during compressive deformation caused by different initial CRSS ratio (tension twin/basal $\langle a \rangle$ slip). As shown in Fig. 3.6 (b), Mg-6Al-xMn alloys which contain higher Mn contents generally show higher initial CRSS ratio (tension twin/basal $\langle a \rangle$ slip) compared to lower Mn contents due to effects of grain refinement on activity of tension twin.

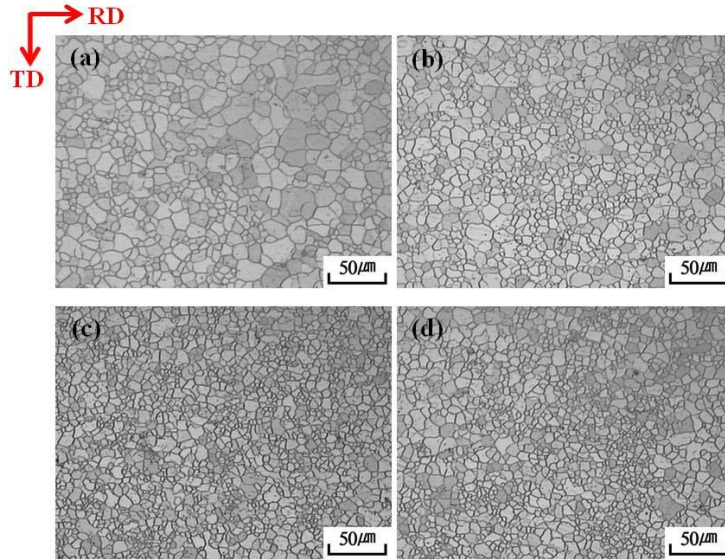


Figure 3.4 Microstructure of annealed Mg-6Al- x Mn alloys; (a) AM603, (b) AM605, (c) AM607 and (d) AM61 alloy.

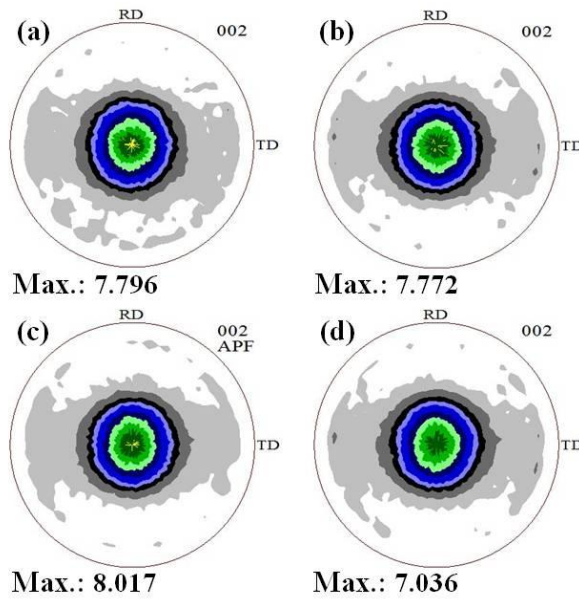


Figure 3.5 (0002) pole figures of annealed Mg-6Al- x Mn alloys; (a) AM603, (b) AM605, (c) AM607 and (d) AM61 alloy.

Table 3.2 Mechanical properties and formability of Mg-6Al-xMn alloys.

Tensile Tests					Compression Tests				Erichsen Tests
Alloys	Y.S. (MPa)	U.T.S. (MPa)	Elong. (%)	n	Y.S. (MPa)	Max. Stress (MPa)	Elong. (%)	Y.S. _c /Y.S. _T	Formability (mm)
AM603	193.9	302.0	17.3	0.207	123.3	415.9	12.0	0.64	2.8
AM605	197.5	304.4	19.2	0.204	129.8	444.8	11.7	0.66	2.4
AM607	203.2	308.4	18.6	0.200	137.9	455.9	10.4	0.68	2.8
AM61	204.1	302.0	15.3	0.190	141.9	469.1	11.8	0.70	2.6

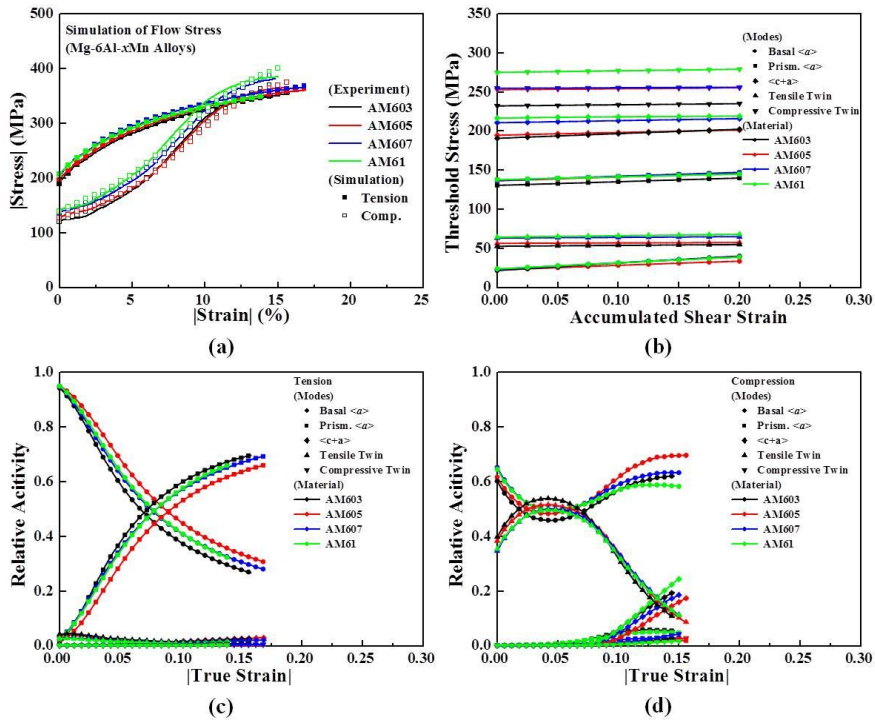


Figure 3.6 VPSC simulation results of annealed Mg-6Al-xMn alloys; (a) experimental and simulated stress-strain curves, (b) hardening curves of deformation modes, (c) relative activities during tensile deformation and (d) relative activities during compressive deformation.

3.3.3 Effects of Ca

Fig.3.7 shows the optical micrographs of annealed Mg-6Al-xCa alloys. Compared to A6 alloy, it can be proven that addition of Ca alloying element could play a role in grain refinement on Mg-6Al alloys. All the alloys show the uniform microstructure and grain size of Mg-6Al-xCa alloys gradually decreases by increasing Ca contents. Average grain size of Mg-6Al-xCa alloys is 7.2, 6.3, 5.5, and 5.2 μm , for AX603, AX605, AX607 and AX61 alloys. It is also interesting to note that second phases can be observed over the 0.7wt.% Ca addition. Maximum solid solubility of Ca in Mg-6Al-0.3Mn alloy is only 0.005wt.% predicted by PanDat software. Therefore, it can be explained that twin roll casting process could increase the solid solubility in Mg-6Al-xCa alloys caused by the high cooling rate. In addition, second phases of Mg-6Al-xCa alloys may have Al-Mn intermetallic compounds and (Mg, Al)₂Ca second phases which are thermally stable at 300~500°C. These kinds of second phases are well known to prevent the grain growth during hot rolling and heat-treatment.

Fig. 3.8 shows (0002) pole figures of annealed Mg-6Al-xCa alloys. In general, all the alloys show single peak pole figures showing strong basal texture. Intensity of (0002) pole figure is 7.155, 7.220, 6.778 and 6.458 for AX603, AX605, AX607 and AX61 alloys, respectively. As compared to A6 alloy, addition of Ca contents is an effective way to weaken the strong basal texture into random texture. With increasing Ca contents, the intensity of (0002) pole figure in Mg-6Al-xCa alloys steadily decreases. The same phenomenon could be observed at Mg-xCa alloys with random texture by Ca addition [26]. Formation of weaker basal texture by Ca contents could be explained by c/a ratio, stacking fault energy, etc.

Table 3.3 shows a summary of mechanical properties and formability of Mg-6Al-xCa alloys. For tensile properties, there is a significant increase in strength by Ca addition. Yield strength is 203.7, 207.7, 212.2 and 216.2 for AX603, AX605, AX607 and AX61 alloys, respectively, indicating that Ca addition is an effective alloying element to increase the yield strength compared to other alloying elements. In addition, Ultimate strength of Mg-6Al-xCa alloys increases and elongation until fracture slightly decreases by increasing Ca contents. The increase of yield strength and ultimate strength may be attributed to fine microstructure and solid solution strengthening mechanism by Ca addition. From the microstructure, fine and uniform microstructure could be obtained by Ca addition and TRC processing can extend Ca solid solubility in Mg-6Al alloys due to rapid cooling rate. Generally, Mg alloys have lower compressive yield strength compared to tensile yield strength due to formation of strong basal texture caused by plastic deformation. However, annealed Mg-6Al-xCa alloys show improved yield isotropy (CYS/TYS) by increased compressive yield strength with Ca contents. CYS and yield isotropy of A6 are only 123.3MPa and 0.64, however, those of AX61 alloy are 159.1MPa and 0.78, respectively. Increase in yield isotropy could be explained by smaller grain size and weaker basal texture by Ca addition. Erichsen values of Mg-6Al-xCa alloys gradually decreases with increasing Ca contents. Formability of Mg alloy is 2.8 for AX603, 2.6 for AX605, 2.6 for AX607 and 2.5mm for AX61 alloys, respectively. Decrease in formability of Mg-6Al-xCa alloys could be related to increase in strength with Ca contents. It has been reported that there is a good relationship between yield strength and formability of Mg alloy [27]. Generally, Mg alloys with higher strength have poor formability at room temperature due to difference in for deformation. However, AX603 alloy

shows better strength and similar formability level to those of A6 alloy caused by grain refinement and texture evolution which can affect the modifying the activity of deformation modes during plastic deformation.

It can be observed in this study that addition of Ca on Mg-6Al alloy could significantly improve the mechanical properties and weak the strong basal texture affecting activity of deformation modes. In order to analyze the activity of deformation modes, VPSC simulations of Mg-6Al-xCa alloys are carried out. Fig. 3.9 (a) indicates that simulated tensile and compressive strain stress curves are well matched with experimental strain stress curves. Fig. 3.9 (b) shows the predicted threshold stress of various deformation modes with accumulated shear strains. It can be seen that degree of increase in initial CRSS of basal $\langle a \rangle$ slip is relatively smaller, however, degree of increase in initial CRSS of tension twin is relatively bigger with increasing Ca contents, which indicates that dominant deformation modes could be changed during plastic deformation. Therefore, it can be expected that Mg alloys containing higher Ca contents have less activity of tension twin and more activity of slip system for compressive deformation caused by different initial CRSS ratio (tension twin/basal $\langle a \rangle$ slip). Fig. 3.9 (c-d) indicates the relative activity of deformation modes for tensile and compressive deformation, respectively. For the tensile deformation, dominant deformation modes are basal $\langle a \rangle$ slip and prismatic $\langle a \rangle$ slip, however, pyramidal $\langle c+a \rangle$ slip and compression twin are rarely activated. In addition, relative activity of basal $\langle a \rangle$ slip steadily increases, however, that of prismatic $\langle a \rangle$ slip decreases with increasing Ca contents. It is mainly caused by weaker basal texture with higher Ca containing Mg alloys due to the increase of Schmid factor. For the compressive deformation, dominant deformation modes are tension twin and basal $\langle a \rangle$ slip. Initially, tension

twin are main deformation in four different Mg alloys, however, the relative activity of tension twin significantly decreases with increasing Ca contents. Decrease in activity of tension twin could be explained by increase in CRSS ratio (tension twin/basal $\langle a \rangle$ slip).

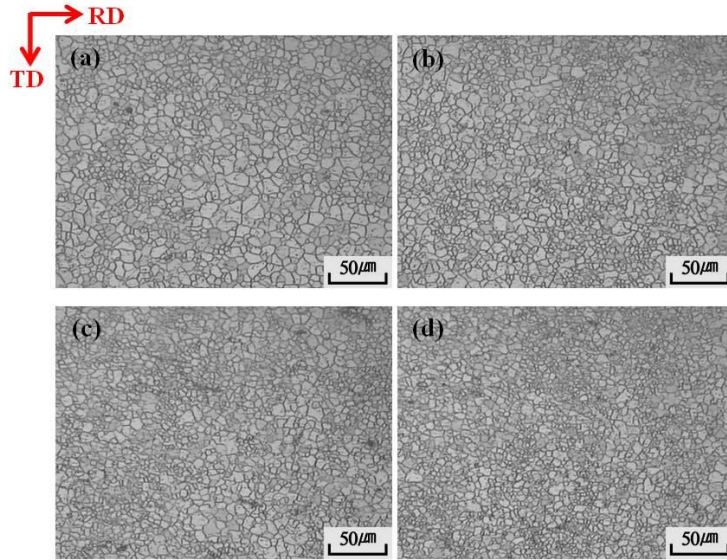


Figure 3.7 Microstructure of annealed Mg-6Al- x Ca alloys; a) AX603, (b) AX605, (c) AX607 and (d) AX61 alloy.

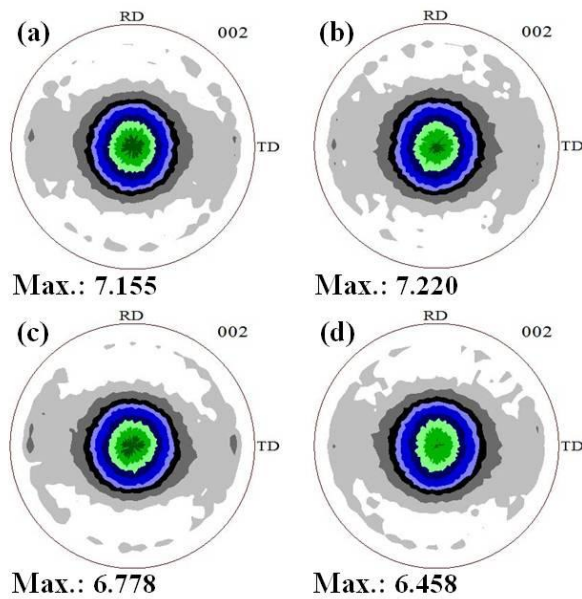


Figure 3.8 (0002) pole figures of annealed Mg-6Al- x Ca alloys; (a) AX603, (b) AX605, (c) AX607 and (d) AX61 alloy.

Table 3.3 Mechanical properties and formability of Mg-6Al-xCa alloys.

Tensile Tests					Compression Tests				Erichsen Tests
Alloys	Y.S. (MPa)	U.T.S. (MPa)	Elong. (%)	n	Y.S. (MPa)	Max. Stress (MPa)	Elong. (%)	Y.S. _C /Y.S. _T	Formability (mm)
A6	193.9	302.0	17.3	0.207	123.3	415.9	12.0	0.64	2.8
AX603	203.7	304.5	18.5	0.202	132.1	455.3	12.2	0.68	2.8
AX605	207.7	304.5	17.6	0.195	146.5	444.9	11.2	0.74	2.6
AX607	212.2	305.6	15.6	0.190	150.6	467.0	10.9	0.74	2.6
AX61	216.2	307.0	16.5	0.184	159.1	459.3	9.9	0.78	2.5

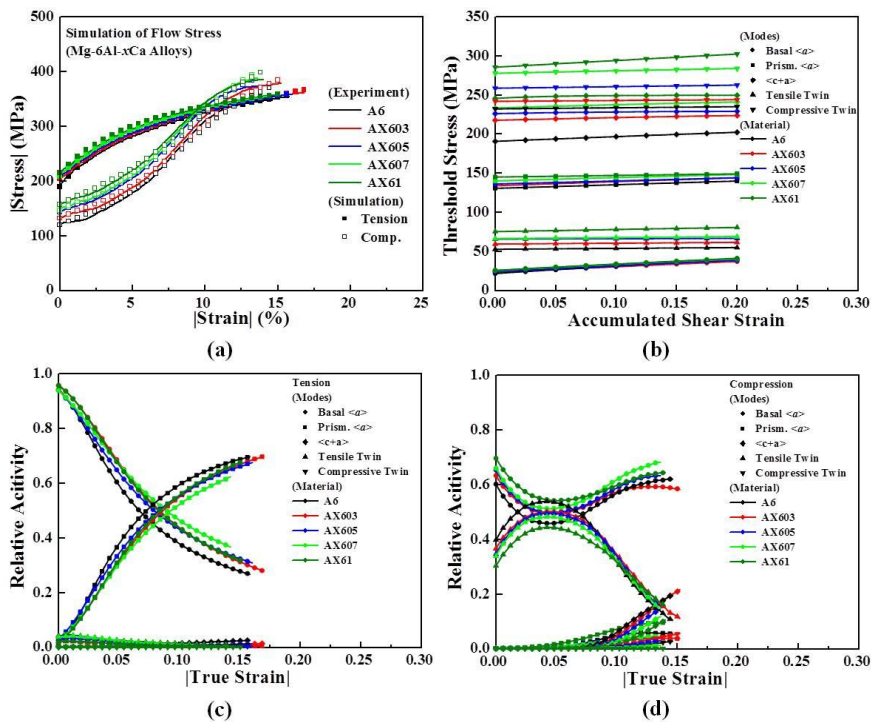


Figure 3.9 VPSC simulation results of annealed Mg-6Al-xCa alloys; (a) experimental and simulated stress-strain curves, (b) hardening curves of deformation modes, (c) relative activities during tensile deformation and (d) relative activities during compressive deformation.

3.3.4 Effects of Sn

Fig.3.10 exhibits the optimal micrographs of annealed Mg-6Al-xSn alloys. It can be seen that fined microstructure could be obtained by Sn addition to Mg-6Al alloys. All the alloys show uniform microstructures and no deformation twin by static recrystallization. Grain size of Mg-6Al-xSn alloys is 10.0, 8.2, 7.9 and 8.9 μm for AT61, AT63, AT65 and AT67 alloys, respectively. It is suggested that lower than 5wt.% Sn addition is effective to grain refinement, however, exceeding 5wt.% Sn addition has the limited grain refinement effects on Mg-6Al alloys. The same observation has been reported in Mg-Zn-Sn alloys by Wei *et. al* [28]. They have reported that addition of Sn slightly decreases the grain size of annealed alloys, however, effects on grain refinement are limited and not apparent. Limited effects of grain refinement by Sn addition are may be related to low value of growth restriction factor (GRF). Lee Y *et. al* [29] has reported that GRF value of Sn is only 1.47, and GRF values of Zr, Ca and Al elements are 38.29, 11.94 and 4.32, respectively. Compared to other elements, Sn has the relatively lower GRF value suggesting Sn addition has minor effects on grain refinements. It can be also seen from the microstructures that second phase particles are little observed lower than 5wt.% Sn, however, volume fraction of second phases significantly increase over the 5wt.% Sn. Solubility of Sn on Mg-6Al alloy is 6.6wt.%, and mole fraction of α -Mg matrix in Mg-6Al-xSn alloys is a range of 0.94 ~ 0.91 with gradual decrease by Sn additions in Scheil condition. It was expected that lots of second phase are observed over the 3wt.% Sn due to formation of Mg₂Sn phase by thermodynamic calculation. However, real microstructures of Mg-6Al-xSn alloys exhibit few second phases caused by TRC casting. In addition, second phases may consist of

Mg₁₇Al₁₂, Mg₂Sn and Al-Mn intermetallic compounds predicted by PanDat Software. It has been reported that Mg₁₇Al₁₂ and Mg₂Sn phases which can strengthen the Mg alloys generally appear in Mg-Al-Sn alloys during solidification [30, 31].

Fig. 3.11 shows the (0002) pole figures of annealed Mg-6Al-xSn alloys. All the alloys exhibit the basal textures with single peak. As compared with (0002) pole figure of A6 alloy, there is not a significant change in intensity of (0002) pole figures. Intensity of (0002) poles for A6 is 7.796, and basal texture intensities are 7.807, 7.286, 7.306 and 8.531 for AT61, AT63, AT65 and AT67 alloys, respectively. This result indicates that Sn addition does not linearly increase or decrease the maximum intensity of basal texture, however, it shows slightly weaker basal texture with increasing Sn contents with consideration of entire (0002) pole figures. S. Wei *et. al* have studied that the Sn addition can increase the max. intensity of (0002) pole figure in Mg-4Zn alloy due to the increase of its axial ratio [28]. It has been also reported that addition of Sn can slightly sharpen the extrusion texture compared to Pure Mg [11]. Therefore, it might be thought that Sn addition on Mg-Al alloys has a limited effect on texture evolution to weaker basal texture.

Table 3.4 shows a summary of mechanical properties and formability of Mg-6Al-xSn alloys. From the tensile properties, yield strength of Mg-6Al-xSn alloys is 199.5, 203.1, 207.8 and 212.3MPa for AT61, AT63, AT65 and AT67 alloys, respectively, indicating that Increasing Sn contents result in increased yield strength. Ultimate strength of Mg-6Al-xSn alloys also increases with increasing Sn contents, however, elongation dramatically decreases over the 5wt.% Sn. The increase in YS and UTS by Sn additions may be caused by grain refinement with fined microstructure and second

phases particles formed at TRC casting. Qi F. *et al.* also have mentioned that strengthening in Mg-Zn-Mn-Sn wrought alloys is mainly determined by grain refinement strengthening and precipitation strengthening [32]. It is well accepted that grain refinement and precipitation strengthening are the main mechanism for strengthening of Mg alloys due to its higher Hall-Petch coefficient and Zener pinning effect. For compression properties, Sn addition is effective to increase the compressive yield strength (CYS) of Mg-6Al-xSn alloys. CYS of AT61 is 129.2MPa, however, CYS of AT67 alloy is 154.1MPa. The significant improvement in strengthening could be obtained by Sn addition resulting in enhancement of the yield isotropy of Mg-6Al-xSn alloys. As compared to A6 alloy, yield isotropy is increased from 0.64 to 0.73 by addition of 7wt.% Sn due to relatively increased compressive yield strength. Since the deformed twins are predominant deformation modes under compressive deformation, it is important to restrict the initiation of deformation twins. Compared to A6 alloy, AT67 alloy have fined microstructure and the similar shape of (0002) pole figure suggesting that AT67 alloy have more tendency to suppress the activity of deformed twins during compressive deformation. Formability of Mg-6Al-xSn alloys gradually decreases with increasing Sn contents. However, Comparable to A6 alloy, formability of AT61 alloy exhibits 3.0mm of Erichsen values with improved mechanical properties, which are associated with enhanced yield isotropy.

From the previous results, increasing Sn contents on Mg-6Al alloys, there are significant increases in compressive properties resulting in enhanced the yield isotropy of Mg-6Al-xSn alloys, whereas (0002) pole figures are not dramatically changed by Sn addition. In order to analyze the relationship yield isotropy and mechanical properties, VPSC simulations of

Mg-6Al-xSn alloys are carried out. Fig. 3.12 (a) indicates that simulated tensile and compressive strain stress curves are well matched with experimental strain stress curves. Fig. 3.12 (b) shows the predicted threshold stress of various deformation modes with accumulated shear strains. It can be seen that initial CRSS of basal $\langle a \rangle$ slip has the smallest values among the various deformation modes. Initial CRSS of deformation modes steadily increases by increasing Sn contents, however, degree of increase in initial CRSS values depends on deformation modes such as basal $\langle a \rangle$ slip, prismatic $\langle a \rangle$ slip, pyramidal $\langle c+a \rangle$ slip, tension twin and compression twin. Basal $\langle a \rangle$ slip has the smallest tendency of increase in initial CRSS while compression twin has relative largest degree of increase in initial CRSS compared to other deformation modes, suggesting that the active deformation modes can be modified due to different CRSS ratios by Sn additions. Fig. 3.12 (c-d) indicates the relative activity of deformation modes for tensile and compressive deformation, respectively. For tensile deformation, basal $\langle a \rangle$ and prismatic $\langle a \rangle$ slip are predominant deformation modes and tensile twin and pyramidal $\langle c+a \rangle$ slip are secondary deformation modes for initial and final stage, respectively. Generally, relative activity of basal $\langle a \rangle$ slip is getting larger with increasing Sn contents compared to A6 alloy, however, the tendency is not clear due to no change of basal texture by Sn addition. For compressive deformation, basal $\langle a \rangle$ slip and tension twin are main deformation modes due to low CRSS and favorable stress state for initiation of deformation twin. In addition, the relative activity of basal slip slightly increases, whereas that of tension twin decreases by increasing Sn contents. It is mainly caused by different CRSS ratio (tension twin/basal $\langle a \rangle$ slip) depending on different Sn contents. When higher Sn contents are added to Mg-6Al alloy, CRSS ratio (tension twin/basal $\langle a \rangle$ slip) is getting larger

resulting in limitation of activity in tension twin during compression deformation, which is associated with enhanced yield isotropy.

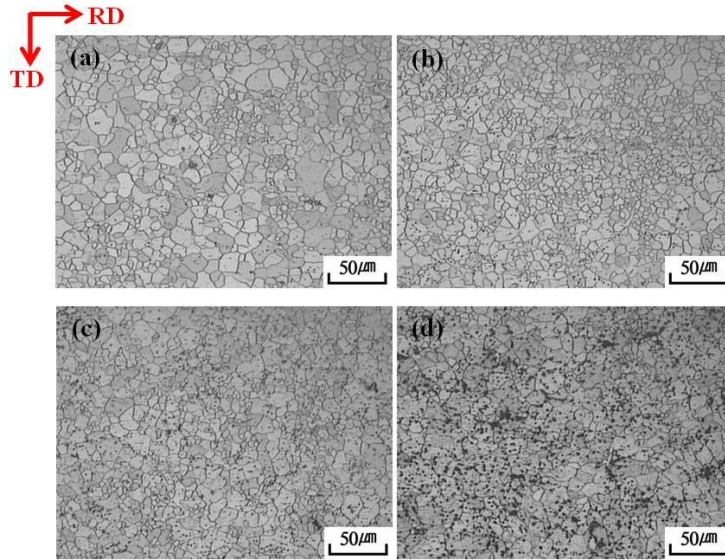


Figure 3.10 Microstructure of annealed Mg-6Al- x Sn alloys; (a) AT61, (b) AT63, (c) AT65 and (d) AT67 alloy.

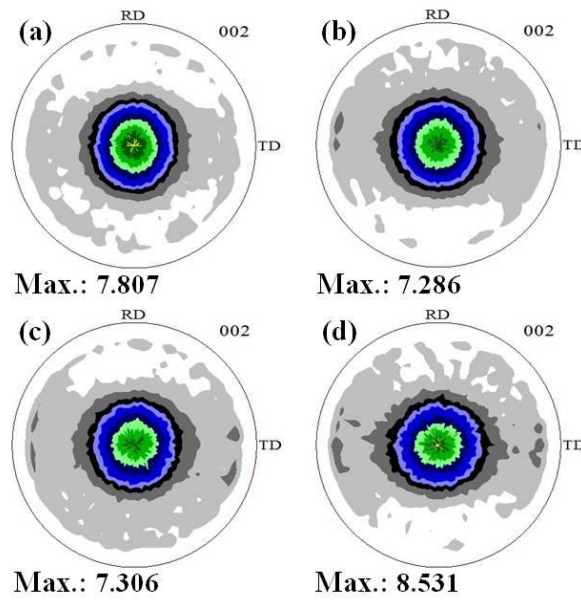


Figure 3.11 (0002) pole figures of annealed Mg-6Al- x Sn alloys; (a) AT61, (b) AT63, (c) AT65 and (d) AT67 alloy.

Table 3.4 Mechanical properties and formability of Mg-6Al-xSn alloys.

Tensile Tests					Compression Tests				Erichsen Tests
Alloys	Y.S. (MPa)	U.T.S. (MPa)	Elong. (%)	n	Y.S. (MPa)	Max. Stress (MPa)	Elong. (%)	Y.S. _C /Y.S. _T	Formability (mm)
A6	193.9	302.0	17.3	0.207	123.3	415.9	12.0	0.64	2.8
AT61	199.5	304.7	18.6	0.201	129.2	421.5	11.6	0.65	3.0
AT63	203.1	311.3	19.8	0.206	137.8	424.8	11.7	0.68	2.7
AT65	207.8	329.7	18.8	0.208	148.3	449.3	10.2	0.71	2.4
AT67	212.3	323.8	10.7	0.197	154.1	462.4	10.3	0.73	2.1

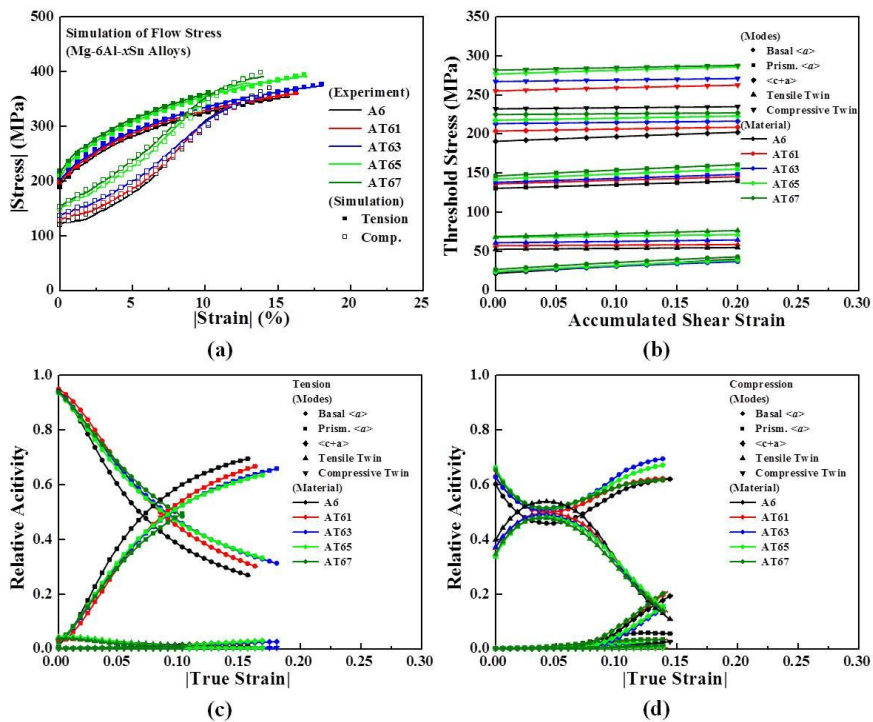


Figure 3.12 VPSC simulation results of annealed Mg-6Al-xSn alloys; (a) experimental and simulated stress-strain curves, (b) hardening curves of deformation modes, (c) relative activities during tensile deformation and (d) relative activities during compressive deformation.

3.3.5 Effects of Sr

Fig. 3.13 indicates the optical micrographs of annealed Mg-6Al-xSr alloys. From the microstructures, Mg-6Al-xSr alloys show fully recrystallized microstructure and uniform equiaxed grain microstructure with no deformation twin caused by static recrystallization. Compared to A6 alloy, it can be seen that addition of Sr alloying element on Mg-6Al alloy is effective to grain refinement. Average grain size of Mg-6Al-xSr alloys is 10.6, 7.5, 7.4, and 5.4 μm , for AJ603, AJ605, AJ607 and AJ61 alloys, respectively. It has been also reported that addition of Sr on Mg-Mn alloys reduced the grain size in the rolled and annealed condition [33]. In addition, the amount of second phases somehow increases by increasing Sr contents, but the degree are not severe. It can be explained by the TRC process. During the TRC casting, the molten alloys go through the chilled Cu-Be rolls, and are rapidly solidified with cooling rate of 100~1,000 $^{\circ}\text{C}/\text{s}$ which could extend the max. solid solubility [34]. Max. solid solubility of Sr in Mg-6Al alloys is only 0.014wt.%, and volume fraction of α -Mg matrix in Scheil condition is 94.4~94.9 % predicted by thermodynamic simulation. It was expected that lots of second phases will appear during casting in consideration of its thermal properties, however, real microstructures of Mg-6Al-xSr alloys show few second phase particles. Therefore, lots of Al and Sr alloying elements could be easily dissolved to Mg matrix by TRC process compared to conventional casting process. In addition, second phases of Mg-6Al-xSr alloys may mainly contain $\text{Mg}_{17}\text{Al}_{12}$ phases, and Al_4Sr and AlMgSr phases could be somehow formed during TRC casting.

Fig. 3.14 shows (0002) pole figures of annealed AJ603, AJ605, AJ607 and AJ61 alloys. In all alloys, basal poles are parallel to normal direction

with single peak pole figures. Formation of basal texture are mainly caused by activity of basal slip during hot-rolling process and further heat-treatment such as annealing process could not significantly change the strong basal texture due to the occurrence of the continuous static recrystallization [26, 35]. Intensity of (0002) pole figure for AJ603 alloy is 7.461 which are the highest texture intensity, however, AJ61 alloy shows the smallest (0002) pole figure intensity of 6.751 among the four different alloys. This result indicates that weaker basal texture forms with increase in Sr contents. It is well known that addition of Sr alloying element could play a role in formation of weaker basal texture in Mg alloys. Borkar *et. al* have reported that addition of Sr can accelerate particle-stimulated nucleation (PSN) of recrystallization resulting in randomization of basal texture in Mg-Mn alloys [36]. It is also reported that Sr element reduces the general stacking fault energy of prismatic plane resulting in activation of prismatic $\langle a \rangle$ slip related to formation of non-basal texture [37]. It is quite difficult to derive formation of random texture by addition of Sr element. Therefore, lots of factors such as PSN recrystallization, SFE, c/a ratio can complicatedly affect the texture evolution to form the random texture of Mg alloys.

Table 3.5 shows a summary of mechanical properties and formability of Mg-6Al-xSr alloys. From the mechanical properties, it can be said that addition of Sr element can increase the strength of Mg-6Al alloys under the tensile and compressive deformation. For tensile properties, yield strength of Mg-6Al-xSr alloys gradually increases with increasing Sr contents. YS of AJ603 alloy is 194.0MPa and that of AJ61 alloy is 217.0MPa, indicating that fined microstructure and second phases particle are attributed to increase its yield strengths. In addition, ultimate strength steadily increases with corresponding Sr contents. It is interesting to note that elongation does not

decrease by increasing Sr contents without AJ605 alloy. Generally, YS or UTS of Mg alloys increases, elongation decreases with corresponding to degree of increase in strength. However, Mg-6Al-xSr alloys shows increasing the strengths and similar values of elongation caused by uniform microstructure and dispersed second phase particles with small fractions. It is also found that compressive yield strength and ultimate strength of Mg-6Al-xSr alloys significantly increases by addition of Sr, which results in improving the yield isotropy (CYS/TYS) representing the one of the formable factors. Yield isotropy of A6 alloy is 0.64 and that of AJ603 alloy is 0.66 with slightly increase by Sr addition. Improved yield isotropy is favorable for formability of Mg alloys at room temperature due to stress state and accommodation of thickness strain during sheet forming. Formability of Mg-6Al-xSr alloys is 2.9, 2.7, 2.6 and 2.6mm for AJ603, AJ605, AJ607 and AJ61 alloys, respectively. Comparable to that of A6 alloy, AJ603 alloy exhibits more formable ability and excellent mechanical properties by addition of Sr and it may be related to uniform microstructure and weaker texture resulting in enhanced yield isotropy caused by modifying the active deformation modes.

The above results indicate that both mechanical properties and room temperature formability of Mg-6Al alloy could be enhanced by addition of Sr element, which can improve the yield isotropy. In order to analyze the contribution of deformation modes on tensile and compressive deformation, VPSC simulations of Mg-6Al-xSr alloys are carried out. Fig. 3.15 (a) shows the simulated and experimental strain stress curves on tensile and compressive deformations, which are in good agreement with each other. Fig. 3.15 (b) indicates the predicted threshold stress of basal $\langle a \rangle$ slip, prismatic $\langle a \rangle$ slip, pyramidal $\langle c+a \rangle$ slip, tension twin and compression twin with

accumulated shear strains. All the alloys show that basal $\langle a \rangle$ slip has the smallest initial CRSS and compression twin has the largest initial CRSS. When Sr contents increases, initial CRSS of all deformation modes steadily increases caused by solid solution strengthening and precipitated strengthening by addition of Al and Sr elements, which are related to increase in strength. Fig. 3.15 (c-d) shows the relative activity of deformation modes for tensile and compressive deformations with strains. For tensile deformation, basal $\langle a \rangle$ and prismatic $\langle a \rangle$ slip are predominant deformation modes, and tension twin is active at initial strain stage, which can relax the stress and increase the activity of slip system. However, pyramidal $\langle c+a \rangle$ slip accommodates small portion at final strain stage due to higher CRSS values. In addition, the relative activity of basal $\langle a \rangle$ slip are getting bigger, whereas that of prismatic $\langle a \rangle$ slip are getting smaller by increasing Sr contents due to more random texture and lower CRSS ratio (prismatic $\langle a \rangle$ slip/basal $\langle a \rangle$ slip) in Mg alloys containing higher Sr contents. In compressive deformation, all the alloys show that tension twin is the main deformation mode to accommodate the strain due to favorable states for initiation of twin deformation. The relative activity of basal slip steadily increases, whereas that of tension twin gradually decreases with increasing Sr content, which are associated with enhanced yield isotropy caused by increased compressive yield strength by restriction of active tension twin during compressive deformation.

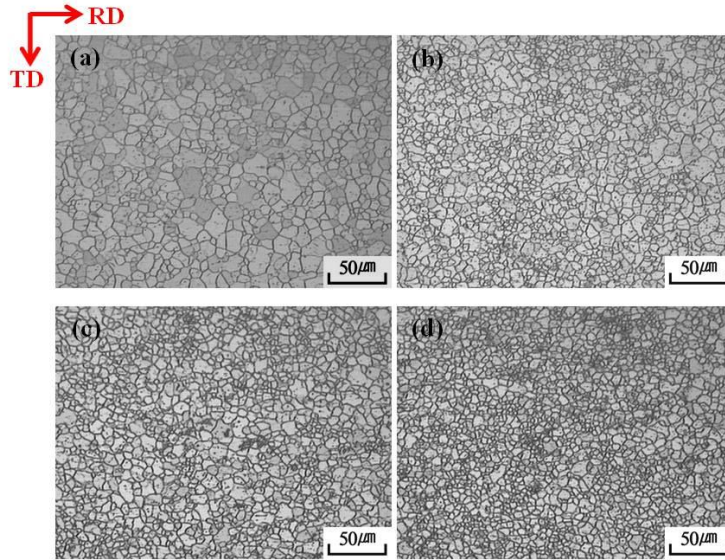


Figure 3.13 Microstructure of annealed Mg-6Al-xSr alloys; (a) AJ603, (b) AJ605, (c) AJ607 and (d) AJ61 alloy.

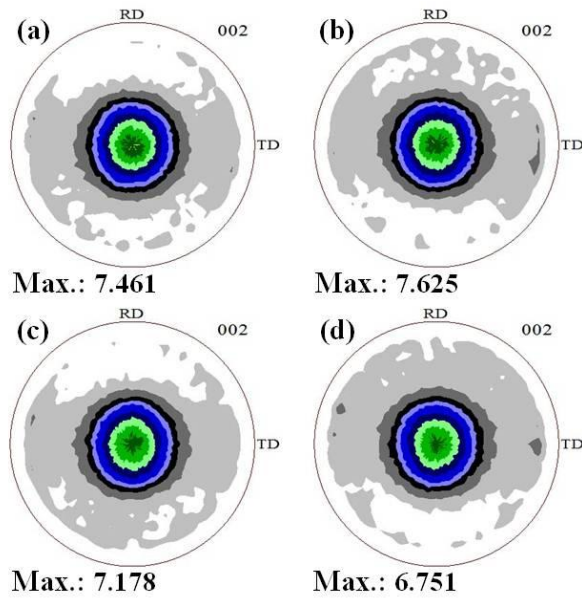


Figure 3.14 (0002) pole figures of annealed Mg-6Al-xSr alloys; (a) AJ603, (b) AJ605, (c) AJ607 and (d) AJ61 alloy.

Table 3.5 Mechanical properties and formability of Mg-6Al-xSr alloys.

Tensile Tests					Compression Tests				Erichsen Tests
Alloys	Y.S. (MPa)	U.T.S. (MPa)	Elong. (%)	n	Y.S. (MPa)	Max. Stress (MPa)	Elong. (%)	Y.S. _C /Y.S. _T	Formability (mm)
A6	193.9	302.0	17.3	0.207	123.3	415.9	12.0	0.64	2.8
AJ603	194.0	298.4	22.0	0.211	127.3	404.4	12.2	0.66	2.9
AJ605	207.0	302.2	14.3	0.196	135.6	441.6	12.0	0.66	2.7
AJ607	210.4	306.4	20.2	0.198	144.6	461.4	11.0	0.69	2.6
AJ61	217.0	314.3	20.8	0.194	144.9	467.8	11.6	0.67	2.6

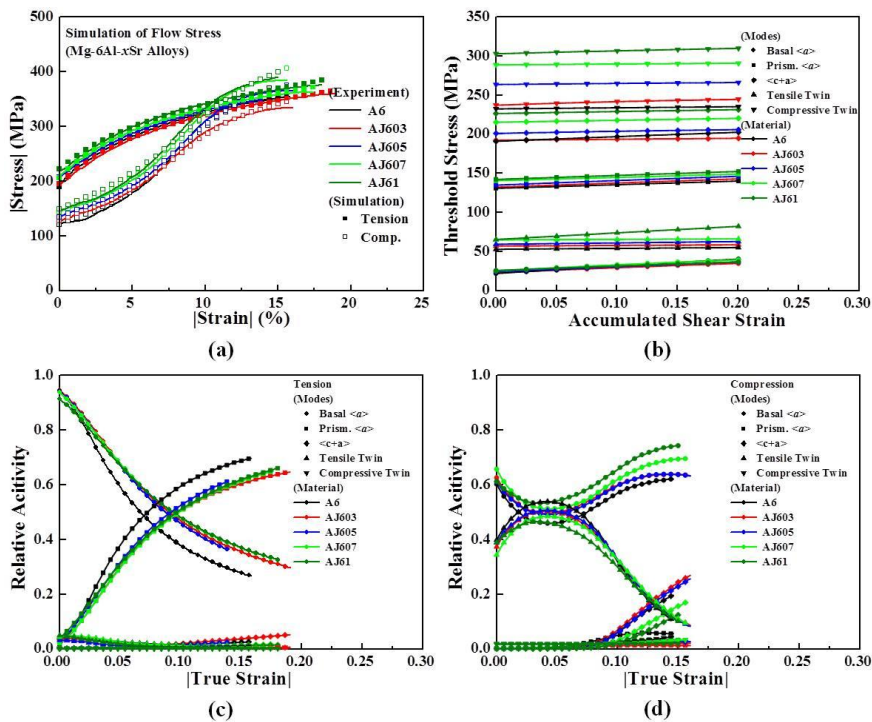


Figure 3.15 VPSC simulation results of annealed Mg-6Al-xSr alloys; (a) experimental and simulated stress-strain curves, (b) hardening curves of deformation modes, (c) relative activities during tensile deformation and (d) relative activities during compressive deformation.

3.3.6 Effects of Zn

Fig. 3.16 indicates the optical micrographs of annealed Mg-6Al-xZn alloys. All the alloys exhibit the uniform microstructure with fully recrystallized microstructure with no deformation twins. Compared to A6 alloy, Zn addition could effectively reduce the grain size of Mg-6Al-xZn alloys. The average grain size is 10.0, 9.0, 7.2, and 7.0 μm for AZ603, AZ61, AZ62 and AZ64 alloys, respectively, suggesting that refined microstructure can be obtained with increasing Zn contents in Mg-6Al alloy. Similar result has been reported that Zn addition reduces the grain sizes of extruded TZ5x alloys [38]. Decrease in grain size may be contributed to second phase particles which play a role in retarding grain growth during hot rolling and thermal treatment. From the microstructures, it can be also seen that volume fraction of second phase particles increase with increasing Zn contents. However, increase tendency in volume fraction is negligible and most of second phases are in Mg matrix due to high solubility of Zn in Mg. Max. solubility of Zn in Mg-6Al alloy is 4.9wt.% and mole fraction of α -Mg matrix in Mg-6Al-xZn alloys is a range of only 94.02 ~ 90.76% by increasing Zn contents under Scheil condition. In addition, second phase particles consists of $\text{Mg}_{17}\text{Al}_{12}$, MgAlZn and Al-Mn intermetallic compounds predicted by PanDat software.

Fig. 3.17 indicates (0003) pole figures of annealed Mg-6Al-xZn alloys. All the alloys exhibit single peak type texture which is parallel to normal direction. It can be found that increasing Zn contents can spread basal poles toward the transverse direction and intensities of basal poles are 7.529, 7.177, 7.636 and 5.328 for AZ603, AZ61, AZ62 and AZ64 alloys, respectively, indicating that generally Zn addition reduces the intensity of (0002) pole

figures of Mg-6Al- x Zn alloys. It has been reported that distribution of (0001) pole figures has a little change and their intensity become a little stronger with Zn increasing [38]. Similarly, Kim D. W *et. al* have mentioned that Zn content does not affect the texture evolution in Mg-Zn alloys [39]. Up to the addition of 2wt.% Zn, there is no change in texture evolution in Mg-6Al- x Zn alloys. On the other hand, over the 2wt.% Zn contents, intensity of basal texture significantly decreases indicating AZ64 alloy has the lowest value of basal texture intensity compared to A6 alloy which has the intensity of 7.796 in basal texture. Formation of weaker basal texture could be related to activation of non-basal slip system during hot-rolling. It has been investigated that Zn solutes the CRSS for prismatic slip steadily decreases with Zn contents for enhancing activity of prismatic $\langle a \rangle$ slip [40]. However, higher temperatures, CRSS for prismatic slip increases with varying Zn contents suggesting that CRSS of prismatic slip is not related to weaker basal texture at higher Zn contents. Recently, it has been reported that high temperature rolling could reduce the intensity of basal texture in Mg alloys [41, 42]. Non-basal slip system and deformation twins such as double twins could be activated at higher temperature leading to formation of random basal textures. Generally, it is known that addition of solute alloying elements can decrease the temperature of solidus line. Temperature of solidus line is 531.69 and 401.97°C for AZ60 and AZ64, respectively. Therefore, weaker basal texture of AZ64 alloy can be possibly be related to decrease in temperature of solidus line which increases the relative rolling temperature compared to lower Zn contents.

Table 3.6 shows a summary of mechanical properties and formability of Mg-6Al- x Zn alloys. For tensile properties, it can be found that the addition of Zn can be effective to improve the mechanical properties such as

yield strength and ultimate strength. YS of Mg-6Al-xZn alloys are 207.5, 211.5, 219.8 and 231.3MPa for AZ603, AZ61, AZ62 and AZ64 alloys, respectively. Linear increase can be observed at YS and UTS with increasing Zn content, suggesting that solid solution hardening and precipitate strengthening could be attributed to increase in its strengths. However, elongation to failure steadily decreases with varying Zn contents. For compression properties, there is a significant improvement of compressive yield strength with increasing Zn contents. CYS of Mg-6Al-xZn alloys is 88.0, 94.3, 123.3 and 160.4MPa for AZ603, AZ61, AZ62 and AZ64 alloys, respectively, indicating the addition of Zn can be effective to increase the yield isotropy. Among the Mg-6Al-xZn alloys, AZ64 alloy shows the largest value of 0.74 in yield isotropy due to weaker basal texture and fined microstructure which are not favorable for initiation of tension twin in compression deformation, suggesting that AZ64 alloy can be formable at room temperature. Erichsen values of Mg-6Al-xZn alloys are 3.0, 3.0, 3.2 and 3.0mm for AZ603, AZ61, AZ62 and AZ64 alloys, respectively. Comparable to that of A6 alloy, all the alloys exhibit more formable ability and increased strengths by addition of Zn, which is caused by refined microstructure and improved yield isotropy leading to modifying the active deformation modes.

In order to analysis the contribution of active deformation modes during the tensile and compressive deformation, VPSC simulations of Mg-6Al-xZn alloys are carried out. Fig. 3.18 (a) exhibits both simulated and experimental tensile and compressive strain-stress curves in good agreement. Fig. 3.18 (b) indicates the hardening curves of basal $\langle a \rangle$ slip, prismatic $\langle a \rangle$ slip, pyramidal $\langle c+a \rangle$ slip, tension twin and compression twin with accumulated shear strains. It can be seen that AZ64 alloy has the largest

initial CRSS values of various deformation modes compared to other alloys. As mentioned before, Zn addition reduces the CRSS for prismatic $\langle a \rangle$ slip by solid solution softening resulting in decrease of yield strength at single and polycrystalline samples [40, 43]. However, such a kind of softening the yield strength could not be found at small contents of Zn and only phenomenon of solid solution hardening on Mg-6Al-xZn alloys is observed with increasing yield strength with increasing Zn contents in present study. In addition, all the alloys show that initial CRSS for basal $\langle a \rangle$ slip has lowest values and initial CRSS for compression twin has the largest values among different deformation modes with general trend at Mg alloys. Fig. 3.18 (c-d) indicates the relative activity of deformation modes for tensile and compressive deformation, respectively. From the tensile deformation, the main deformation modes are basal $\langle a \rangle$ slip and prismatic $\langle a \rangle$ slip and relative activity of basal $\langle a \rangle$ slip steadily increases by varying Zn contents. Even though initial CRSS for basal $\langle a \rangle$ slip increases with increasing Zn contents, the degree of increase in CRSS for basal slip is smaller compared to other deformation modes and weaker basal texture at higher Zn contents are favorable for activation of basal slip with Schmid factor. From the compressive deformation, the dominant deformation modes are tension twin and basal $\langle a \rangle$ slip, however, the relative activity of tension twin steadily decreases by Zn addition. The relative activity of tension twin at initial stage is 0.411, 0.391, 0.388 and 0.329 for AZ603, AZ61, AZ62 and AZ64 alloys, respectively indicating that predominant deformations could be changed to slip deformations from twin deformations and it affects the yield isotropy of Mg-6Al-xZn alloys.

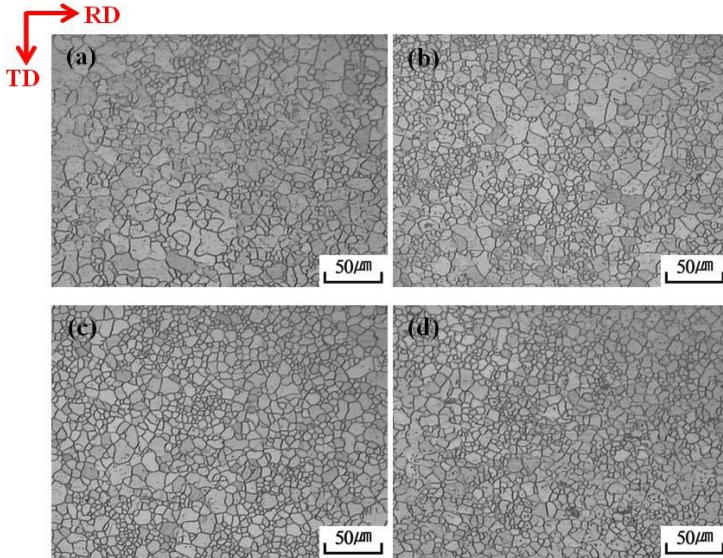


Figure 3.16 Microstructure of annealed Mg-6Al- x Zn alloys; (a) AZ603, (b) AZ61, (c) AZ62 and (d) AZ64 alloy.

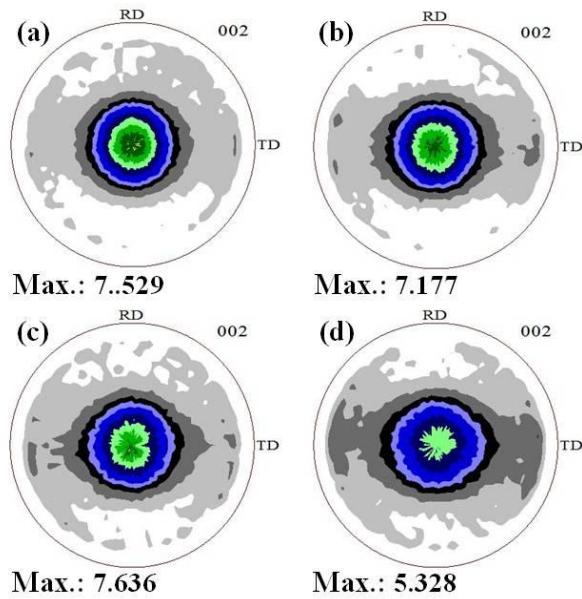


Figure 3.17 (0002) pole figures of annealed Mg-6Al- x Zn alloys; (a) AZ603, (b) AZ61, (c) AZ62 and (d) AZ64 alloy.

Table 3.6 Mechanical properties and formability of Mg-6Al-xZn alloys.

Tensile Tests					Compression Tests				Erichsen Tests
Alloys	Y.S. (MPa)	U.T.S. (MPa)	Elong. (%)	n	Y.S. (MPa)	Max. Stress (MPa)	Elong. (%)	Y.S. _C /Y.S. _T	Formability (mm)
A6	193.9	302.0	17.3	0.207	123.3	415.9	12.0	0.64	2.8
AZ603	207.5	310.1	19.4	0.199	131.5	434.4	11.9	0.63	2.0
AZ61	211.5	323.7	21.7	0.202	138.8	448.1	12.5	0.66	2.4
AZ62	219.8	336.9	17.9	0.195	142.1	474.3	11.9	0.65	2.8
AZ64	231.3	341.8	10.3	0.196	173.9	507.3	12.7	0.75	2.6

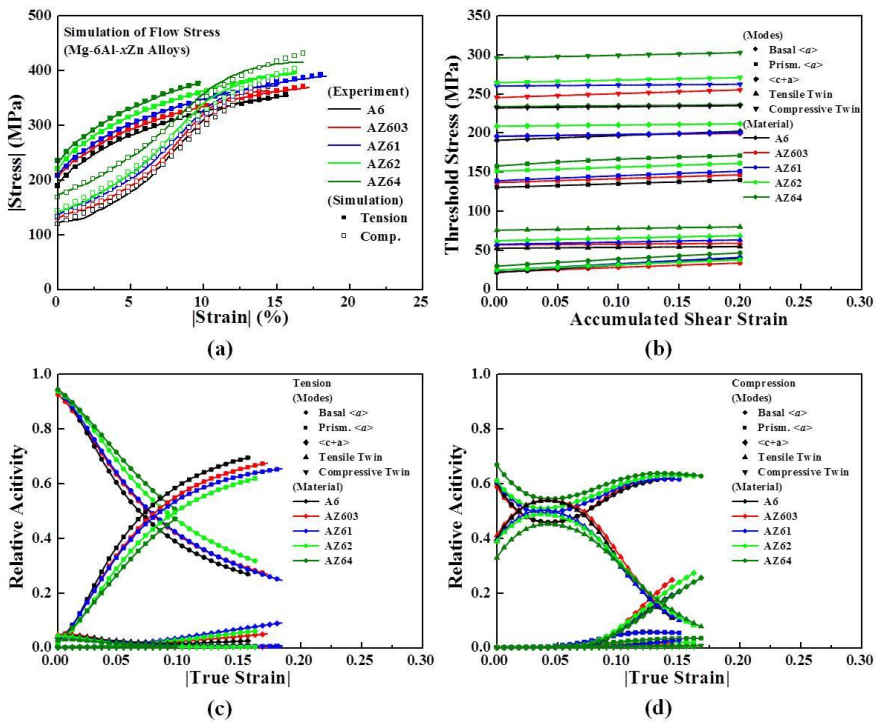


Figure 3.18 VPSC simulation results of annealed Mg-6Al-xZn alloys; (a) experimental and simulated stress-strain curves, (b) hardening curves of deformation modes, (c) relative activities during tensile deformation and (d) relative activities during compressive deformation.

3.3.7 Effects of alloying elements on grain size, texture and yield isotropy

Fig. 3.19 shows the relationship between average grain size of annealed Mg-6Al-X alloys and contents of alloying elements such as Mn, Ca, Sn, Sr and Zn. In all series Mg alloys, it shows that increasing of element contents, average grain size of Mg alloys generally decreases. Especially, Ca and Sr addition on Mg-6Al alloy play a role in grain refinement of Mg-6Al-X alloys. AX61 alloy has the smallest grain size of 5.2 μ m and AJ61 alloy has the second smallest grain size of 5.4 μ m. Formation of small grain size by Ca and Sr addition may be related to appearance of second phase particles precipitated during TRC process. Max. solid solubility of Ca and Sr in Mg-6Al is 0.005 and 0.014wt.% that is relatively smaller contents compared to other alloying elements such Al, Sn and Zn. Therefore, lots of second phases related to Ca and Sr elements could be attributed to grain refinement caused by Zener pinning effects. Fig. 3.20 indicates the relationship between intensity of (0002) pole figures and contents of alloying elements. All series Mg alloys do not significantly change strong basal texture by increasing contents of elements and their intensities of Mg alloys are approximately from 5 to 9. However, It can be seen that Ca, Sr and Zn addition on Mg-6Al alloy effectively decreases the intensity of basal texture, however, the addition of Mn and Sn elements slightly increases the intensity of (0002) pole figures. Fig. 3.21 shows the values of yield isotropy of Mg-6Al-X alloys as a function of contents of alloying elements. Generally, all alloys show that increasing the amount of alloying elements increases the yield isotropy of Mg-6Al-X alloys. Mg-6Al-xMn, Mg-6Al-xCa and Mg-6Al-xSr alloys have more positive effects on enhancement of yield isotropy compared to the rest of alloying elements and those alloying elements could

rapidly increase the yield isotropy of Mg-6Al-X alloys within the low content addition. It may be thought that enhanced yield isotropy is attributed to grain size and texture evolution. Generally, yield isotropy can be affected by grain size, texture and deformation behavior, etc. It has been reported that tensile-compressive mechanical isotropy is related to activation of tension twins [44]. Formation of strong basal texture can easily initiate the tension twins during compressive deformation, and smaller grain size of Mg alloys reduces the yield isotropy caused by suppression of twin generation. Thus, enhancement of yield isotropy by Sr and Ca additions is responsible for weaker basal texture and grain refinement resulting in modification of deformation behaviors during deformation. Fig. 3.22 shows the yield isotropy of Mg-6Al-X alloys and relative activity of tension twin in compression deformation at initial stage. It clearly shows that the yield isotropy is a close correlation with activity of tension twin or basal $\langle a \rangle$ slip. It can be also observed in this study that CRSS ratio (tension twin/basal $\langle a \rangle$ slip) generally increases with increasing the yield isotropy. Therefore, it is suggested that higher values of yield isotropy for Mg alloys could be obtained by increasing the CRSS ratio (tension twin/basal $\langle a \rangle$ slip) for accelerating the activity of basal $\langle a \rangle$ slip.

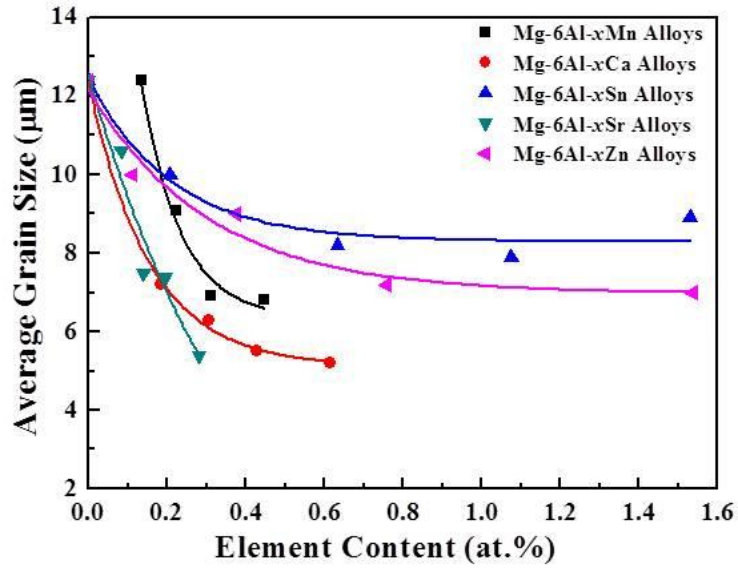


Figure 3.19 Average grain size of Mg-6Al-X alloys and the contents of alloying elements.

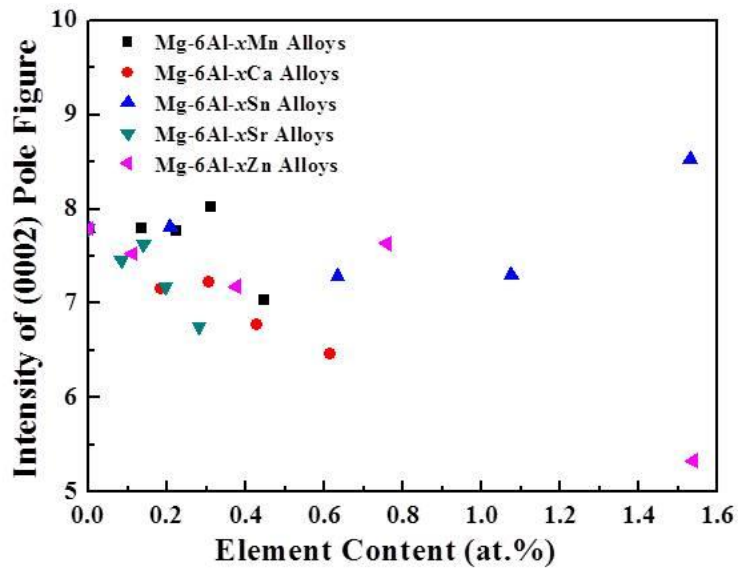


Figure 3.20 Max. intensity of (0002) pole figure of Mg-6Al-X alloys and the contents of alloying elements.

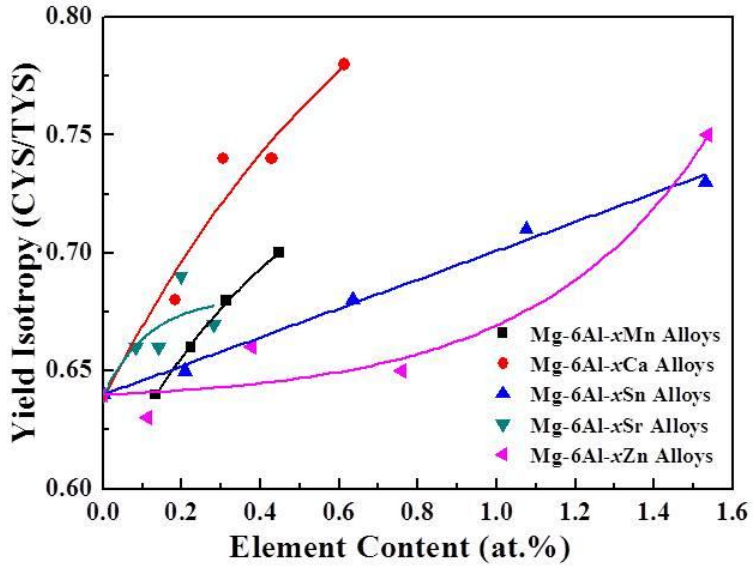


Figure 3.21 Yield isotropy of Mg-6Al-X alloys and the contents of alloying elements.

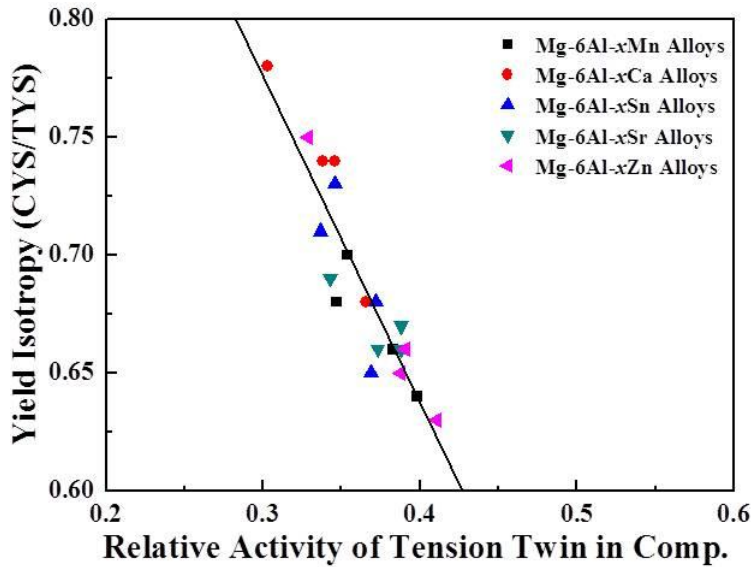


Figure 3.22 Yield isotropy of Mg-6Al-X alloys and the relative activity of tension twin in compression deformation at initial stage.

3.4 Conclusions

By using the TRC process, the influence of alloying elements such as Al, Mn, Ca, Sn, Sr and Zn on yield isotropy, deformation behavior and texture evolution of Mg-xAl and Mg-6Al-X alloys was investigated. Furthermore, mechanical properties and microstructural evolution of Mg-xAl and Mg-6Al-X alloys have also been studied. The main conclusions can be drawn as follows:

(1). Among the different alloying elements, Sr and Ca were the most effective elements for grain refinement on Mg-6Al alloy due to appearance of second phases to restrict the grain growth during hot deformation.

(2). The addition of Mn and Sn on Mg-6Al alloy had a tendency to increase the intensity of (0002) pole figure. However, the addition of Al, Ca, Sr and Zn elements decreased the intensity of basal texture.

(3). Yield isotropy decreased with increasing contents of alloying elements. Especially, Ca was the most powerful element to enhance the yield isotropy of Mg-6Al-X alloys. Furthermore, AX61 alloy showed the yield isotropy of around 0.80 due to weaker basal texture and small grain size.

(4). VPSC simulations showed that there was a close relationship between yield isotropy and relative activity of tension twin at initial stage in compression modes. Yield isotropy of Mg-6Al-X alloys gradually increased when the relative activity of tension twin decreased due to higher CRSS ratio (tension twin/basal $\langle a \rangle$ slip).

Bibliography

1. K. S. Song, H. C. Jung, K. S. Shin, "Fatigue crack propagation behavior of AZ31 Mg alloy in ultra-high vacuum", *Met. Mater. Int.* 17 (2011) pp. 397-402.
2. C. D. Yim, Y. M. Moon, B. S. You, Y. S. Na, J. S. Bae, "Microstructural change in gravity cast Mg-Ni alloys with Ni contents", *Met. Mater. Int.* 10 (2004) pp. 605-608
3. B. L. Mordike, T. Ebert, "Magnesium –properties-application-potential", *MSE A* 302 (2001) pp. 37-45.
4. S. S. Park, G. T. Bae, D. H. Kang, I. H. Jung, K. S. Shin, N. J. Kim, "Microstructural evolution in twin-roll strip cast Mg-Zn-Mn-Al alloy", *Scripta Mater.* 57 (2007) pp. 793-796.
5. T. T. Sasaki, J. D. Ju, K. Hono, K. S. Shin, "Heat-treatable Mg-Sn-Zn wrought alloy", *Scripta Mater.* 61 (2009) pp. 80-83.
6. S. S. Park, Y. S. Park, N. J. Kim, "Microstructure and properties of strip cast AZ91 Mg alloy", *Met. Mater. Int.*, 8 (2002) pp. 551-554.
7. M. Ferry, *Direct Strip Casting of Metals and Alloys*, Woodhead Publishing, Cambridge England, 2006.
8. X. P. Chen, D. Shang, R. Xiao, G. J. Huang, Q. Liu, "Influence of rolling ways on microstructure and anisotropy of AZ31 alloy sheet", *Trans. Nonferrous Met. Soc. China* 20 (2010) pp. s589-s593.
9. X. Gong, H. Li, S. B. Kang, J. H. Cho, S. Li, "Microstructure and mechanical properties of twin-roll cast Mg-4.5Al-1.0Zn sheets processed by differential speed rolling", *Mater. Des.* 31 (2010) pp. 1581-1587.
10. N. Stanford, "Micro-alloying Mg with Y, Ce, Gd and La for texture modification-A comparative study", *MSE A* 527 (2010) pp. 2669-2677.

11. N. Stanford, M. R. Barnett, "The origin of rare earth texture development in extruded Mg-based alloys and its effect on tensile ductility", *MSE A* 496 (2008) pp. 399-408.
12. J. Bohlen, S. Yi, D. Letzig, K. U. Kainer, "Effect of rare earth elements on the microstructure and texture development in magnesium-manganese alloys during extrusion", *MSE A* 527 (2010) pp. 7092-7098.
13. A. Singh, Y. Osawa, H. Somekawa, T. Mukai, "Ultra-fine grain size and isotropic very high strength by direct extrusion of chill-cast Mg-Zn-Y alloys containing quasicrystal phase", *Scripta, Mater.* 64 (2011) pp. 661-664.
14. A. K. Dahle, Y. C. Lee, M. D. Nave, P. L. Schaffer, D. H. StJohn, J. "Development of the as-cast microstructure in magnesium-aluminium alloys", *Light Metals 1* (2001) pp. 61-72.
15. C. H. Caceres, D. M. Rovera, "Solid solution strengthening in concentrated Mg-Al alloys", *J. Light Metals 1* (2001) pp. 151-156.
16. X. Huang, K. Suzuki, Y. Chino, M. Mabuchi, "Influence of aluminum content on the texture and sheet formability of AM series magnesium alloys", *MSE A* 633 (2015) pp. 144-153.
17. Z. Bian, A. Tripathi, H. Yu, N. D. Nam, L. M. Yan, "Effect of aluminum contents on the texture and mechanical behavior of Mg-1wt% Mn wrought magnesium alloys", *MSE A* 639 (2015) pp. 320-326.
18. Q. Yang, A. K. Ghosh, "Deformation behavior of ultrafine-grain AZ31B Mg alloy at room temperature", *Acta Mater.* 54 (2006) pp. 5159-5170.
19. S. W. Xu, K. Ohishi, S. Kamado, F. Uchida, T. Homma, K. Hono, "High-strength extruded Mg-Al-Ca-Mn alloy", *Scripta Mater.* 65 (2011) pp. 269-272.
20. N. Tahreen, D. L. Chen, M. Nouri, D. Y. Li, "Influence of aluminum

- content on twinning and texture development of cast Mg-Al-Zn alloy during compression”, *J. Alloys Comp.* 623 (2015) pp. 15-23.
21. S. M. Yin, C. H. Wang, Y. D. Diao, S. D. Wu, S. X. Li, “Influence of grain size and texture on the yield asymmetry of Mg-3Al-1Zn alloy”, *J. Mater. Technol.* 27 (2011) pp. 29-34.
 22. A. Chapuis, J. H. Driver, “Temperature dependency of slip and twinning in plane strain compressed magnesium single crystals”, *Acta Mater.* 59 (2011) pp. 1986-1994.
 23. S. A. Khan, Y. Miyashita, Y. Mutoh, Z. B. Sajuri, “Influence of Mn content on mechanical properties and fatigue behavior of extruded Mg alloys”, *MSE A* 420 (2006) pp. 315-321.
 24. L. B. Tong, M. Y. Zheng, S. W. Xu, S. Kamado, Y. Z. Du, X. S. Hu, K. Wu, W. M. Gan, H. G. Brokmeir, G. J. Wang, X. Y. Lv, “Effect of Mn addition on microstructure, texture and mechanical properties of Mg-Zn-Ca alloy”, *MSE A* 528 (2011) pp. 3741-3747.
 25. X. Huang, K. Suzuki, A. Watazu, I. Shigematsu, N. Saito, “Effects of manganese addition on microstructure and press formability of hot-rolled Mg-Al-Zn alloy sheets”, *J. Mater. Res.* 23 (2008) pp. 3029-3039.
 26. J. Y. Lee, Y. S. Yun, W. T. Kim, D. H. Kim, “Twinning and texture evolution in binary Mg-Ca and Mg-Zn alloys”, *Met, Mater, Int.*, 20 (2014) pp. 885-891.
 27. B. C. Suh, M. S. Shim, K. S. Shin, N. J. Kim, “Current issues in magnesium sheet alloys: Where do we go from here?”, *Scripta Mater.* xxx (2014) pp. xxx-xxx.
 28. S. Wei, T. Zhu, M. Hodgson, W. Gao, “Effects of Sn addition on the microstructure and mechanical properties of as-cast, rolled and annealed Mg-4Zn alloys”, *MSE A* 585 (2013) pp. 139-148.

29. Y. C. Lee, A. K. Dahle, D. H. StJohn, "The role of solute in grain refinement of magnesium", *Metall. Mater. Trans. A* 31A (2000) pp. 2895-2906.
30. E. Doernberg, A. Kozlov, R. Schmid-Fetzer, "Experimental investigation and thermodynamic calculation of Mg-Al-Sn phase equilibria and solidification microstructures", *JPEDAV* (2007) 28 pp. 523-535.
31. T. T. Sasaki, K. Yamamoto, T. Honma, S. Kamado, K. Hono, "A high-strength Mg-Sn-Zn-Al alloy extruded at low temperature", *Scripta Mater.* 59 (2008) pp. 1111-1114.
32. F. Qi, D. Zhang, X. Zhang, X. Xu, "Effect of Sn addition on the microstructure and mechanical properties of Mg-6Zn-1Mn alloy", *J. Alloys Comp.* 585 (2014) pp. 656-666.
33. M. Masoumi, M. Pekguleryuz, "Effect of Sr on the texture of rolled Mg-Mn-based alloys", *Mater. Letters* 71 (2012) pp. 104-107.
34. S. S. Park, W. J. Park, C. H. Kim, B. S. You, N. J. Kim, "The twin-roll casting of magnesium alloys", *JOM* 61 (2009) pp. 14-18.
35. Y. Xu-yue, Z. Ya-kun, H. Miura, T. Sakai, "Static recrystallization behavior of hot-deformed magnesium alloy AZ31 during isothermal annealing", *Trans. Nonferrous Met. Soc. China* 20 (2010) pp. 1269-1274.
36. H. Borkar, M. Hoseini, M. Pekguleryuz, "Effect of strontium on flow behavior and texture evolution during the hot deformation of Mg-1wt%Mn alloy", *MSE A* 537 (2012) pp. 49-57.
37. M. Yuasa, N. Miyazawa, M. Hayashi, M. Mabuchi, Y. Chino, "Effects of group II elements on the cold stretch formability of Mg-Zn alloys", *Acta Mater.* 83 (2015) pp. 294-303.
38. W. N. Tang, S. S. Park, B. S. You, "Effect of the Zn content on the microstructure and mechanical properties of indirect-extruded Mg-5Sn-xZn

- alloys”, *Mater. Design* 32 (2011) pp. 3537-3543.
39. D. W. Kim, B. C. Suh, M. S. Shim, J. H. Bae, D. H. Kim, N. J. Kim, “Texture evolution in Mg-Zn-Ca alloy sheets”, *Metall. Mater. Trans. A* 44A, (2013), pp. 2950-2961.
40. A. Akhtar, E. Teghtsoonian, “Solid solution strengthening of magnesium single crystals-II The effect of solute on the ease of prismatic slip”, *Acta Metall.* 17 (1969), pp. 1351-1356.
41. X. Huang, K. Suzuki, N. Saito, “Textures and stretch formability of Mg-6Al-1Zn magnesium alloy sheets rolled at high temperatures up to 793K”, *Scripta Mater.* 60 (2009) pp. 651-654.
42. X. Huang, K. Suzuki, Y. Chino, M. Mabuchi, “Influence of initial texture on rolling and annealing textures of Mg-3Al-1Zn alloy sheets processed by high temperature rolling”, *J. Alloys Comp.* 537 (2012) pp. 80-85.
43. A. H. Blake, C. H. Caceres, “Solid-solution hardening and softening in Mg-Zn alloys”, *MSE A* 483-484 (2008) pp. 161-163.
44. Y. Chino, K. Kimura, M. Hakamada, M. Mabuchi, “Mechanical anisotropy due to twinning in an extruded AZ31 Mg alloy”, *MSE A* 485 (2008) pp. 311-317.

Chapter 4. Characterization of TRC Mg-Zn-X-Ca alloys for enhanced room temperature formability

4.1 Introduction

Twin roll casting (TRC) is a promising process by which to fabricate strip plates, such as stainless steel and Al alloy sheets. Recently, it was reported that commercial Mg alloy sheets can be successfully fabricated through the TRC process at a low cost [1-2]. TRC Mg alloys exhibit good mechanical properties; however, their lower formability at room temperature is a drawback when applied to automobile components due to high cost of sheet forming. Therefore, the development of highly formable, high-strength TRC Mg alloys is necessary in order to widespread the application of Mg sheets and reduce the weight of vehicles. The high formability of Mg alloys is closely related to their weaker basal textures or random textures. There have been numerous studies of texture modifications of strong basal textures that are vulnerable to room-temperature formability. One approach that changes a strong basal texture into a random texture involves some form of severe deformation (SDF), such as equal-channel angular extrusion (ECAE), differential speed rolling (DSR) or cross rolling to develop weaker basal textures [3-5]. However, these types of processes increase the production costs, and the shapes of Mg alloys with which these processes can be applied are limited. Another approach to change the texture of Mg alloys involves the addition of alloying elements such as Ca, Sr, Y or RE, among others.

Yuasa *et al.* [6] studied the effects of additions of Ca and Sr on Mg-Zn alloys. Mg-Zn-Ca and Mg-Zn-Sr alloys exhibit weaker basal textures and high formability with Erichsen values of 7.3~8.2mm due to the higher stacking fault energy. Chino *et al.* [7] studied the effects of the Y content on Mg-Y alloys, finding that Y as an alloying element could increase the activity of prismatic $\langle a \rangle$ cross slip, resulting in the formation of weaker textures, also finding that Mg-1.5Zn-xY alloys show excellent Erichsen values in the range of 5.7~9.2mm. It has also been reported that Mg-Zn-Mn-RE alloys show weak and random basal textures with a broader distribution of basal poles toward TD and with formability at room temperature of 9.5mm, which is nearly identical to that of Al alloys [8]. Despite the fact that they exhibit excellent room-temperature formability, they are not fabricated through the TRC process and do not have sufficient yield strength compared to that of Al alloys. Other research reported numerous correlations between the degree of formability and the r value as well as between the formability and work-hardening capacity, which is the inverse of the yield ratio [9-11]. However, the relationship between the formability and deformation behaviors of Mg alloys has not yet been investigated.

In the present study, TRC Mg-4Zn-X-Ca alloys were characterized to develop new highly formable, high-strength TRC Mg alloys. The microstructures and mechanical properties of Mg-4Zn-X-Ca alloys were investigated by optical microscopy and in tensile and compressive tests. The texture evolution of TRC Mg-4Zn-X-Ca alloys was examined by X-ray diffraction analysis. In order to find the correlation between the formability and deformation behaviors with different compositions, VPSC simulations

were carried out to calculate the contribution of the deformation modes of tension and compression deformation based on the experimental results.

4.2 Experimental Procedures

Alloys with nominal compositions (in wt.%) of Mg-4Zn-0.3Mn (Z4), Mg-4Zn-0.3Ca-0.3Mn (ZX40), Mg-4Zn-0.3Al-0.3Ca-0.3Mn (ZAX400), Mg-4Zn-0.3Y-0.3Ca-0.3Mn (ZWX400), Mg-4Zn-0.3Cu-0.3Ca-0.3Mn (ZCX400) and Mg-4Zn-0.3Si-0.3Ca-0.3Mn (ZSX400) were subjected to a TRC process on a laboratory scale. The chemical compositions of the Mg-4Zn-X-Ca alloys are listed in Table 4.1. The alloys were melted at 720~730°C using a steel crucible under protective gas and were transferred to a preheated nozzle held at 650°C, followed by TRC process. The casting speed was 3m/min and the roll gap was set to 2.0mm. The thickness of the TRC sheets was approximately 3.7 ~ 3.9mm. The TRC sheets were subsequently homogenized at 350°C for 24hr, followed by water quenching. The homogenized sheets were hot rolled at 350°C for four passes with a total rolling reduction of 65%. Before the final rolling pass, the rolled samples were annealed at 350°C for 12hr followed by final rolling with a thickness of 1.0mm. The rolled sheets were subsequently annealed at 350°C for 1hr, followed by water quenching. The tensile tests and compression tests were performed at a strain rate of 2×10^{-4} /sec using an Instron 5582 machine. The loading axis was parallel to the rolling direction. The stretch formability of the sheets was evaluated by an Erichsen cupping test using a graphite-type lubricant. The punch diameter and speed were 20mm and 5mm/min (for a 55mm square-type specimen), respectively. Figures of annealed sheets were measured from four different planes: $\{10\bar{1}0\}$, $\{0002\}$, $\{10\bar{1}1\}$, and $\{11\bar{1}0\}$ using the Schulz reflection method by a PANalytical X'Pert PRO X-ray diffractometer with Cu K source. The macro-texture was analyzed on the mid-thickness planes perpendicular to the normal direction. Complete pole

figures were acquired from the orientation distribution function (ODF) calculated using the arbitrarily defined cells (ADC) method in the LaboTex 3.0 software. The texture of deformed samples was characterized using EBSD using FE-SEM (SU70, HITACHI) fitted with a TSL EBSD camera operating at 20kV, 70° tilting angle. VPSC simulations were conducted for both tension and compression deformation in order to predict the contribution of various deformation modes using the Voce-type hardening rule and the predominant twin reorientation scheme (PTR) model for hardening and twinning models, respectively.

Table 4.1 Chemical compositions (wt.%) of the investigated alloys.

Alloys	Compositions (wt.%)							
	Zn	Mn	Ca	Al	Si	Cu	Y	Mg
Z4	4.5008	0.2782	-	-	-	-	-	Bal.
ZX40	4.2794	0.3304	0.2155	-	-	-	-	Bal.
ZAX400	4.5094	0.2297	0.2916	0.3045	-	-	-	Bal.
ZWX400	4.3198	0.1783	0.3027	-	-	-	0.3592	Bal.
ZCX400	4.2036	0.2403	0.2983	-	-	0.3117	-	Bal.
ZSX400	4.1518	0.2410	0.2363	-	0.220	-	-	Bal.

4.3 Results and discussions

4.3.1 Microstructure of Mg-4Zn-X-Ca alloys

Cross-sectional micrographs of the Z4, ZX40, ZAX400, ZWX400, ZCX400 and ZSX400 TRC alloys are shown in Fig. 4.1. This figure shows that all of the alloys exhibit centerline segregation, which is detrimental to the mechanical properties and the surface quality of the strip plates; this type of segregation forms along the casting direction due to the partition redistribution of solute atoms during the twin roll casting process. However, the volume fraction of the segregation is not excessive, and there is no formation of inverse segregation, which is linked from the center to the surface. The Z4, ZX40, ZAX400, ZCX400 and ZSX400 alloys show an equiaxed dendrite microstructure, whereas the ZWX400 alloy shows an inclined columnar dendritic microstructure due to its different solidification behavior, which was affected by factors such as the freezing range, second phases, and the processing parameters [2,12-13]. In order to homogenize the as-cast microstructure, all of the samples were subjected to a heat treatment at 350°C for 24hr before the hot-rolling process. Fig. 4.2 shows the optical micrographs of the rolled Mg-4Zn-X-Ca alloys. These alloys exhibit a deformed microstructure with deformed twins. Compared to the Z4 alloy, the ZX40 alloy shows a refined microstructure due to intermetallic compounds related to Ca, similar to the microstructure of the ZWX400 and ZCX400 alloys. However, the ZAX400 alloy, containing Al alloying element, shows the smallest grain size with a relatively low twin volume fraction, while the ZSX400 alloy shows a refined recrystallized microstructure around the grain boundary caused by dynamic recrystallization via the hot-rolling process. After the annealing process,

significant changes in the microstructures of the Mg-4Zn-X-Ca alloys were observed, as shown in Fig. 4.3. All of the alloys exhibit fully annealed and uniform microstructures, and much of the deformed twinning disappears due to static recrystallization. The average grain sizes for the Mg-4Zn-X alloys were 14.4, 9.6, 7.5, 10.3, 10.8 and 12.1 μm for the Z4, ZX40, ZAX400, ZWX400, ZCX400 and ZSX400 alloys, respectively. Compared to the Z4 alloy, the ZX40 alloy appears to have a fine microstructure due to the addition of Ca. It has been reported that the Ca alloying element plays a major role in the grain refinement of Mg alloys due to intermetallic compounds related to Ca, which impede the grain boundary, thus improving the resistance to grain growth during the hot-rolling and heat-treatment processes [14]. From the microstructure, a number of particles that appear to be related to Ca were observed in the α -Mg matrix of the ZX40 alloy but not the Z4 alloy. In addition, among the different Mg alloys, the ZAX400 alloy exhibits the smallest grain size, at 7.5 μm . This may be caused by the different types of precipitates which formed during the TRC casting step as compared to the ZX40 alloy. The ZAX400 alloy may consist of MgZn, $\text{Ca}_2\text{Mg}_6\text{Zn}_3$, Mg_2Ca , $(\text{Mg},\text{Al})_2\text{Ca}$, Al_8Mn_5 and α -Mn phases; however, the ZX40 alloy can have only MgZn, $\text{Ca}_2\text{Mg}_6\text{Zn}_3$ and α -Mn phases according to thermodynamic simulations under the Scheil condition, suggesting that numerous second particles can be precipitated by an addition of Al in the Mg-Zn-Ca alloy system and that they may play a role in restricting the grain growth via Zener pinning effects during the hot-rolling process.

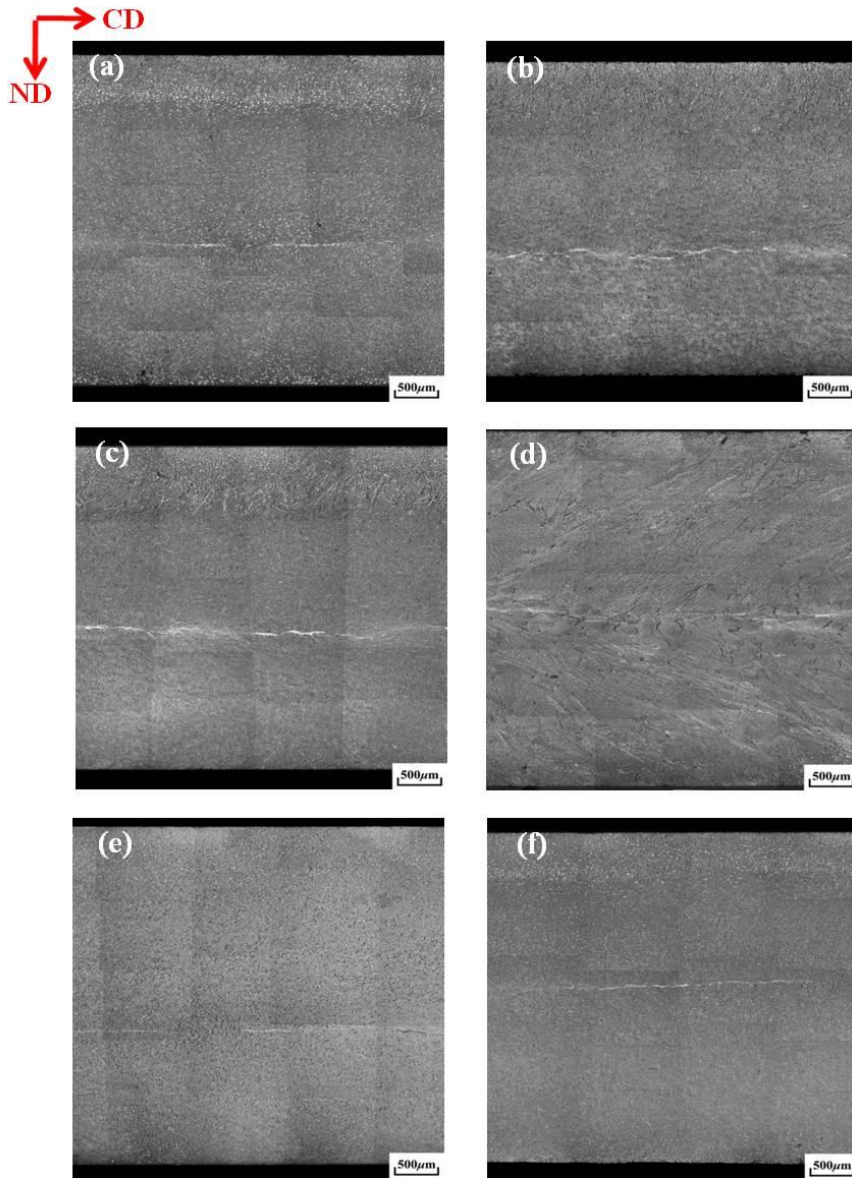


Figure 4.1 Microstructures of as-cast Mg-4Zn-X-Ca alloys; (a) Z4, (b) ZX40, (c) ZAX400, (d) ZWX400, (e) ZCX400 and (f) ZSX400.

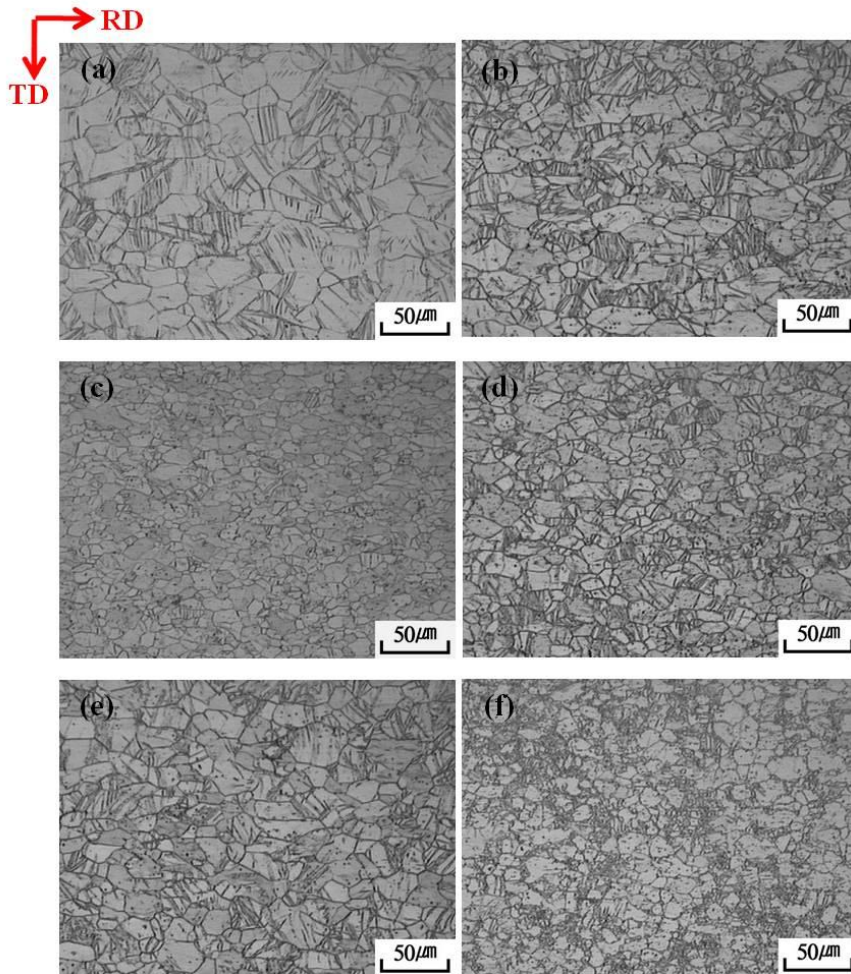


Figure 4.2 Microstructures of as-rolled Mg-4Zn-X-Ca alloys; (a) Z4, (b) ZX40, (c) ZAX400, (d) ZWX400, (e) ZCX400 and (f) ZSX400.

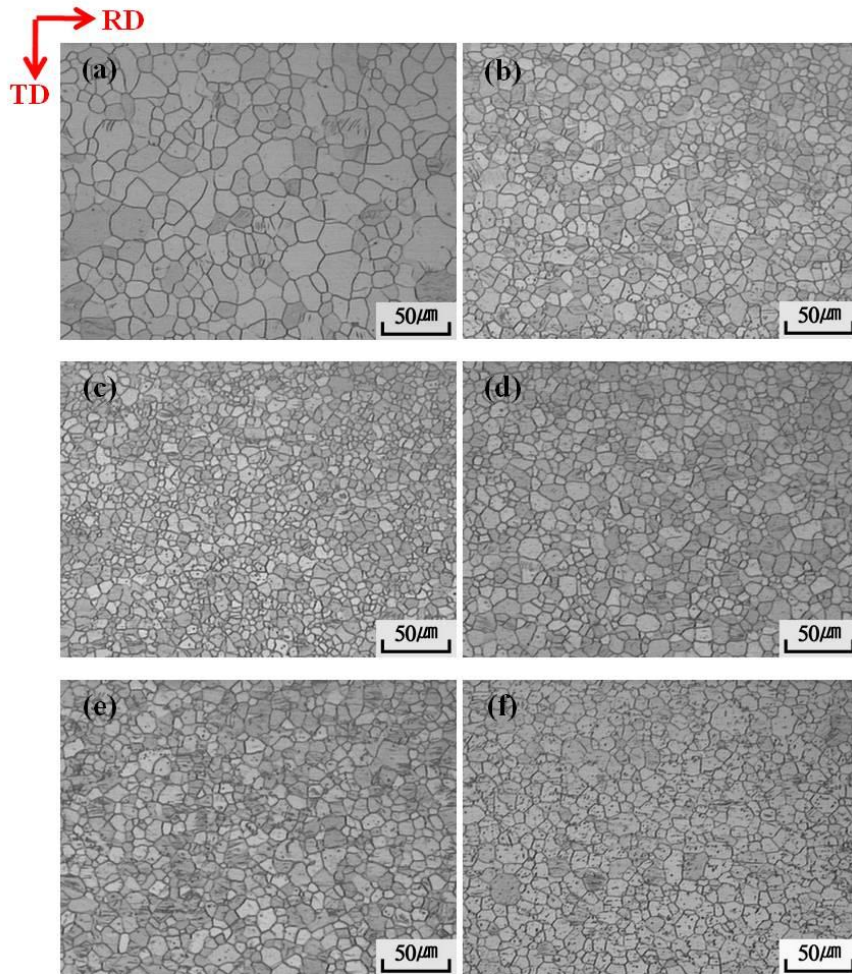


Figure 4.3 Microstructures of as-annealed Mg-4Zn-X-Ca alloys; (a) Z4, (b) ZX40, (c) ZAX400, (d) ZWX400, (e) ZCX400 and (f) ZSX400.

4.3.2 Texture of Mg-4Zn-X-Ca alloys

Figure 4.4 shows the (0002) pole figures of the Mg-4Zn-X-Ca alloys rolled at 350°C. The rolled Z4 and ZSX400 alloys show similar basal textures, i.e., typical Mg wrought textures. Both alloys exhibit a strong basal texture parallel to the rolling direction. The intensity levels of the (0002) pole figure are 9.537 and 9.044 for the Z4 and ZSX400 alloys, respectively. The formation of a strong basal texture in Z4 and ZSX400 alloys could be related to the dependence on the main deformation modes during the hot rolling process. It has been reported that basal $\langle a \rangle$ slip mostly accommodates the strain during rolling, resulting in a strong basal texture which is formed by the rotation of the slip plane and the slip direction toward the rolling plane and the rolling direction, respectively [15]. However, the ZX40, ZAX400, ZWX400 and ZCX400 alloys have completely different (0002) pole figures compared to the Z4 and ZSX400 alloys, which shows a strong basal texture. Their basal textures exhibit a broadening of the angular distribution of the basal poles from the ND toward the RD-TD distribution. The formation of a double peak for the RD case could be attributed to the activation of the pyramidal $\langle c+a \rangle$ slip system due to high-temperature deformation with low CRSS values of the pyramidal $\langle c+a \rangle$ slip [16]. Furthermore, it has been suggested that deformation twins, especially double twins, can tilt the basal texture toward the RD via the rotation of the deformed twin area by 38° [17]. Recently, the splitting of the basal pole toward the TD was thought to be related to the activation of the prismatic $\langle a \rangle$ slip during the hot-rolling process [8]. Another research has also studied how the addition of Ca to the Mg alloy could reduce the stacking fault energy of the prismatic slip, resulting in greater activation of the prismatic

$\langle a \rangle$ slip [6]. In addition, these cases exhibit lower intensity of the (0002) pole figures as compared to that of the Z4 alloy. The intensity levels of the (0002) pole figure are 4.735, 4.243, 4.424 and 4.892 for the ZX40, ZAX400, ZWX400 and ZCX400 alloys, respectively. This indicates that the addition of Ca to the Mg-4Zn-X alloy can effectively randomize the deformation textures, with the exception of the ZSX400 alloy, which has a strong basal texture. Figure 4.5 shows the basal texture of the annealed Mg-4Zn-X-Ca alloys. For the Z4 alloy, the intensity of the (0002) pole figure increases significantly from 9.537 (rolled) to 16.484 (annealed); however, the other alloys tend to decrease the intensity of the basal texture after the annealing process. The change in the intensity of the basal texture may depend on the different types of static recrystallization. It has been reported that when continuous recrystallization occurs in Mg alloys, the intensity of the (0002) pole figure increases significantly. However, the occurrence of discontinuous recrystallization results in the formation of a weaker basal texture [18]. Therefore, significant evolution of the texture of Mg alloys can be induced by a discontinuous recrystallization process. It is interesting to note that the ZX40, ZAX400, ZWX400 and ZCX400 alloys exhibit weaker basal textures with the splitting of the basal poles from the ND to TD, which is favorable for room-temperature formability. However, the Z4 and ZSX400 alloys show strong basal textures. Lee *et al.* suggested that the splitting of the basal poles to the TD is related to the operation of compressive and secondary twins in the ZX31 alloy due to local lattice distortion and the reduced stacking fault energy caused by the addition of Ca [18]. This suggests that the activation of non-basal slips and compression twin can be accelerated by the addition of Ca for random textures of rolled and annealed Mg alloys.

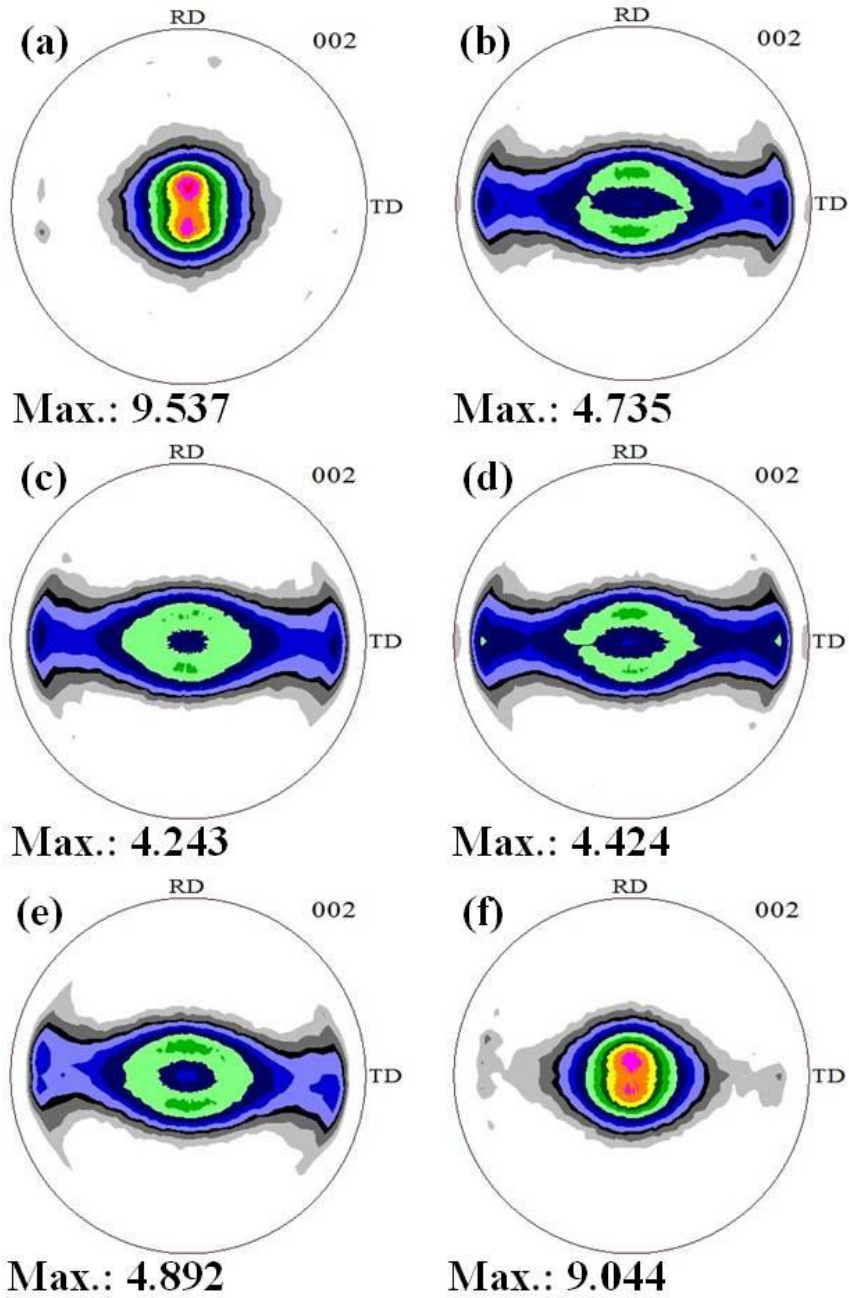


Figure 4.4 (0002) pole figures of as-rolled Mg-4Zn-X-Ca alloys; (a) Z4, (b) ZX40, (c) ZAX400, (d) ZWX400, (e) ZCX400 and (f) ZSX400.

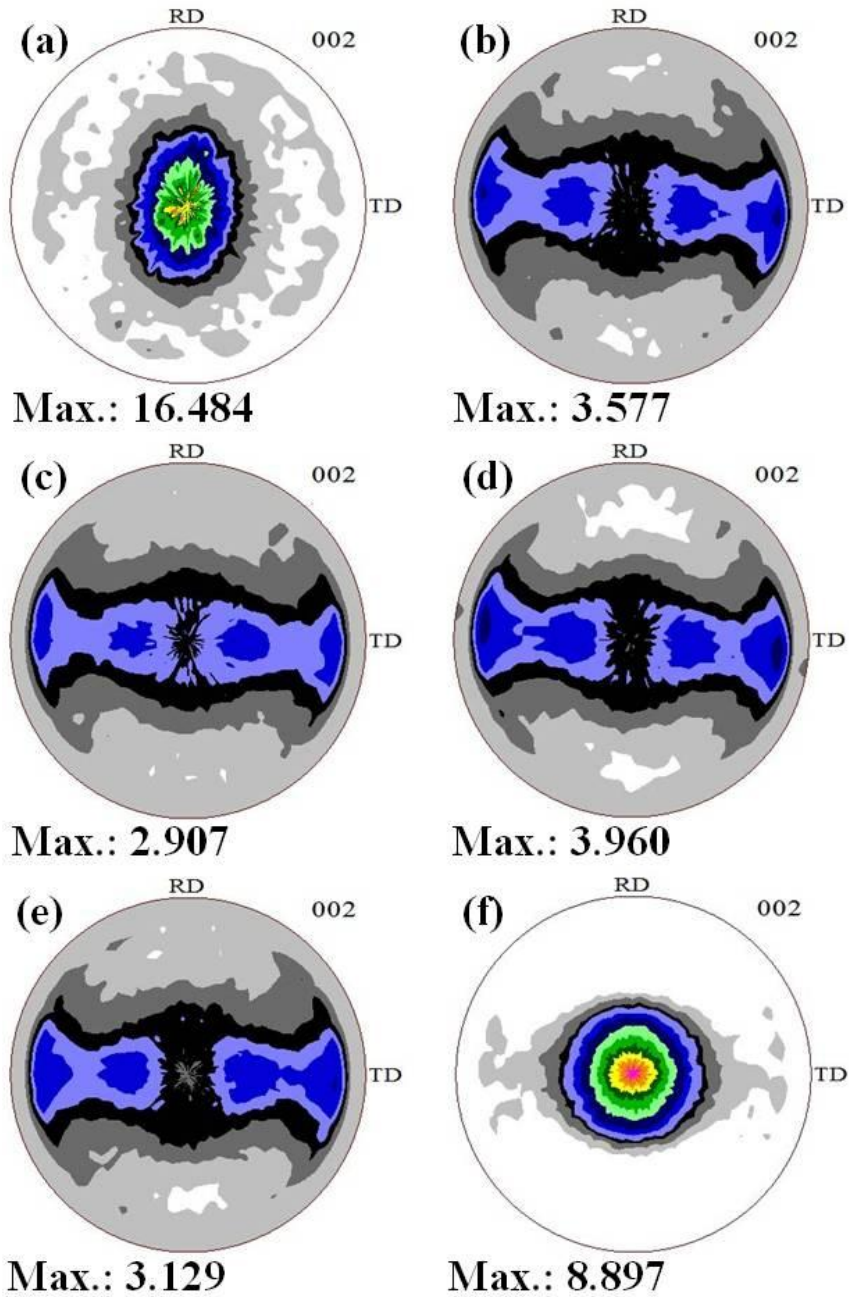


Figure 4.5 (0002) pole figures of as-annealed Mg-4Zn-X-Ca alloys; (a) Z4, (b) ZX40, (c) ZAX400, (d) ZWX400, (e) ZCX400 and (f) ZSX400.

4.3.3 Mechanical Properties & formability of Mg-4Zn-X-Ca alloys

Fig. 4.6 presents the mechanical properties of the annealed Mg-4Zn-X-Ca alloys. The solid line shows the tensile stress-strain curves and the dashed line shows the compressive stress-strain curves. For the tensile strain-stress curves, the yield strength levels of the Mg-4Zn-X-Ca alloys are 141.3, 156.1, 189.3, 175.9, 167.3 and 170.8MPa for the Z4, ZX40, ZAX400, ZWX400, ZCX400 and ZSX400 alloys, respectively. This result indicates that a Ca addition to the Mg-4Zn alloy improves the yield strength compared to the Z4 alloy. The increase in the yield strength may be caused by grain refinement strengthening and a precipitate-hardening mechanism stemming from the addition of Ca. From the annealed microstructure, it was noted that a fine microstructure and uniformly distributed second particles existed in the ZX40 alloy. The ZAX400 alloy showed the highest yield strength among the different alloys owing to the appearance of numerous second phases which precipitated, resulting in pinning effects during the deformation process. The ultimate strength is not affected by the addition of Ca compared to the Z4 and ZX40 alloys, which show identical UTS values. However, the ZAX400, ZWX400, ZCX400 and ZSX400 alloys increase the UTS due to the addition of Al, Y, Cu and Si compared to the ZX40 alloy. In addition, the elongation to failure values of the Mg-4Zn-X-Ca alloys are 24.7, 23.9, 22.2, 25.6, 24.5 and 17.9% for Z4, ZX40, ZAX400, ZWX400, ZCX400 and ZSX400 alloys, respectively. All alloys show greater than 20% elongation without the ZSX400 alloy indicating that a significant improvement in the elongation can be realized in Mg-4Zn-X-Ca alloys. With regard to the compressive strain-stress curves, the compressive yield strength levels of the Mg-4Zn-X-

Ca alloys are 77.3, 126.2, 139.4, 134.6, 126.9 and 110.9MPa for Z4, ZX40, ZAX400, ZWX400, ZCX400 and ZSX400 alloys, respectively. This indicates that the increase in the compressive yield strength via the addition of Ca is higher than that of the tensile yield strength. This may be caused by grain refinement and texture evolution after the addition of Ca.

Generally, compressive deformation in Mg alloys is dominant due to the activity of tension twin [9]. The ZX40 alloy shows a smaller grain size and a weaker basal texture, thus suppressing the initiation of tension twin during compressive deformation. Therefore, the ZX40 alloy exhibits an improved yield isotropy (compressive yield strength/tensile yield strength) value of 0.81. The ZAX400, ZWX400 and ZCX400 alloys also show higher yield isotropy values exceeding 0.74; however, the ZSX400 alloy shows a relatively low value of the yield isotropy at 0.65 due to its strong basal texture, which is favorable for the initiation of tension twin. Table 4.2 summarizes the mechanical properties and formability of the Mg-4Zn-X-Ca alloys. Fig. 4.7 shows the samples after the Erichsen tests with the Mg-4Zn-X-Ca alloys. The Erichsen value of the Z4 alloy is only 3.8mm. However, the formability of the ZX40 alloy containing 0.3wt.% of Ca is 7.2mm, nearly double that of the Z4 alloy. The formability values of the ZAX400, ZWX400 and ZCX400 alloys are 7.5, 7.6 and 8.0mm, respectively. Specifically, the ZAX400 alloy shows an enhanced tensile yield strength and improved room-temperature formability, comparable to those of Al alloys. Fig. 4.8 shows the Erichsen values and yield strength levels of the Mg-4Zn-X-Ca alloys, with the data for highly formable Mg alloys included for comparison. This figure shows that Mg-4Zn-X-Ca alloys which are developed in this study, exhibit excellent formability close to 8.0mm and good yield strength of approximately 189MPa.

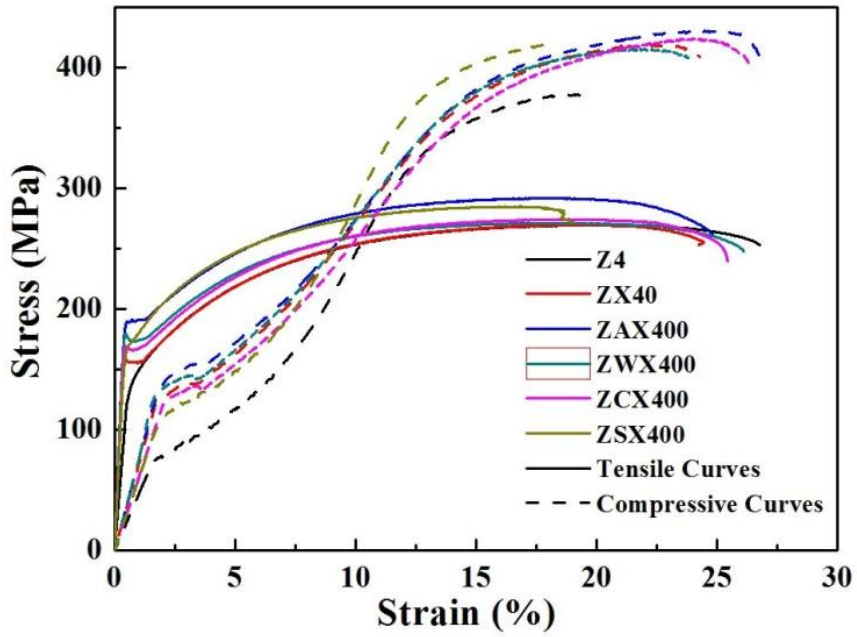


Figure 4.6 Nominal strain-stress curves of Mg-4Zn-X-Ca alloys.

Table 4.2 Mechanical properties and formability of Mg-4Zn-X-Ca alloys.

Alloys	Tensile Properties				Compressive Properties		Yield Isotropy	Formability
	Y. S. (MPa)	U. T. S. (MPa)	Elongation (%)	n	Y. S. (MPa)	Max. S. (MPa)	C.Y.S./T.Y.S.	Erichsen Value (mm)
Z4	141.3	269.8	24.7	0.273	77.3	377.4	0.55	3.8
ZX40	156.1	269.8	23.9	0.266	126.2	418.8	0.81	7.2
ZAX400	189.3	291.8	22.2	0.225	139.4	430.4	0.74	7.5
ZWX400	175.9	271.0	25.6	0.231	134.6	415.5	0.77	7.6
ZCX400	167.3	274.2	24.5	0.251	126.9	423.6	0.76	8.0
ZSX400	170.8	284.8	17.9	0.227	110.9	418.6	0.65	3.8

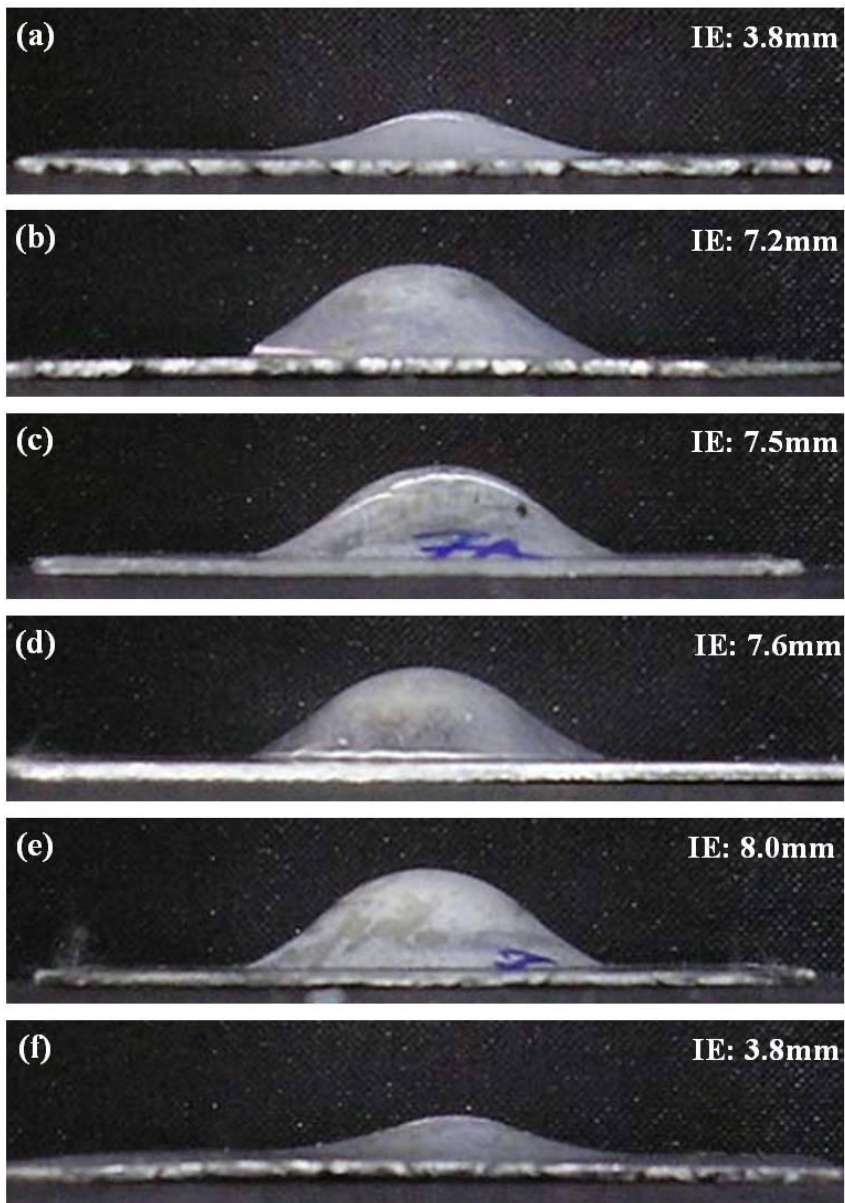


Figure 4.7 Circular blanks after Erichsen tests for Mg-4Zn-X-Ca alloys; (a) Z4, (b) ZX40, (c) ZAX400, (d) ZWX400, (e) ZCX400 and (f) ZSX400.

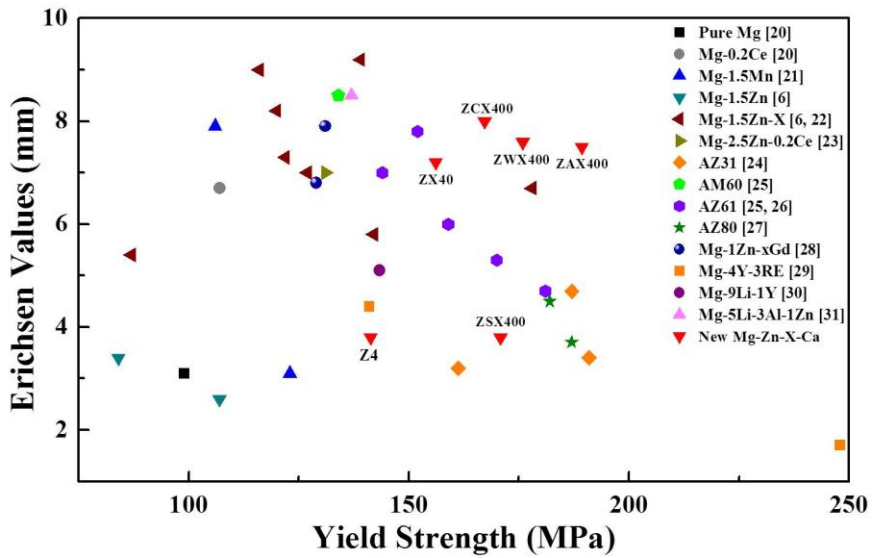


Figure 4.8 Relationship between Erichsen values and yield strength of Mg alloy and New Mg-4Zn-X-Ca alloys (investigated alloys in present study).

4.3.4 VPSC simulations of Mg-4Zn-X-Ca alloys

It was found in this study that an addition of Ca to the Mg-4Zn alloy significantly improves the room-temperature formability until it is comparable to that of Al alloys and enhances the yield isotropy, which is largely affected by the deformation behavior. In order to analyze the contribution of activated deformation modes, VPSC simulations of Mg-4Zn-X-Ca alloys were carried out to assess the tensile and compressive deformation. Figure 4.9 (a) shows both the experimental and simulated results, demonstrating the good agreement between them. Figure 4.9 (b) shows the hardening curves of the deformation modes, in this case the basal $\langle a \rangle$ slip, the prismatic $\langle a \rangle$ slip, the pyramidal $\langle c+a \rangle$ slip, tension twin and compression twin. These results show that all of the initial CRSS values of the ZX40 alloy increase compared to those of the Z4 alloy, which demonstrates lower mechanical properties, in this case the tension and compression properties. Specifically, the initial CRSS value of tension twin for the ZX40 alloy doubles upon the addition of the Ca alloying element. The initial CRSS values of tension twin in all alloys without ZSX400 increase from 30MPa to 62 ~ 63MPa. The increase of the initial CRSS values for the tension twin is mainly related to the texture evolution caused by the addition of Ca. The ZX40, ZAX400, ZWX400, ZCX400 alloys, which contain 0.3wt.% of Ca, show random basal textures which are unfavorable for the initiation of twin deformations due to the geometry condition, resulting in a significant increase of the CRSS values due to limited activation of tension twin. Figures 4.9 (c) and (d) present the evolution of the relative activities of the deformation modes during tensile and compressive deformation, respectively. For tension deformation, all of

the alloys show that the main deformation modes are basal $\langle a \rangle$ slip and prismatic $\langle a \rangle$ slip modes, which mainly accommodate the strain at a later stage. Furthermore, a small percentage of the strain can be accommodated by tension deformation at the initial stage, which is commonly observed in Mg alloys [6]. According to the strain, in the Mg-4Zn-X-Ca alloys, the relative activity of the basal $\langle a \rangle$ slip gradually decreases, whereas that of the prismatic $\langle a \rangle$ slip steadily increases. It was also found that the relative activity of the basal $\langle a \rangle$ slip increases upon the addition of Ca. The relative activity of the basal $\langle a \rangle$ slip for the ZX40 alloy is 0.45; however, that of the Z4 alloy is only 0.33. The increase by more than 1.3 times of the relative activity for the basal $\langle a \rangle$ slip may be induced by the texture evolution caused by the Ca addition, which is related to the Schmid factor. Fig. 4.10 shows the formation of deformation twins with increasing the amount of tensile strain from 2% to 10%. Z4 has the area fraction of tension twins increases from 0.28% at 2% strain to 0.1.21% at 10% strain. ZX40 with more random texture has the area fraction of tension twins increases from 0.35% at 2% strain to 0.64% at 10% strain. It shows that when tension twin occur during tensile test, the basal plane is tilted to TD. From the VPSC results, It shows that the tension twin in tension mode has the smaller relative activity compared to other slip systems and is not the main deformation mode to accommodate the strain. However, tension twinning attributes to texture evolution of Mg alloys from basal planes. For compression deformation, the basal $\langle a \rangle$ slip and tension twin are the predominant deformation modes. The relative activity of the basal $\langle a \rangle$ slip mode is always higher in all strain conditions; however, that of the tension twin steadily decreases past the peak position due to the reorientation induced by the tension twin. Large deformation of the pyramidal $\langle c+a \rangle$ slip

mode is active at a later stage due to the higher CRSS value in this case compared to other slip systems. In addition, the ZX40, ZAX400, ZWX400 and ZCX400 alloys, which have more random textures, exhibit different deformation behavior compared to the Z4 and ZSX400 alloys, which show a strong basal texture. The former alloys show high activity of the basal $\langle a \rangle$ slip, whereas the latter alloys tend to show low activity of basal $\langle a \rangle$ slip at all strain levels caused by the different CRSS ratio (tension twin/basal $\langle a \rangle$ slip). The initial CRSS ratio (tension twin/basal $\langle a \rangle$ slip) for the Z4 alloy is 1.13; however, that of the ZX40 alloy is 2.06. The CRSS ratio increases by more than 1.8 times upon an addition of Ca due to textural evolution and grain growth. Therefore, the ZX40, ZAX400, ZWX400 and ZCX400 alloys show high basal $\langle a \rangle$ slip activity, improving the yield isotropy due to higher values of the initial CRSS ratio (tension twin/basal $\langle a \rangle$ slip).

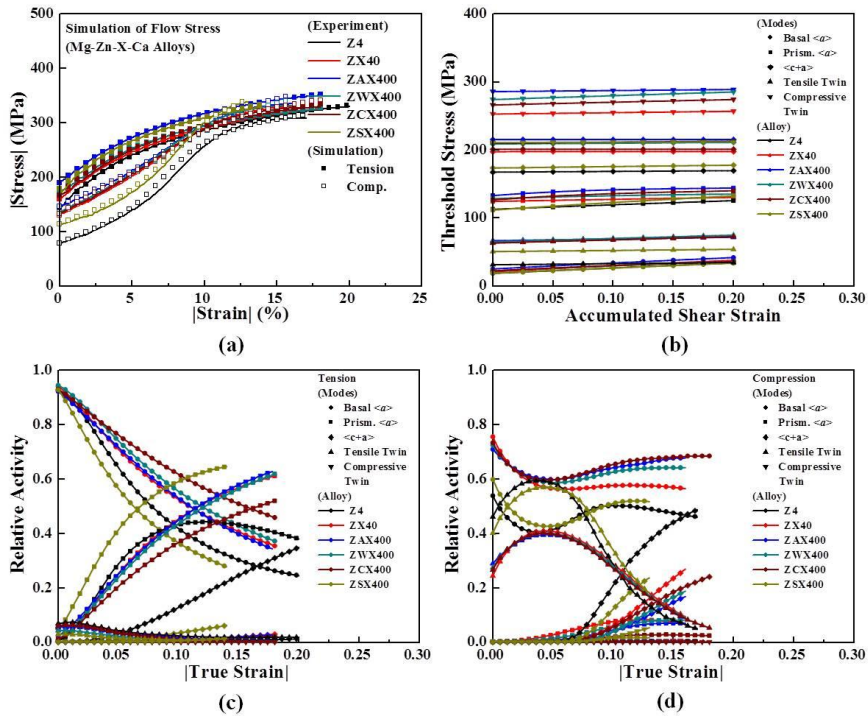


Figure 4.9 VPSC simulation results of annealed Mg-4Zn-X-Ca alloys rolled at 350°C; (a) experimental and simulated stress-strain curves, (b) hardening curves of deformation modes, (c) relative activities during tensile deformation and (d) relative activities during compressive deformation.

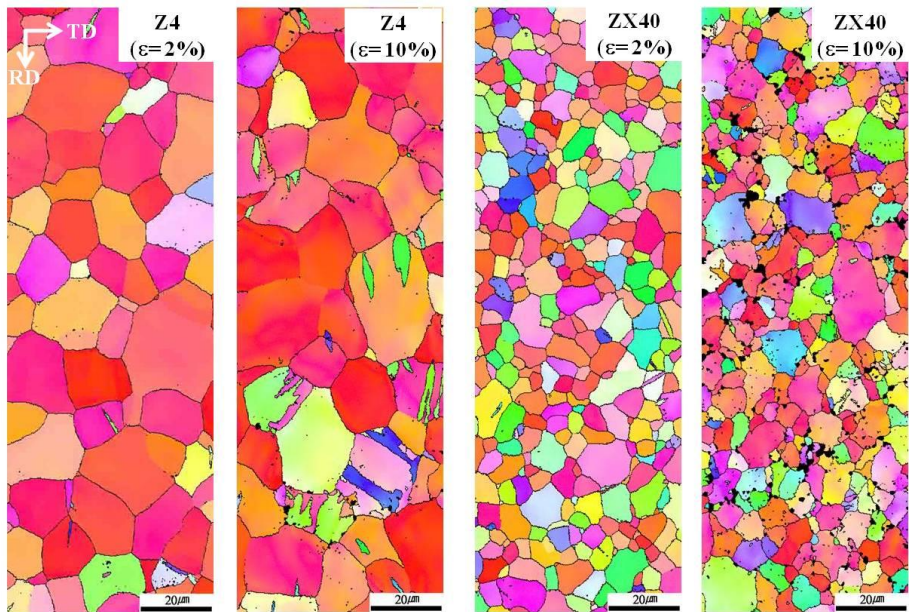


Figure 4.10 Inverse pole figure (IPF) map of Z4 and ZX40 alloy with deformed to $\epsilon = 2\%$ and 10% (Tensile loading is along RD).

4.3.5 Relationship between formability vs. yield isotropy vs. deformation behavior

Figure 4.11 shows the correlation between the relative basal $\langle a \rangle$ slip activity in the compression mode at the initial stage and the maximum intensity of the (0002) pole figures. This figure shows that there is a linear relationship between the intensity of the basal texture and the relative activity of the basal slip during compression deformation. The intensity of the (0002) pole figures steadily decreases with an increase in the relative basal $\langle a \rangle$ slip activity. The increased activity of basal $\langle a \rangle$ slip during compression may be caused by the restriction of twin deformations, especially tension twin. It has been reported that Mg alloys with strong basal textures have higher volume fractions of tension twin during compression [32-33]. This increases the relative basal $\langle a \rangle$ slip activity due to the low CRSS ratio compared to those of other slip systems. Therefore, the ZX40 and ZSX400 alloys have relatively lower basal $\langle a \rangle$ slip activity levels due to the formation of strong basal textures. Figure 4.12 shows the relationship between the basal $\langle a \rangle$ slip activity in the compression mode at the initial stage and the CRSS ratio (tension twin/basal $\langle a \rangle$ slip), showing that the increase in the basal slip activity during compression is mainly attributed to the large CRSS ratio (tension twin/basal $\langle a \rangle$ slip). For example, the initial CRSS values of the basal $\langle a \rangle$ slip and tension twin for the Z4 alloy are 17.8 and 30.6MPa, respectively, while those for the ZX40 alloy are correspondingly 20.1 and 63.1MPa. The initial CRSS values for both deformation modes increase due to the addition of Ca; however, a rapid increase in the CRSS value occurs upon tension twinning caused by the Ca

addition. Thus, the ZX40 alloy has high basal $\langle a \rangle$ slip activity compared to the Z4 alloy owing to the higher CRSS ratio.

As mentioned previously, there is a close relationship between deformation behavior and texture and the CRSS ratio (tension twin/basal $\langle a \rangle$ slip). It is also well known that the yield isotropy can be affected by the texture and the deformation behavior. Figure 4.13 indicates the relationship between the yield isotropy and the CRSS ratio (tension twin/basal $\langle a \rangle$ slip) of the Mg-4Zn-X-Ca alloys, clearly showing that there is a proportional relationship between the yield isotropy and the CRSS ratio, indicating that large yield isotropy is necessary to obtain a large CRSS ratio. Figure 4.14 shows the correlation between the Erichsen value and the yield isotropy of the Mg-4Zn-X-Ca alloys, demonstrating an increase in the yield isotropy of Mg-4Zn-X-Ca alloys with the Erichsen value. This suggests that higher formability of Mg alloys can result from the enhanced yield isotropy stemming from the modification of the contribution of the deformation behavior. Mg-4Zn-X-Ca alloys demonstrate the potential of TRC Mg alloys with high formability (an Erichsen value of 70 ~8.0mm) and high strength levels (Y.S. of 167 ~ 189MPa). These values are comparable to those of Al alloys.

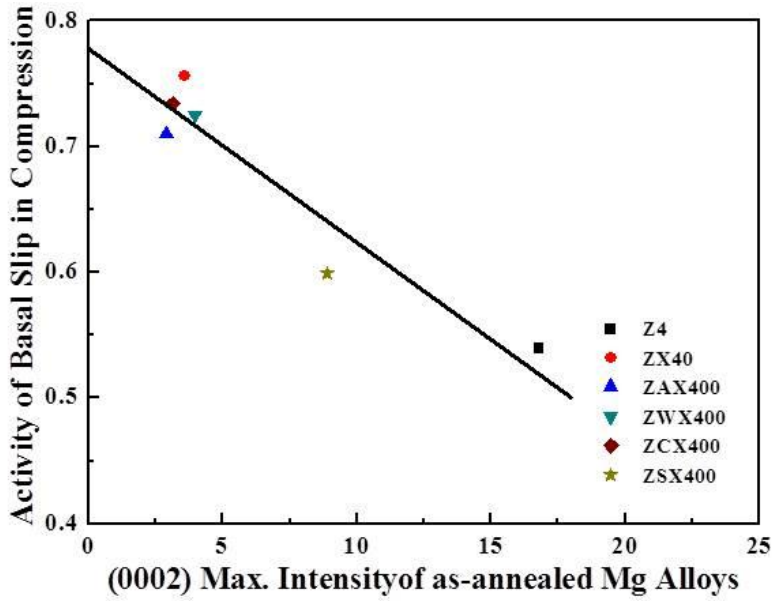


Figure 4.11 Relationship between activity of basal slip in compression at initial stage and (0002) max. intensity of basal texture.

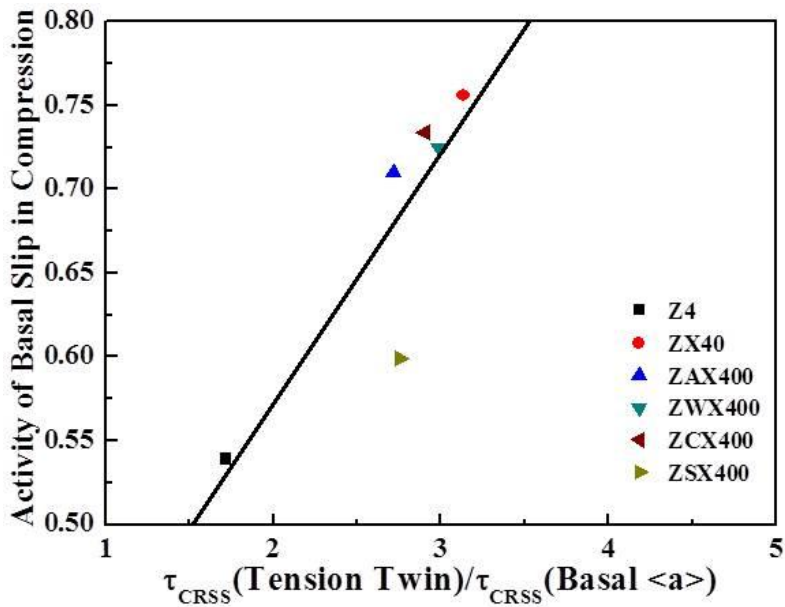


Figure 4.12 Activity of basal slip in compression at initial stage and CRSS ratio (tension twin/basal <a>slip).

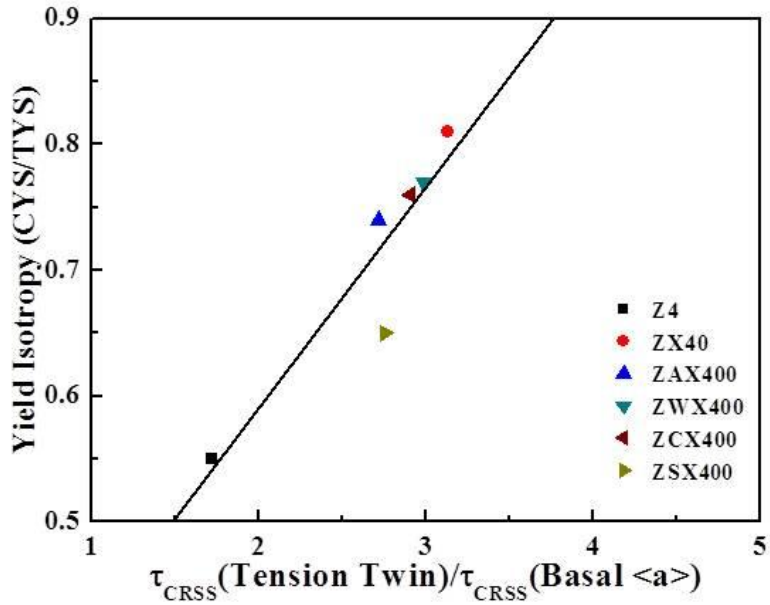


Figure 4.13 Variation of yield isotropy and CRSS ratio (tension twin/basal $\langle a \rangle$ slip).

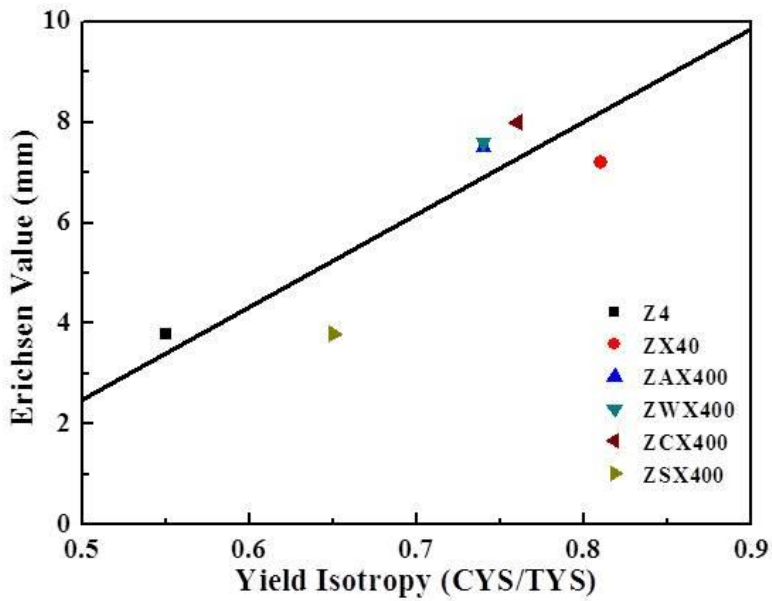


Figure 4.14 Relationship between Erichsen values and yield isotropy.

4.3.6 Finite element simulation during Erichsen test

To understand the deformation behavior during Erichsen test, finite element method has been conducted. In order to carry out the Erichsen simulation, 1,000 grains, 1,199 meshes in sheet and 0.12 shear friction coefficient between sheet and punch are used. Fig. 4.15 indicates the strain distribution of annealed Z4 and ZX40 alloy. It indicates that maximum effective strain of Z4 alloys have higher value of effective strain compared to that of ZX40 alloy during Erichsen test. Max. effective strain of ZX40 alloy is only 0.32mm/mm at 8mm of Erichsen value, however, that of Z4 alloy is 0.48 which are not formable at room temperature due to strong basal texture. Fig. 4.16 indicates the relative activity of Z4 and ZX40 alloys during Erichsen test. Basal $\langle a \rangle$ slip, $\langle c+a \rangle$ slip and tension twin are the main deformation modes. However, basal $\langle a \rangle$ slip generally accommodates the most strain during Erichsen test. In case of “A” position, more relative activity of basal $\langle a \rangle$ slip occurs at ZX40 alloy compared with Z4 alloy because of random texture which easily activates the basal $\langle a \rangle$ slip. With the increase of strain, the relative activity of basal $\langle a \rangle$ slip decreases, and that of $\langle c+a \rangle$ slip gradually increases. Similar result is observed at “B” position. As the process goes on, the relative activity of basal $\langle a \rangle$ slip decreases, however, that of $\langle c+a \rangle$ slip increases. Fig. 4.17 indicates the relationship between Erichsen values and CRSS ratio (tension twin/basal $\langle a \rangle$ slip) at 15% which are corresponded to 3.5mm of Erichsen value at center of Z4 and ZX40 alloys. There is a proportional relationship between the formability and the CRSS ratio (tension twin/basal $\langle a \rangle$ slip), indicating that accelerating the basal $\langle a \rangle$ slip is helpful to accommodate the strain along the thickness direction. Therefore, highly formable Mg alloys could be developed by modifying deformation modes.

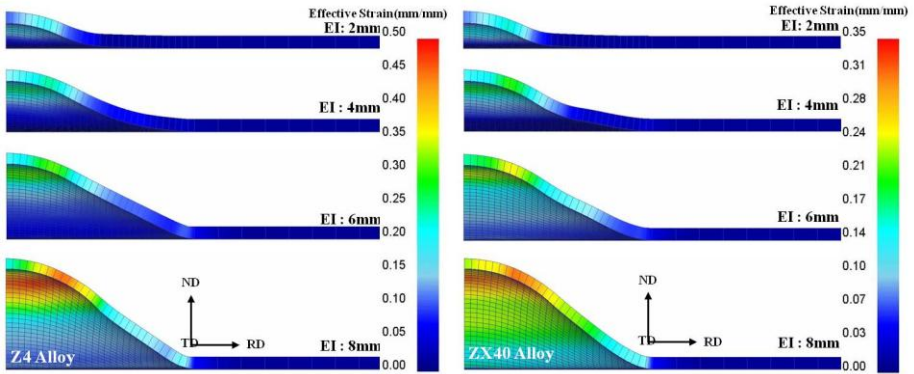


Figure 4.15 The strain distribution along the RD according to Erichsen test of Z4 and ZX40 alloys.

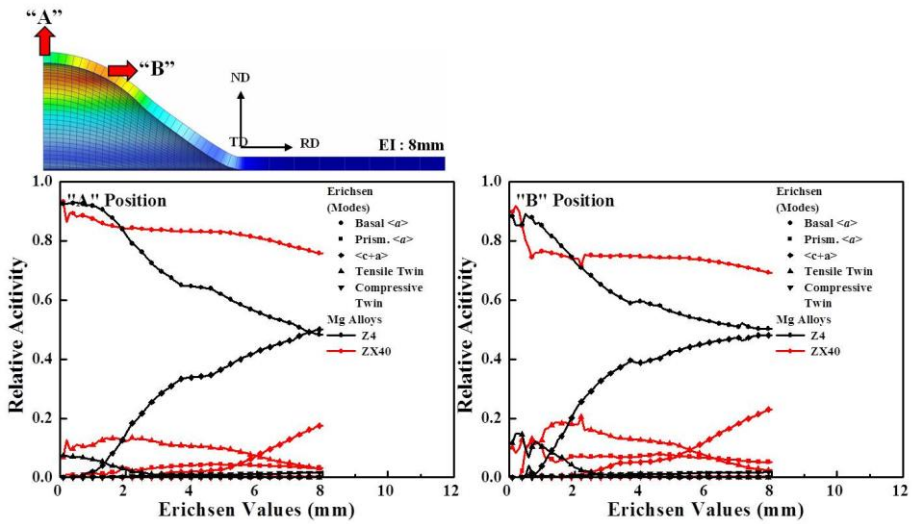


Figure 4.16 Contribution of the deformation modes during Erichsen test of Z4 and ZX40 alloys.

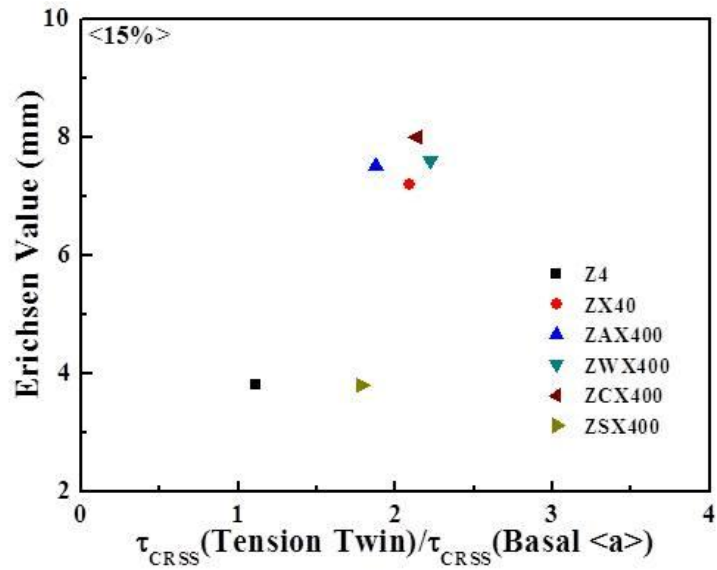


Figure 4.17 Relationship between Erichsen values and CRSS ratio (tension twin/basal $\langle a \rangle$ slip) at 15% corresponding to 3.5mm of Erichsen value at center position.

4.4 Conclusions

Formability and VPSC simulations of Mg-4Zn-X-Ca alloys were done in an effort to understand the effects of different deformation behaviors on the room-temperature formability of Mg-4Zn-X-Ca alloys. Furthermore, the mechanical properties and the microstructural and texture evolution properties of Mg-4Zn-X-Ca alloys were also investigated. The main conclusions are given below.

(1). Mg-4Zn-X-Ca alloys showed sound microstructures in the as-cast condition with no occurrence of inverse segregation on their surfaces. In addition, significant grain refinement was observed in the ZAX400 alloy due to the formation of intermetallic compounds related to the Al and Ca elements.

(2). Mg-4Zn-X-Ca alloys exhibited random textures whose basal poles were tilted toward the transverse direction, except for the ZSX400 alloy, which showed a strong basal texture with a texture similar to that of the Z4 alloy due to the different static recrystallization behaviors.

(3). Mg-4Zn-X-Ca alloys showed high formability with Erichsen values of 7~8mm and high yield strength levels of 167 ~ 189MPa due to the non-basal textures and the effect of the strengthening of the grain refinement. Specifically, the ZAX400 alloy showed a high yield strength value of 189.3MPa with an Erichsen value of 7.5mm, comparable to those of Al alloys.

(4). Compared to the Z4 alloy, the ZX40 alloy had higher relative basal $\langle a \rangle$ slip activity in both tension and compression modes in all deformation stages. This was caused by the change of the CRSS ratio (tension twin/basal $\langle a \rangle$ slip). An increase in the CRSS ratio induces limited

activity of tension twin deformation to accommodate the strain.

(5). There was a close correlation between the formability of Mg-4Zn-X-Ca alloys and the activity of the deformation modes, between the Erichsen value and the yield isotropy, and between the yield isotropy and the CRSS ratio (tension twin/basal $\langle a \rangle$ slip). Higher formability of Mg alloys can be obtained from the improved the yield isotropy.

Bibliography

1. D. Liang, C. B. Cowley, "The twin-roll strip casting of magnesium", *JOM*, 56, (2004) pp. 26-28.
2. S. S. Park, W. J. Park, C. H. Kim, B. S. You, Nack J. Kim, "The twin-roll casting of magnesium alloys" *JOM*, 61, (2009) pp. 14-18
3. X. Huang, K. Suzuki, A. Watazu, I. Shigematsu, N. Saito, "Improvement of formability of Mg-Al-Zn alloy sheet at low temperatures using differential speed rolling", *J. Alloys Compd*, 470 (2009) pp. 263-268.
4. T. Mukai, M. Yamanoi, H. Watanabe, K. Higashi, "Ductility enhancement in AZ31 magnesium alloy by controlling its grain structure", *Scripta Mater.* 45 (2001) pp. 89-94.
5. Y. Chino, J. S. Lee, K. Sassa, A. Kamiya, M. Mabuchi, "Press formability of a rolled AZ31 Mg alloy sheet with controlled texture", *Mater. Letters* 60 (2006) pp. 173-176.
6. M. Yuasa, N. Miyazawa, M. Hayashi, M. Mabuchi, Y. Chino, "Effects of group II elements on the cold stretch formability of Mg-Zn alloys", *Acta Mater.* 83 (2015) pp. 294-303.
7. Y. Chino, K. Sassa, M. Mabuchi, "Texture and stretch formability of a rolled Mg-Zn alloy containing dilute content of Y", *MSE A* 513-514 (2009) pp. 394-400.
8. L. Gao, H. Yan, J. Luo, A. A. Luo, R. "Microstructure and mechanical properties of a high ductility Mg-Zn-Mn-Ce magnesium alloy", *Chen, J. Magnesium Alloys 1* (2013) pp. 283-291.
9. D. H. Kang, D. W. Kim, S. Kim, G. T. Bae, K. H. Kim, N. J. Kim, "Relationship between stretch formability and work-hardening capacity of twin-roll cast Mg alloys at room temperature", *Scripta Mater.* 61 (2009) pp. 768-771.

- 10.X. Huang, K. Suzuki, Y. Chino, M. Mabuchi, "Influence of aluminium content on the texture and sheet formability of AM series magnesium alloys", *MSE A* 663 (2015) pp. 144-153.
- 11.Y. Chino, K. Sassa, A. Kamiya, M. Mabuchi, "Enhanced formability at elevated temperature of a cross-rolled magnesium alloy sheet", *MSE A* 441 (2006) pp. 349-356.
- 12.D. Y. Ju, X. D. Hu, "Effect of casting parameters and deformation on microstructure evolution of twin-roll casting magnesium alloy AZ31", *Trans. Nonferrous Met. Soc. China* 16 (2006) pp. s874-s877.
- 13.J. Zeng, R. Koitzsch, H. Pfeifer, B. Friedrich, "Numerical simulation of the twin-roll casting process of magnesium alloy strip", *J. Mater. Process. Technol.* 209 (2009) pp. 2321-2328.
- 14.Y. Chino, T. Ueda, Y. Otomatsu, K. Sassa, X. Huang, K. Suzuki, M. Mabuchi, "Effects of Ca on tensile properties and stretch formability at room temperature in Mg-Zn and Mg-Al alloys", *Mater. Trans.* 52 (2011) pp. 1477-1482.
- 15.Y. N. Wang, J. C. Huang, "Texture analysis in hexagonal materials", *Mater. Chem. Phys.* 81 (2003) pp. 11-26.
- 16.S. R. Agnew, M. H. Yoo, C. N. Tome, "Application of texture to understanding mechanical behavior of Mg and solid solution alloys containing Li or Y", *Acta Mater.* 49 (2001) pp. 4277-4289.
- 17.B. C. Wonsiewicz, W. A. Backofen, "Plasticity of magnesium crystals", *Trans. AIME* 239 (1967) pp. 1422-1431.
- 18.J. Y. Lee, Y. S. Yun, B. C. Suh, N. J. Kim, W. T. Kim, D. H. Kim, "Comparison of static recrystallization behavior in hot rolled Mg-3Al-1Zn and Mg-3Zn-0.5Ca sheets", *J. Alloys Compd.* 589 (2014) pp. 240-246.

- 19.H. Wang, B. Raeisinia, P. D. Wu, S. R. Agnew, C. N. Tome, "Evaluation of self-consistent polycrystal plasticity models for magnesium alloy AZ31B sheet", *Inter. J. Solids Structures*, 47, (2010) pp. 2905-2917.
- 20.Y. Chino, M. Kado, M. Mabuchi, "Enhancement of tensile ductility and stretch formability of magnesium by addition of 0.2wt% Ce", *MSE A* 494 (2008) pp. 343-349.
- 21.K. Suzuki, Y. Chino, X. Huang, M. Yuasa, M. Mabuchi, "Enhancement of room temperature stretch formability of Mg-1.5mass%Mn alloy by texture control", *Mater. Trans.* 54 (2013) pp. 392-398.
- 22.Z. X. Cai, H. T. Jiang, D. Tang, Z. Ma, Q. Kang, "Texture and stretch formability of rolled Mg-Zn-RE alloys at room temperature", *Rare Met.* 32 (2013) pp. 441-447.
- 23.Y. Chino, X. Huang, K. Suzuki, K. Sassa, M. Mabuchi, "Influence of Zn concentration on stretch formability at room temperature of Mg-Zn-Ce alloy", *MSE A* 528 (2010) pp. 566-572.
- 24.Y Chino, M. Mabuchi, "Enhanced stretch formability of Mg-Al-Zn alloy sheets rolled at high temperature", *Scripta Mater.* 60 (2009) pp. 447-450.
- 25.X. Huang, K. Suzuki, Y. Chino, M. Mabuchi, "Texture and stretch formability of AZ61 and AM60 magnesium alloy sheets processed by high-temperature rolling", *J. Alloy Comp.* 632 (2015) pp. 94-102.
- 26.X. Huang, K. Suzuki, N. Saito, "Textures and stretch formability of Mg-6Al-1Zn magnesium alloy sheets rolled at high temperatures up to 793K", *Scripta Mater.* 60 (2009) pp. 651-654.
- 27.X. Huang, K. Suzuki, N. Saito, "Microstructure and mechanical properties of AZ80 magnesium alloy sheet processed by differential speed rolling", *MSE A* 508 (2009) pp. 226-233.

28. D. Wu, R. S. Chen, E. H. Han, "Excellent room-temperature ductility and formability of rolled Mg-Gd-Zn alloy sheets", *J. Alloys Comp.* 509 (2011) pp. 2856-2863.
29. X. Huang, K. Suzuki, Y. Chino, "Static recrystallization and mechanical properties of Mg-4Y-3RE magnesium alloy sheet processed by differential speed rolling at 823K", *MSE A* 538 (2012) pp. 281-287.
30. H. Takuda, S. Kikuchi, N. Yoshida, H. Okahara, "Tensile properties and press formability of a Mg-9Li-1Y alloy sheet", *Mater. Trans.* 44 (2003) pp. 2266-2270.
31. Q. Yang, B. Jiang, J. Li, H. Dong, W. Liu, S. Luo, F. Pan, "Modified texture and room temperature formability of magnesium alloy sheet by Li addition", *Int. J. Mater. Form* (2015) pp.1-7.
32. M. R. Barnett, C. H. J. Davies, X. Ma, "An analytical constitutive law for twinning dominated flow in magnesium", *Scripta Mater.* 52 (2005) pp. 627-632.
33. S. M. Yin, C. H. Wang, Y. D. Diao, S. D. Wu, S. X. Li, "Influence of grain size and texture on the yield asymmetry of Mg-3Al-1Zn alloy", *J. Mater. Sci. Technol.* 27 (2011) pp.29-34.

초 록

자동차 차체 경량화 및 연료 효율 증진에 대한 관심이 증가하면서 자동차부품의 경량화 소재로써 마그네슘합금의 적용에 대한 요구가 폭발적으로 증가하고 있다. 현재 마그네슘 부품은 제조단가가 저렴한 다이캐스팅 및 중력주조와 같은 주조 공정을 활용하여 제조되고 있으나, 주조 결함으로 인한 강도 및 연신율 등 낮은 기계적 특성으로 인해 그 적용이 제한되고 있으며, 고인성을 갖는 마그네슘부품에 대한 수요는 지난 수십 년 동안 급격히 증가되고 있다. 기계적 특성이 우수한 가공재 마그네슘 부품은 대부분 압출 또는 압연 공정으로 통해 제조되고 있으나 가공 공정은 주조 공정에 비해 많은 비용이 소비되어 가격 경쟁력이 떨어진다. 따라서 가공재 마그네슘 부품을 저렴하게 제조할 수 있는 신제조 공정 개발이 필요한 상황이다. 최근 압연과 주조 공정을 동시에 부여할 수 있는 트윈 롤 캐스팅 공정에 대한 관심이 높아지고 있으며, 상용합금인 Mg-Al-Zn 합금 판재를 저렴한 생산비용으로 제조할 수 있는 트윈 롤 캐스팅 공정이 구축되었다. 하지만 Mg-Al-Zn 합금은 트윈 롤 캐스팅 시 중심편석과 크랙이 발생하여 최종 판재의 기계적 특성 및 표면 특성에 악영향을 미치며, 반복적인 압연공정으로 인해 강한 저면 집합조직이 형성되어 낮은 성형성을 나타낸다. 따라서 마그네슘 가공재에 대한 적용 확대를 위해서는 트윈 롤 캐스팅 공정에 적합한 마그네슘합금 개발이 필요하며, 이와 동시에 반복적인 압연공정에서도 비저면

집합조직을 형성할 수 있는 마그네슘 합금개발이 요구된다.

첫 번째 연구 목표는 트윈 롤 캐스팅 공정에 적합한 마그네슘합금을 개발하기 위해 Mg-6Al 합금의 응고 거동과 변형 거동에 대해 분석하였다. 트윈 롤 캐스팅 공정에 대한 전산모사 결과를 보면, AX60 합금은 편석 형성 경향이 낮은 반면에 AZ60 합금은 편석 형성 경향이 높으며, 이는 각 합금이 갖는 응고 거동과 열적 특성이 편석 형성에 밀접한 관계가 있는 것을 확인 할 수 있었다. 실제 주조재의 미세조직에서 볼 수 있듯이, TRC 전산모사 결과와 중심편석의 분율 사이에 밀접한 상관관계가 있는 것을 확인하였다. 또한 Ca와 Sr를 첨가한 Mg-6Al-X 합금은 Mg-6Al 합금과 비교했을 때, 비저면 집합조직이 좀 더 발달하였다. 압연 온도를 350도에서 450도로 증가할 경우 비저면 집합조직을 갖는 마그네슘 합금 판재를 제조할 수 있었다. 소성변형거동 전산모사 결과에서는 압연 온도가 증가할수록 압축 시 인장쌍정에 대한 활동도가 억제되었으며, 이로 인해 Mg-6Al 합금의 항복강도 등방성과 성형성이 개선되었다.

두 번째 연구 목표는 고성형성을 구현할 수 있는 마그네슘합금을 개발하기 위해 Al, Mn, Ca, Sn, Sr, Zn 등 합금원소 첨가에 따른 Mg-xAl 합금과 Mg-6Al-X 합금의 항복강도 등방성, 변형 거동, 기계적 특성 및 집합조직 변화를 체계적으로 조사하였다. 일반적으로 합금원소 함량이 증가함에 따라 항복강도의 등방성이 개선되었으며, Ca 합금원소는 다른 합금원소보다 항복강도의 등방성 개선에 큰 효과가 있었다. 특히 Ca이 1wt.% 첨가된 AX61 합금의 항복강도 등방성이 0.80으로 A6합금에 비해 크게 개선되었다.

소성변형거동 전산모사 결과에서는 약한 저면 집합조직이 형성될수록 압축 변형 시 인장쌍정에 대한 활동도는 감소되었으며, 이는 인장쌍정과 저면슬립에 대한 CRSS비가 인장쌍정의 발생에 큰 영향을 주는 것으로 조사되었다.

세 번째 연구 목표는 고강도 고성형성 TRC 마그네슘 합금개발에 대해 조사하였다. 고강도 및 고성형성을 구현하기 위해 성형성과 소성변형거동 전산모사결과간의 상관 관계를 분석하여 성형성이 크게 영향을 미치는 변형거동에 대해 조사하였다. 또한 Mg-4Zn-X-Ca 합금에 대한 미세조직, 집합조직 및 기계적 특성을 체계적으로 분석하였다. 모든 주조재 합금계에서 양호한 미세조직을 갖는 것을 확인할 수 있었으며, 판재 표면에 악영향을 미치는 역편석은 모든 합금계에서 발생하지 않은 것을 볼 수 있다. 어닐링된 Z4와 ZSX400 합금계는 강한 저면 집합조직이 형성되었으나 나머지 다른 합금에서는 TD 방향으로 기울어진 랜덤 집합조직이 형성되었다. ZX40 합금은 Z4합금과 비교했을 때, 항복강도와 성형성이 크게 향상되었으며, ZX40 합금의 성형성은 7.2mm으로 나타내었다. 특히 ZAX400 합금은 항복강도 189.3MPa, 에릭슨값 7.5mm으로 알루미늄 판재와 동등한 기계적 특성 및 성형성을 나타내었다. Mg-4Zn-X-Ca 합금의 고성형성 특징은 집합조직 변화와 밀접한 관계가 있으며, 특히 변형 거동에 크게 영향을 받는 것을 조사되었다. 고성형성을 나타낸 ZX40, ZAX400, ZCX400, ZWX400 합금은 상대적으로 압축 시 저면 슬립의 활동도가 증가하는 반면, Z4, ZSX400 합금은 저면 슬립의 활동도가 상대적으로 낮으며, 이는 저면 슬립과 인장쌍정에 대한 CRSS 비에

의해 결정되는 것을 확인하였다.

주요어: 마그네슘합금, 트윈 롤 캐스팅, 편석, 기계적 특성, 성형성,
집합조직, 소성변형거동

학 번: 2010-30176